NASA CR. 183,028

A Reproduced Copy

Λ   ~~OF~~

NASA CR-183,028

Reproduced for NASA

by the

NASA Scientific and Technical Information Facility

FFNo 672 Aug 65

3 1176 01329 1365

FINAL REPORT

"Fiber Waveguide Sensors for Intelligent Materials"

NASA Grant NAG-1-780

June 1988

Prepared by: A. R. Flax
              R. O. Claus

TABLE OF CONTENTS

SUMMARY

This report, an addendum to the six month report submitted to NASA Langley Resesearch Center in Dececember 1987, will cover the research performed by the Fiber and Electro-Optics Research Center (FEORC) at Virginia Tech for the NASA Langley Research Center Grant NAG-1-780, for the period from December 1987 - June 1988. This final report will discuss the research performed in the following four areas that are mentioned in the proposal: Fabrication of Sensor Fibers Optimized for Embedding in Advanced Composites, Fabrication of Sensor Fiber with In-Line Splices and Evaluation via OTDR Methods, Modal Domain Optical Fiber Sensor Analysis, and Acoustic Fiber Waveguide Implementation.

DISCUSSION

This section will discuss the four research areas mentioned in the NASA Langley Grant, NAG-1-780. The four research areas which will be discusssed are the following: Fabrication of Sensor Fibers Optimized for Embedding in Advanced Composite Materials, Fabrication of Sensor Fiber with In-Line Splices and Evaluation via OTDR Methods, Modal Domain Optical Fiber Sensor Analysis, and Acoustic Fiber Implementation.

1. Fabrication of Sensor Fibers Optimized for Embedding in Advanced Composite Materials

Optical fibers embedded in materials, i.e. composites, can sense position, strain, temperature, structural vibrations, and impact [2]. Several embedded optical fiber sensors have been investigated in the past six months. A Mach-Zehnder interferometer was used to sense tensile and composite strains in a composite material laminate [1]. Acoustic emission in symmetric cross-ply composite laminates due to axial loading was interrogated with embedded optical fibers. This data was successfully compared to a piezoelectric transducer adhered to the composite where the transducer monitored acoustic emissions due to axial loading [3]. Fibers attached to an aluminum plate were used to assess impact damage. The various signals could be correlated to an impact height. Also, methods were used to

2

determine impact location [4]. The integrity of the composite
due to embedded optical fibers has been examined by Moire
interferometry techniques [5,11]. There has been a movement
toward creating an 'intelligent structure.' An intelligent material
consists of embedded actuators and sensors. Fiber optic sensors
used to create intelligent aerospace structures have been examined
[16]. Several papers review what smart structures are [6,7,13,
17]. Problems associated with smart structures have been
identified [8].

In the past six months there has been no progress in
developing specialty fibers for improving specimen integretiy
because the draw tower is not fully operational.

2. Fabrication of Sensor Fiber with In-Line Splices and Evaluation via OTDR Methods

Detecting localized strain with in-line air-gap splices in
an optical fiber in conjunction with an Optical Time Domain
Reflectometer (OTDR) was reviewed at the Smart Structures
Workshop [9]. This experiment using the high resolution OTDR,
has been delayed due to a defective OTDR. Due to this delay,
another graduate student working on this project, Sanjay Sudeora,
will send a report to NASA as soon this difficulty is overcome.

3. Modal Domain Sensor Analysis

In the past six months the research in modal domain sensing
has been directed towards analytically describing the movement
of few-moded speckle patterns as perturbations are applied to an
optical fiber [10,15,18], pursuing micro-optical fiber devices

which can be used with modal domain sensing systems [19] and real time signal processing of modal domain signals [14].

FEORC has analytically described the movement of two few-moded speckle patterns as perturbations are applied to the optical fiber: a three-lobed rotational speckle pattern and a two-lobed speckle pattern where the two lobes exchange power as the optical fiber is perturbed. The system sensitivity for both of these modal patterns has been described. FEORC has concluded that the two-lobed pattern is the optimum modal pattern [10,15,18].

In conjunction with modal domain sensing two in-line micro-optical devices can make a modal domain sensing system compact and packageable. An in-line laterally offset few-moded optical fiber splice can monitor one lobe of the two-lobed speckle pattern, thus performing in-line signal processing. The splice loss of two laterally offset few-moded optical fibers has been derived, because existing single mode and multimode optical fiber splice loss formulas can not be applied to few-moded optical fiber splices. The other device is a modal conversion coupler, which converts the input modes of the modal conversion coupler, a fused biconical taper coupler, to another set of modes. The amplitude coefficients associated with the modes propagating in a modal domain sensor are unknown. The modal conversion coupler may be a method of creating a mode with a known modal amplitude and superimposing several modes to create a totally characterizable modal domain sensor [19].

4

A detector array can be used to process modal domain output patterns. This array is linked to an IBM-PC to analyze the data in real time [14].

Finally, the modal domain demonstration unit was delivered to NASA Langley in April 1988. This unit uses modal domain sensing techniques to detect quiscent strain, AC strain, structural vibrations, and acoustic emission in a graphite-epoxy composite.

4. Acoustic Fiber Waveguide Implementation

Acoustic waveguide sensors were reveiwed at the Smart Structures Workshop [11]. In the second six months of this contract, there has been no significant progress in the area of acoustic waveguides. FEORC is waiting for the arrival of some ultrasonics equipment and the draw tower to become fully operational.

REFERENCES

JOURNAL PAPERS

[1] "A Rugged Optical Fiber Interferometer for Strain Measurements Inside a Composite Material Laminate," ASTM,Journal of Composites Technology & Research, Spring 1988, Vol. 10, No. 10 pp 11-15 (K. Murphy and J.C. Duke, Jr.).

SMART STRUCTURES WORKSHOP PAPERS (Blacksburg, VA) - April 1988

[2] "Fiber Optic Methods for Structure Monitoring," (K.D. Bennett and R.O. Claus).

[3] "Acoustic Emission Detection in Smart Materials," (K.D. Bennett and K.D. Zehner).

[4] "Fiber Optic Assessment of Impact Damage in Smart Materials," (M.R. Dumais and K.D. Bennett).

[5] "Experimental Analysis of Smart Structure Materials by Full-Field Optical Techniques," (R. Czarnek).

[6] "Introduction Issues for Smart Structures," (R.O. Claus).

[7] "Material Issues for Smart Structures," (G.L. Wilkes).

[8] "Control and Signal Processing Design Issues in Smart Structures," (J.C. McKeeman and D.K. Lindner).

[9] "Applications of OTDR Methods for Structural Analysis," (R.G. May, Jr.).

[10] "Modal Interference Techniques for Strain Detection in Few-Mode Optical Fibers," (B.D. Duncan).

[11] "Acoustic Fiber Methods for Structural Monitoring," (A. Safaai-Jazi).

SPIE CONFERENCE (Boston, MA) - SEPTEMBER 1988

[12] "Interferometric Meeasurements of Strain Concentrations Induced By An Optical Fiber Embedded in Fiber Reinforced Composites," (R. Czarnek, Y.F. Guo, K.D. Bennett and R.O. Claus).

[13] "Demonstration of A Smart Structure With Embeedded
      Actuators and Sensors," (C.A. Rogers, K.D. Bennett,
      H.H. Robertshaw and J.C. McKeeman).

[14] "Full Field Analysis of Modal Domain Sensor Signals for
      Structural Control," (K.D. Bennett, J.C. McKeeman and
      R.G. May).

[15] "Intensity Pattern Modulation in Optical Fiber Modal
      Domain Sensor Systems: Experimental Results,"
      (B.D. Duncan and B.W. Brennan).

[16] "Smart Structures Program at Virginia Tech," (R.O.
      Claus and K.D. Bennett).

[17] "Fiber Optic Sensor Systems for Smart Aerospace
      Structures," (W.J. Rowe, R.O. Claus, D.A. Martin and
      D. Trites).

M.S. THESES

[18] "Mode Interference Techniques for Strain Detection in
      Few-Mode Optical Fibers," M.S. Thesis, Electrical
      Engineering Department, Virginia Tech, April 1988
      (B.D. Duncan).

[19] "Micro-Optical Fiber Devices Used With Modal Domain
      Sensing," M.S. Thesis, Electrical Engineering
      Department, Virginia Tech, To Be Defended - June 1988
      (A.R. Flax).

APPENDIX A - Thesis Abstracts

Modal Interference Techniques for Strain Detection in Few-Mode Optical Fibers

by

Bradley Dean Duncan

Richard O. Claus, Chairman

Electrical Engineering

(ABSTRACT)

Interference between the modes of an optical fiber results in specific intensity patterns which can be modulated as a function of disturbances in the optical fiber system. These modulation effects are a direct result of the difference in propagation constants of the constituent modes. In this presentation it is shown how the modulated intensity patterns created by the interference of specific mode groups in few-mode optical fibers (V < 5.0) can be used to detect strain. A detailed discussion of the modal phenomena responsible for the observed strain induced pattern modulation is given and it is shown that strain detection sensitivities on the order of 10^{-9} can be expected. Data taken during the evaluation of an actual experimental strain detection system based on the developed theory is also presented.

Micro-Optical Fiber Devices Used With Modal Domain Sensing

by

Amy Flax

R. O. Claus, Chairman

Electrical Engineering

(ABSTRACT)

In order to develop more compact optical fiber sensing systems, modal filtering can be performed in-line by using micro-optical devices. Two such devices are a laterally offset few-moded optical fiber mechanical splice and a modal conversion optical fiber coupler. A third device, the air-gap splice used with multimode fibers, can examine the modal content of an optical fiber. A basic theoretical understanding on how these devices operate is reviewed. A splice loss calculation for few-moded optical fibers is presented. Applications of the asymmetrical few-moded mechanical optical fiber splice, the modal conversion coupler, and the air-gap splice are discussed.

APPENDIX B - Embedded Optical Fiber Sensor Engineering

APPENDIX C - Modal Domain Sensing
Related M.S. Thesis I

APPENDIX D - Modal Domain Sensing
    Related M.S. Thesis II

Micro-Optical Fiber Devices Used With Modal Domain Sensing

by

Amy Flax

Thesis submitted to the Faculty of the

Virginia Polytechnic Institute and State University

in partial fulfillment of the requirements for the degree of

Master of Science

in

Electrical Engineering

APPROVED.

_____
R. O. Claus, Chairman

_____   _____
A Safaai-Jazi   J. C. McKeeman

June 1988

Blacksburg, Virginia

Micro-Optical Fiber Devices Used With Modal Domain Sensing

by

Amy Flax

R O. Claus, Chairman

Electrical Engineering

(ABSTRACT)

In order to develop more compact optical fiber sensing systems, modal filtering can be performed in-line by using micro-optical devices. Two such devices are a laterally offset few-moded optical fiber mechanical splice and a modal conversion optical fiber coupler. A third device, the air-gap splice used with multimode fibers, can examine the modal content of an optical fiber A basic theoretical understanding on how these devices operate is reviewed. A splice loss calculation for few-moded optical fibers is presented. Applications of the asymmetrical few-moded mechanical optical fiber splice, the modal conversion coupler, and the air-gap splice are discussed.

Acknowledgements

I would like to express my appreciation to my advisor, Dr. R.O. Claus, for his guidance and encouragement. I would like to thank Dr. Safaai-Jazi for his patience and assistance.

I would, also, like to thank all the FEORC employees and graduate students for their consultation and companionship

I would like to thank my two dear friends, Amy Matthews and Paul Werntz, for their support, encouragement, and understanding. Finally, I would like to especially thank Paul for helping me focus

Table of Contents

List of Illustrations

1.0 Introduction

Fiber optic sensing systems may be used to detect temperature, pressure, acoustic waves, strain, and a wide range of physical observables The classical method for detecting these parameters with maximum sensitivity uses single mode fiber optic interferometers, which require two optical fibers. The reference fiber in such an interferometer must be maintained in a controlled environment for optimum detection. To eliminate this .
of two optical fibers in a sensing system, the modal changes in one multimode optical fiber due to perturbations of the optical fiber can be exploited. This type of fiber optic sensing is called modal domain sensing.

Modal domain sensing is most effective when used with a few-moded optical fibers. So far the few-moded optical fibers used with modal domain sensing support 2 to 10 modes [1,2] The optimum far field interference pattern of the fiber modes, the speckle pattern, is a modal field interference pattern that can be characterized by simple rotations or simple intensity changes in the far field intensity pattern due to modal changes from perturbations to the optical fiber [2] But the question now is what to do with the optical information at the output of the sensor fiber (how to glean the relevant information

from the modal domain sensor). In-line micro-optical fiber devices would eliminate cumbersome non-optical spatial filters, realignment problems, and additional electrical circuitry which make far field pattern processing difficult. Micro-optical fiber devices create and enable compact, packageble modal domain sensing systems.

Two such micro-optical fiber devices used with modal domain sensing systems are an optical fiber asymmetrical splice and an optical fiber modal conversion coupler. The optical fiber asymmetrical splice consists of a few-moded optical fiber spliced to a laterally offset few-moded optical fiber or to a single mode optical fiber for in-line spatial filtering. The optical fiber modal converter is an optical fiber coupler which generates a set of output modes from a given set of input modes.

Another important micro-optical fiber device is the air-gap splice used with multimode optical fibers to detect local strain changes via Fresnel backscattered-based Optical Time Domain Reflectometry (OTDR) [3]. The air-gap splice causes pulse delay effects depending on the modes which are propagating in the multimode optical fiber.

The principles of operation of the two devices used with modal domain sensing, the asymmetrical optical fiber splice and the optical fiber modal converter coupler and the principle of operation of the air-gap splice will be explained in Chapter 4 of this thesis. Finally, future applications of these micro-optical devices will be discussed in Chapte 5.

2.0 Optical Fiber Theory

The basic parameters that determine the nature of the electromagnetic fields which may propagate in optical fibers, and the basic mode theory which describes those fields need to be reviewed in order to understand the operation of the micro-optical fiber devices intended for sensor signal processing

2.1 Basic Parameters Governing Optical Fibers

An optical fiber typically is a cylindrical waveguide fabricated from a dielectric, silica, as shown in Figure 1 [4]. The center of the optical fiber, the core, has an index of refraction of n_1. The core has a radius, a Surrounding the core is the cladding which has an index of refraction, n_2, which is slightly smaller than n_1.

The optical fiber waveguide will only support a discrete number of modes, having a unique propagation constant, β. The propagation constants of the modes supported by

$NA = SIN\theta$

θ

LIGHT RAYS

ACCEPTANCE
CONE
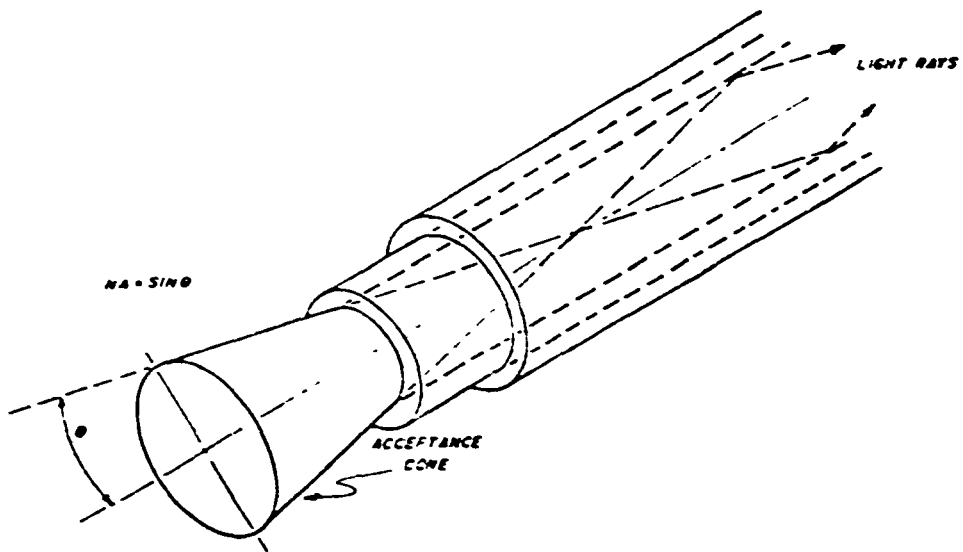
Figure 1.   An Optical Fiber [4]

2.0 Optical Fiber Theory

the optical fiber must fall between the wave number of the core and the wave number of the cladding, Equation 2.1-1.

$$n_2 k_0 \leq \beta \leq n_1 k_0 \qquad (2.1-1)$$

where

$$k_0 = \omega\sqrt{\mu_0 \varepsilon_0}, \; \textit{free space wavenumber,}$$

$$n_2 k_0 = n_2 \omega\sqrt{\mu_0 \varepsilon_0}, \; \textit{wavenumber in the cladding, and}$$

$$n_1 k_0 = n_1 \omega\sqrt{\mu_0 \varepsilon_0}, \; \textit{wavenumber in the core}$$

The amount of light that can be accepted by the optical fiber is determined by the numerical aperture (*NA*). The numerical aperture defines the acceptance cone for the light that will propagate in the core. The numerical aperture is defined in terms of the indices of refraction of the core and cladding as

$$NA = (n_1{}^2 - n_2{}^2)^{1/2} = \sin\theta, \qquad (2.1-2)$$

where θ is the cone of acceptance angle as shown in Figure 1.

The *V — number* of an optical fiber determines how many propagating modes the optical fiber will support. The *V — number* is defined in terms of the numerical aperture (*NA*), the optical fiber's core radius (*a*) and input source's wavelength of operation (λ) as indicated in (2.1-3).

$$V = \frac{2\pi a}{\lambda} (n_1{}^2 - n_2{}^2)^{1/2} \qquad (2.1-3)$$

By knowing the $V - number$ for a few-moded optical fiber, the number of propagating modes can be determined analytically. The results of the analysis are shown graphically in Figure 2 [5]. Now, the propagation constant for each mode can be determined from the normalized propagation constant, b, where

$$b = \frac{(\beta/k_o)^2 - n_2^2}{n_1^2 - n_2^2}, \text{ and} \qquad (2.1-4)$$

$$\beta = k_o[\, b(n_1^2 - n_2^2) + n_2^2\,]^{1/2}. \qquad (2.1-5)$$

2.2 Optical Fiber Mode Theory

After reviewing the parameters that govern the operation of an optical fiber, a rev of basic mode theory is essential in understanding the principles of operation oi micro-optical fiber devices. The electromagnetic field solutions in optical fibers are solutions to the wave equation for cylindrical waveguides, i.e.

$$\nabla^2\left(\frac{\vec{E}}{\vec{H}}\right) + (k_o^2 n^2)\left(\frac{\vec{E}}{\vec{H}}\right) = 0 \qquad (2.2-1)$$

In Equation 2 2-1, k, is the free space wavenumber and n is the index of refraction ($\cdot$ = core, n_2 = cladding) Equation 2.2-1 can be separated into six scalar equations i. components e_x, e_y, e_z, h_x, h_y, and h_z. The Laplacian operator, ∇^2, can be separated into a Laplacian operator transverse to the direction of propagation, ∇_t^2, and a Laplacian operator in the direction of propagation, ∇_z^2, i.e.
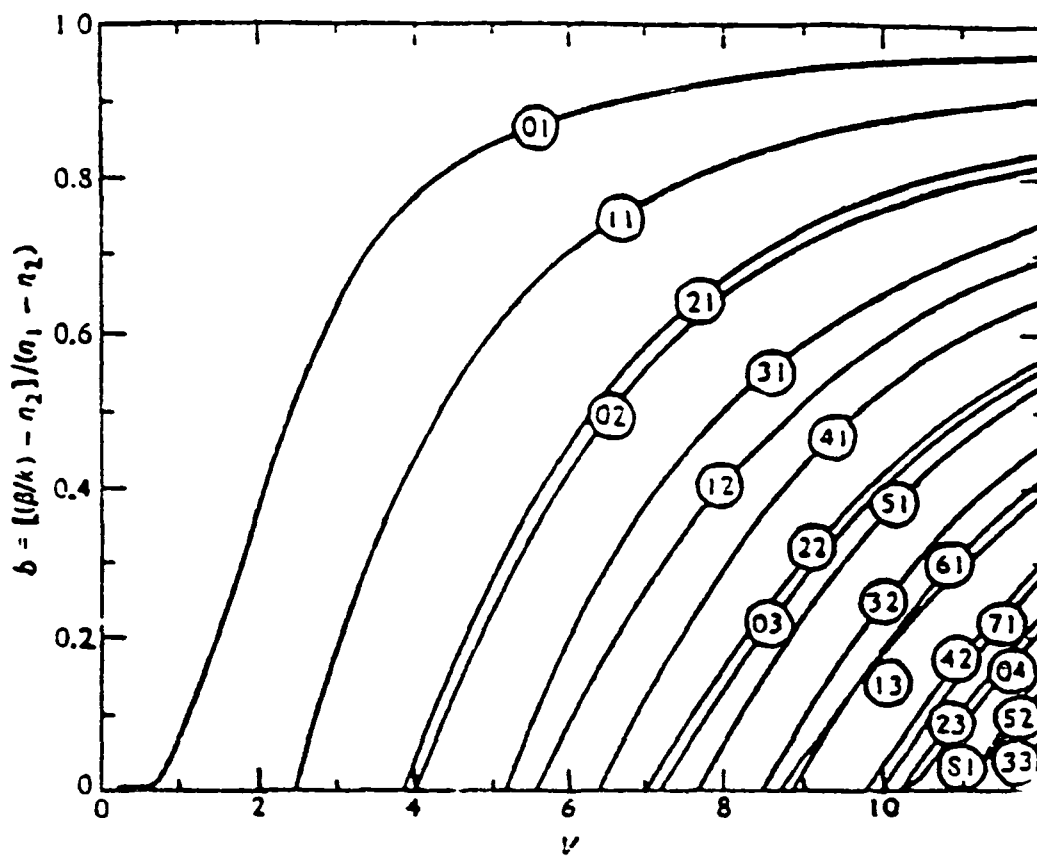
Figure 2. b vs. V-number [5]

$$\nabla^2 = \nabla_t^2 + \nabla_z^2. \qquad (2\,2-2)$$

If the electromagnetic field solutions are solved for the z -component of the electromagnetic field, the r and ρ components of the electromagnetic field can be found from the known z-components These relationships will be defined later, after the field solutions for z -components are established.

The following analysis is for the scalar field component, e, or h, which will be redefined as Ψ, i e

$$\nabla_t^2\Psi + (k_o^2 n^2 - \beta^2)\Psi = 0, \qquad (2.2-3)$$

where β is the propagation constant

Ψ can be described as a function of R and Φ, where R and Φ can be separated, as shown in the following equations.

$$\Psi = R(r)\Phi(\phi), \qquad (2\,2-4)$$

$$\frac{d^2\Phi}{d\phi^2} + \ell^2\Phi = 0, \; and \qquad (2.2-5)$$

$$\frac{d^2R}{dr^2} + \frac{1}{r}\frac{dR}{dr} + \left(q^2 - \frac{\nu^2}{r^2}\right)R = 0, \qquad (2\,2-\text{c})$$

where,

$$q^2 = k_o^2 n^2 - \beta^2. \qquad (2.2-7)$$

The solution to Equation 2 2-5 can be one of the following

$$\Phi = \begin{Bmatrix} A_1 \sin v\varphi \\ B_1 \cos v\phi \\ A_1 \sin v\phi + B_1 \cos v\phi \end{Bmatrix},$$ (2 2 – 8)

and the solution to Equation 2 2-6 inside the core is a Bessel function of the first kind, ı e.

$$R = J_v(q,r), \quad q^2 > 0 \,(\iota\,e.n = n_1).$$ (2.2 – 9)

The solution to Equation 2.2-6 outside the core is a modified Bessel function of the second kind, ı e.

$$R = BK_v(q,r), \quad q^2 < 0 \,(\iota\,e\,n = n_2).$$ (2.2 – 10)

So, for the scalar electric field ın the z-direction inside the core $(r < a)$, the solution f a mode ıs Equation 2.2-11. Simıliar equations hold true for h_z, i.e.

$$e_z = J_v\left(\frac{Ur}{a}\right)\begin{pmatrix} A_1 \sin v\phi \\ B_1 \cos v\phi \\ A_1 \sin v\phi + B_1 \cos v\phi \end{pmatrix}$$ (2.2 – 11)

where

$$q^2 = U^2 = \left(k_o^{\,2} n_1^{\,2} - \beta^2\right)a^2.$$ (2.2 – 12)

For the scalar electric field ın the z-direction in the cladding region $(r < a)$, the solution ıs gıven in Equation 2 2-13 Sımılar equations hold true for h_z, i.e.

$$e_z = K_v\left(\frac{W'r}{a}\right)\left(\begin{array}{c} A_1 \sin v\phi \\ B_1 \cos v\phi \\ A_1 \sin v\phi + B_1 \cos v\phi \end{array}\right) \qquad (2.2-13)$$

where

$$q^2 = W^2 = \left(\beta^2 - k_o^2 n_2^2\right)a^2. \qquad (2.2-14)$$

It is important to note that the $V-number$ can be also defined in terms of U and (Equation 2 2-15).

$$V^2 = U^2 + W'^2 \qquad (2.2-15)$$

Since the field solutions for the z-components of the electromagnetic fields can be determined, the r and ϕ components of the electromagnetic fields can be found in Equations 2.2-16 thru 2.2-19.

$$e_r = -\frac{j}{q^2}\left(\frac{\beta \partial e_z}{\partial r} + \frac{\mu\omega}{r}\frac{\partial h_z}{\partial \phi}\right), \qquad (2.2-16)$$

$$e_\phi = -\frac{j}{q^2}\left(\frac{\beta}{r}\frac{\partial e_z}{\partial \phi} - \mu\omega\frac{\partial h_z}{\partial \phi}\right), \qquad (2.2-17)$$

$$h_r = -\frac{j}{q^2}\left(\beta\frac{\partial h_z}{\partial r} - \frac{\omega\varepsilon}{r}\frac{\partial e_z}{\partial \phi}\right), \text{ and} \qquad (2.2-18)$$

$$h_\phi = -\frac{j}{q^2}\left(\frac{\beta}{r}\frac{\partial h_z}{\partial \phi} + \omega\varepsilon\frac{\partial e_z}{\partial r}\right). \qquad (2.2-19)$$

Usually the modes of the optical fiber are defined in terms of HE_{vm} and EH_{vm}, where v is the order of the Bessel function and m is the root of the v order Bessel function. A specialized classification of these modes are the linearly polarized (LP) modes. These are the modes that will be specified in conjunction with the micro-optical fiber devices.

Linearly polarized modes are electromagnetic fields that are linearly polarized. LP modes need to propagate in fibers that are weakly guiding. Weak guidance is defined by Equation 2.2-20.

$$\Delta = \frac{n_1{}^2 - n_2{}^2}{2n_1{}^2} \cong \frac{n_1 - n_2}{n_1} \qquad (2.2-20)$$

The linear polarization causes degeneracies among the EH_{vm} and HE_{vm} modes [6]. The $LP_{\ell m}$ can be defined in terms of HE_{vm} and EH_{vm} by the following relationships:

$$\ell = v + 1, \qquad (2.2-21)$$

$$for\,\ell \geq 2, \quad LP_{\ell m} = HE_{v+1,m}, \; or \; EH_{v-1,m}, \qquad (2.2-22)$$

$$for\,\ell = 1, \quad LP_{1m} = TE_{0m}, TM_{0m}, or \; HE_{2m}, \; and \qquad (2.2-23)$$

$$for\,\ell = 0, \quad LP_{0m} = HE_{1m}. \qquad (2.2-2\cdot)$$

The solution for the LP modes in the core yields the following:

$$E_x = \frac{J_\ell(Ur/a)}{J_\ell(U)} \begin{pmatrix} \cos \ell\phi \\ \sin \ell\phi \end{pmatrix} \quad and \qquad (2.2-25)$$

$$H_y = Y_1 E_x \qquad (2.2-26)$$

where

$$Y_1 = \sqrt{\frac{\varepsilon_o n_1}{\mu_o}} \,. \qquad (2.2-27)$$

The solution for the LP modes in the cladding similarly yields the following:

$$E_x = \frac{K_\ell(Wr/a)}{K_\ell(W)} \begin{pmatrix} \cos \ell\phi \\ \sin \ell\phi \end{pmatrix} \quad and \qquad (2.2-28)$$

$$H_y = Y_2 E_y \qquad (2.2-29)$$

where

$$Y_2 = \sqrt{\frac{\varepsilon_o n_2}{\mu_o}} \,. \qquad (2.2-30)$$

The LP modes can be decomposed further into even modes denoted by $LP_{\ell m}$, and odd modes denoted by $LP_{\ell m}$. The odd modes are defined by the electric field componen⁺ with the $\cos(\ell\phi)$ term, and the even modes are defined by the electric field compone... with the $\sin(\ell\phi)$ term.

The basic parameters of optical fibers, the mode theory, and the understanding of LP modes will aid in understanding the prinicple of operation of micro-optical fiber devices for fiber sensor applications.

3.0 Modal Domain Sensing

The novel idea of using a single optical fiber's modes instead of an optical fiber interferometer for detecting perturbations (i.e. strain, vibrations, etc.) was discovered by Layton [7] and Kingsley [8]. Using the modes of an optical fiber to glean information about the optical fiber's surroundings will be referred to as modal domain sensing. During the last few years at Virginia Tech a better understanding of the mechanisms behind modal domain sensing and practical implementations of modal domain sensing has been accomplished by Bennett [9], Ehrenfeuchter [1], Srinivas [10], Shankaranarayanan [2], and Duncan [11]. The primary mechanism behind modal domain sensing is the change in the modes' propagation constants due to perturbations to the optical fiber. These changes in the propagation constants cause changes in the modal interference pattern which can be related to the applied perturbations to the optical fiber. Some applications of modal domain sensing thus far are the use of embedded optical fibers in composites to detect acoustic emission [9], optical fibers to detect structural vibrations [1,11], and optical fibers to detect axial strain [2,10,11].

A basic experimantal set-up of a modal domain sensing system is seen in Figure 3. The laser, the lens, and the optical fiber aligner can be considered to "the input optics" for the optical fiber. The optical fiber is the sensing region. At the end of the perturbed optical fiber is the signal processing (the filter) which may be implemented using an out-of-line spatial filter (no optical fibers are used) or an in-line optical fiber as a spatial filter. Chapter 4 will look at some spatial filtering techniques which may be implemented with an optical fiber. After the spatial filtering section is the detection scheme, a photodiode detector feeds an oscilloscope in order to monitor the signal from the modal domain sensor. Then, a computer can be used in conjunction with this system for frequency analysis of the signal

This chapter will examine the phase modulation in an optical fiber introduced by perturbations to the optical fiber; then, the optimum modal interference pattern for modal domain sensing will be reviewed [11].

3.1 Phase Modulation

To understand the phase modulation of the an optical fiber due to perturbations, the phase modulation in one mode will be presented first (i.e. the change in the mode's propagation constant) [12,13].

The transverse electric field solution is defined in Equation 3.1-1.

$$E_t = E_t(r, \phi)e^{j\beta z} \qquad (3.1-1)$$
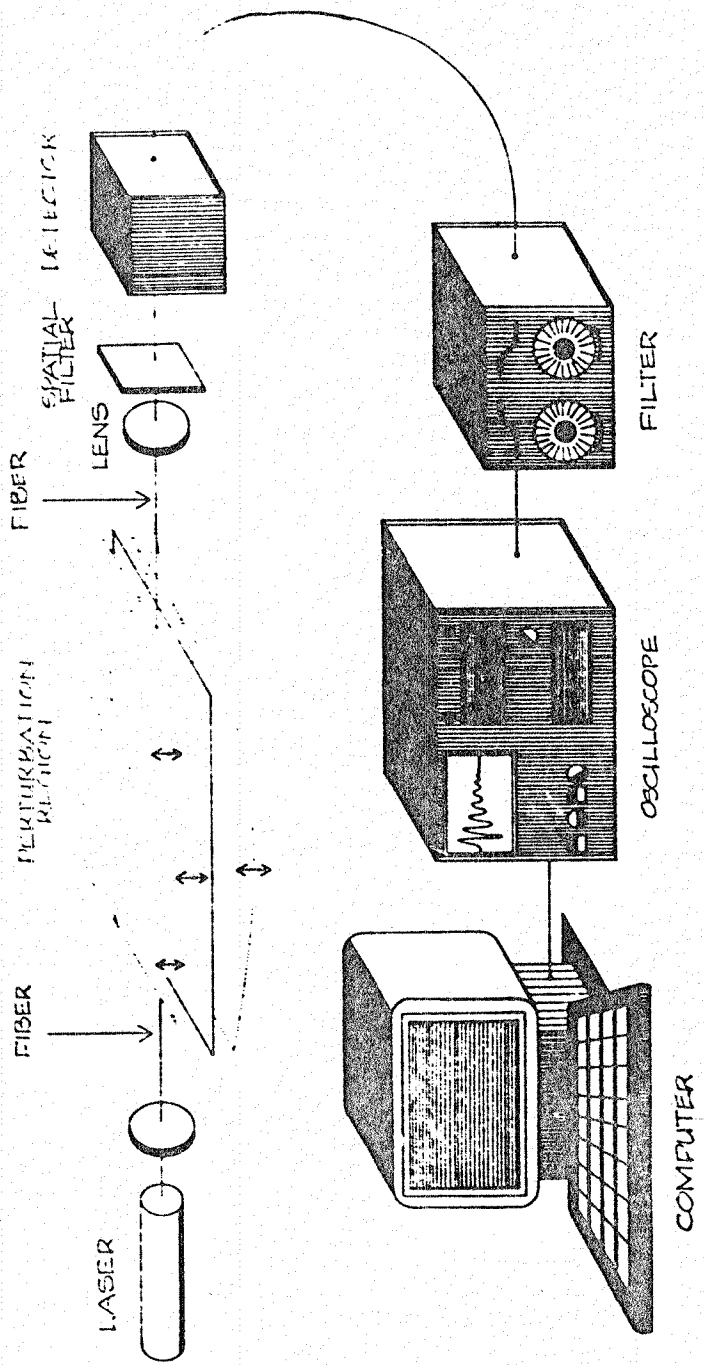
Figure 3. A Modal Domain Sensing Experimental Set-Up

3.0 Modal Domain Sensing

$$= |E_t(r, \phi)| e^{j\beta z + j\psi}.$$

The phase of a mode is defined by Equation 3.1-2.

$$\phi = \beta z + \psi. \tag{3.1 - 2}$$

Here, z is defined as the distance along the as the length of the optical fiber, L . The phase modulation due to a perturbation is represented in Equation 3.1-3.

$$\Delta\phi = \beta\Delta z + z\Delta\beta \tag{3.1 - 3}$$

Equation 3.1-3 is valid for axial strain (ε_z) or small acoustic waves (small vibrations). Δz can be expressed in terms of axial strain and the length of the optical fiber, Equation 3 1-4.

$$\Delta z = \varepsilon_z L, \ for \ axial \ strain \tag{3.1 - 4}$$

$\beta\Delta z$ can be expressed in terms of an isotropic stress due to hydrostatic pressure, P, Poisson's ratio, μ, and Young's modulus, E, as indicated in Equation 3.1-5.

$$\beta\Delta z = \beta\varepsilon_z L = -\frac{\beta(1 - 2\mu)LP}{E} \tag{3 1 - 5}$$

The $\Delta\beta$ term depends on a photoelastic effect and a dimensional effect, Equation 3.1-6 [12,13].

$$\Delta\beta = \left(\frac{\partial\beta}{\partial n}\right)\Delta n + \left(\frac{\partial\beta}{\partial D}\right)\Delta D \tag{3.1 - 6}$$

where,

3.0 Modal Domain Sensing

n = *refractive index*

β = *longitudinal propagation constant*

D = *diameter of the core.*

Equation 3 1-6 can be decomposed further by expanding the Δn term, Equation 3.1-7 [12,13].

$$\Delta n = -\frac{n^3}{2}[\varepsilon_z(1-\mu)P_{12} - \mu\varepsilon_z P_{11}] \qquad (3.1-7)$$

where,

ε_z = *axial strain*

μ = *Poissons* ratio

P_{11}, P_{12} = *photoelastic constants.*

It is important to note that for small changes in the index of refraction, i.e. the difference between the core and the cladding indices of refraction is slight, an effective index of refraction, n_{eff}, can be considered to be equal to n_1 and to n_2 (Equation 3.1-8).

$$n_{eff} \cong n_1 \cong {}_2 \qquad (3.1-8)$$

So $\frac{\partial\beta}{\partial n}$ can be approximated as indicated in Equation 3.1-9.

$$\frac{\partial\beta}{\partial n} \cong k_o = \frac{2\pi}{\lambda_o} \qquad (3.1-9)$$

For the second term in Equation 3.1-6 changes in phase due to changes in the diameter, ΔD, can be expanded into the following

$$\Delta D = \mu \varepsilon_z D \qquad (3.1-10)$$

Also, the term $\dfrac{\partial \beta}{dD}$ can be rewritten as Equation 3.1-11

$$\frac{\partial \beta}{dD} = \frac{V^3}{2\beta a^3} \frac{\partial b}{aD} \qquad (3.1-11)$$

However, the change in phase due to changes in the diameter is negligible compared to $\dfrac{\partial \beta}{dn} \Delta n$, so the second term in Equation 3.1-6 can be neglected.

Finally, $\Delta \phi$ due to changes in the propagation constant from external perturbations applied to the optical fiber can be rewritten as Equation 3.1-12 [12,13].

$$\Delta \phi = \varepsilon_z L \left\{ \beta - \frac{\beta n^2}{2} [(1 - \mu)P_{12} - \mu P_{11}] \right\} \qquad (3.1-12)$$

3.2 Differential Phase Modulation

For the few-moded optical fibers and the micro-optical fiber devices that are used with modal domain sensing an understanding of the differential phase modulation between the propagating modes when external perturbations are applied to the optical fiber is essential. Since the optical fibers used in the experiments for modal domain sensing support two modes, differential phase modulation for two modes will be considered. The

reason why a mode combination of two modes is used with modal domain sensing will be explained in Section 3 3.

The difference in phase under static conditions can be defined as ϕ_{12} (Equation 3.2-1), where 1 is for the first mode and where 2 is for the second mode.

$$\phi_{12} = \phi_1 - \phi_2 \qquad (3.2-1)$$

For applied perturbations to the few-moded optical fibers Equation 3 2-1 becomes Equation 3 2-2.

$$\phi_{12} + \Delta\phi_{12} = [\phi_1 + \Delta\phi_1] - [\phi_2 + \Delta\phi_2] \qquad (3.2-2)$$

The differential phase modulation is described by Equation 3 2-3.

$$\Delta\phi_{12} = [\phi_1 + \Delta\phi_1] - [\phi_2 + \Delta\phi_2] + \phi_{12} \qquad (3\ 2-3)$$

Equation 3 1-12 can be restated for differential phase modulation between two modes, and Equation 3.2-2 can be written in the form of Equation 3.1-12.

$$\Delta\phi_{12} = \Delta z \Delta\beta_{12} \qquad (3.2-4)$$

where,

$$\Delta\beta = \beta_{12},$$

$$\beta_{12} = \beta_1 - \beta_2,$$

$$\Delta\phi_{12} = \varepsilon_z L \left\{ \beta_{12} - \frac{\beta_{12} n^2}{2} [(1-\mu)P_{12} - \mu P_{11}] \right\}. \qquad (3.2-5)$$

This is the differential phase modulation between two modes. This differential phase modulation is important for the amplitude modulation of the electric field intensity. The intensity will be explained for the optimum modal pattern in the following section

3.3 The Optimum Modal Pattern

Recently, there has been a great deal of research to determine an easily characterizeable modal interference pattern. This modal interference pattern needs to be easy to generate. Changes in the modal interference pattern need to be correlated with external perturbations applied to the optical fiber.

It has been proven by Duncan [11] that the modes that produce the optimum interference pattern is the x- polarized even LP_{01} and LP_{11} modes, Figure 4 [11]. This modal interference pattern meets the two requirements mentioned earlier. This pattern is quite easy to generate, and as this pattern is perturbed the two lobes exchange power. This exchange in power between the two lobes can be correlated to external perturbations being applied to the optical fiber. A sensing system using this modal interference pattern can achieve a system sensitivity for strain of 10^{-9} [11] Changes in intensity for a modal domain sensing system using the LP_{01} and LP_{11} modal interference pattern need to be reviewed.
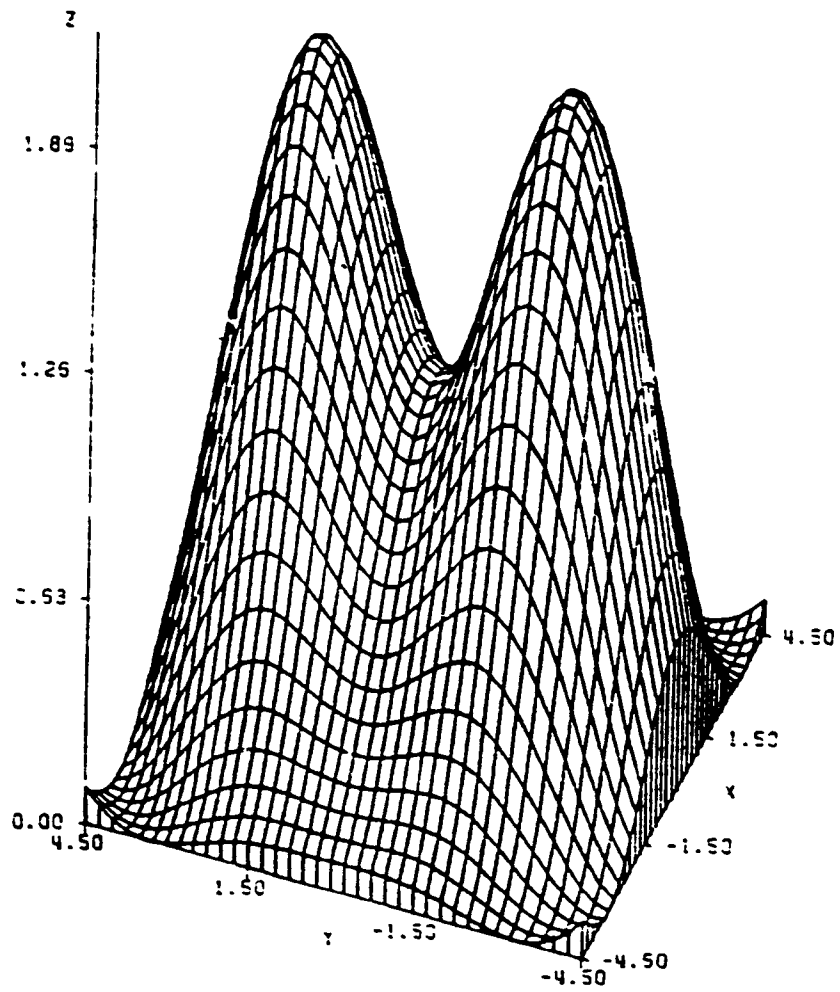
Figure 4. Interference Pattern: LP_{01} and LP_{11} Modes [11]

3.0 Modal Domain Sensing

3.3.1 Intensity of the LP_{01} and LP_{11} Modes

The fields in the core of the optical fiber, the LP_{01} and LP_{11} modes, are defined respectively in Equations 3.3.1-1 and 3.3.1-2.

$$E_x = A_1 J_0(U_0 r/a) \tag{3.3.1 - 1}$$

$$H_y = A_1 Y_1 J_0(U_0 r/a)$$

$$E_x = A_2 J_1(U_1 r/a) \cos \phi \tag{3.3.1 - 2}$$

$$H_y = A_2 Y_1 J_1(U_1 r/a) \cos \phi$$

The fields for the LP_{01} and LP_{11} modes in the cladding are defined respectively by Equations 3.3.1-3 and 3.3.1-4.

$$E_x = A_1 K_0(W_0 r/a) \tag{3.3.1 - 3}$$

$$H_y = A_1 Y_1 K_0(W_0 r/a)$$

$$E_x = A_2 K_0(W_0 r/a) \cos \phi \tag{3.3.1 - 4}$$

$$H_y = A_2 Y_1 K_0(W_0 r/a) \cos \phi$$

Now, the total fields in the core can be described by Equation 3.3.1-5.

$$\vec{E}_x = (A_1 J_0(U_0 r/a) e^{-j(\beta_{01} - \psi_c)} + A_2 J_1(U_1 r/a) \cos \phi e^{-j(\beta_{11} - \psi_{11})}) \hat{a}_x \tag{3.3.1 - 5}$$

$$\vec{H}_y = (Y_1 E_x) \hat{a}_y$$

ψ_{01} and ψ_{11} are random phase terms

It is important to note at this point that the amplitudes of the fields A_1 and A_2, are undetermined. At this point the amplitudes to the LP_{01} and LP_{11} can not be determined from the launching conditions. The work based on these amplitudes will be relative to the modes, because the modal amplitudes cannot be determined explicitly.

Intensity for the electromagnetic fields is found in Equation 3.3.1-6.

$$ I = \frac{1}{2} Re\left\{ (E_x \hat{a}_x \times Y_1 E_x^* \hat{a}_z) \cdot \hat{a}_z \right\} = \frac{1}{2} Y_1 |E_x|^2 \qquad (3.3.1-6) $$

By substituting Equation 3.3.1-5 into Equation 3.3.1-6, Equation 3.3.1-7 is obtained.

$$ I = I_o \left\{ A_1^2 J_0^2(U_0 r/a) + A_2^2 J_1^2(U_1 r/a)[\cos\phi]^2 + \right. $$
$$ \left. A_1 A_2 J_0(U_0 r/a) J_1(U_1 r/a) \cos(\Delta\beta z - \Delta\psi) \cos\phi \right\} \qquad (3.3.1-7) $$

where,

$$ I_o = \frac{Y_1}{2}, $$

$$ \Delta\beta = \beta_{01} - \beta_{11}, $$

$$ \Delta\psi = \psi_{01} - \psi_{11} $$

By examining Equation 3 3.1-7 the first term of this intensity equation is the intensity of the LP_0, mode, Figure 5 [11]. The second term in the intensity equation is the intensity of the LP_{11} mode, Figure 6 [11]. The third term in the intensity equation is the interference of the LP_{01} and the LP_{11} modes. The third term is defined as the "cross

term." The cross term is a cosine function as seen in Figure 7 when this term is a maximum [11].

Equation 3.3 1-7 can be rewritten as Equation 3.3.1-8 as a series of functions dependent on $\bar{r}$, ϕ, and z, i e.

$$I = I_o\{I_1(\bar{r}) + I_2(\bar{r}, \phi) + I_3(\bar{r}, \phi, z)\}. \qquad (3.3.1-8)$$

The intensity of the LP_{01} and LP_{11} modes when $I_3 = 0$ is displayed in Figure 4.

The assumption for the rest of this paper is that $A_2 = 2A_1$. This assumption will enhance the changes in intensity due to applied perturbations. If $\dfrac{A_2}{A_1}$ is less than 1 then the LP_{01} term will dominate, and a single bright spot will be present at the output. If $\dfrac{A_2}{A_1}$ is much greater than one, little power will exist in the LP_{01} mode, and minimal interference between the two modes will occur as perturbations are applied to the optical fiber [11].

3.3.2 Intensity Modulation

In modal domain sensing the main focus is the behavior of Equation 3.3 1-7 as perturbations are applied to the optical fiber. The third term of Equation 3.3.1-7 is affected by the perturbations to the optical fiber. When $I_3 = 0$, the LP_{01} and the LF_{11} intensity are as displayed, respectively in Figures 5 and 6. As the optical fiber is perturbed to the point where I_3 is a maximum, there is an exchange of power between the two lobes as shown in Figure 8 [11] In Figure 8 one lobe is a maximum while the other lobe is a minimum.
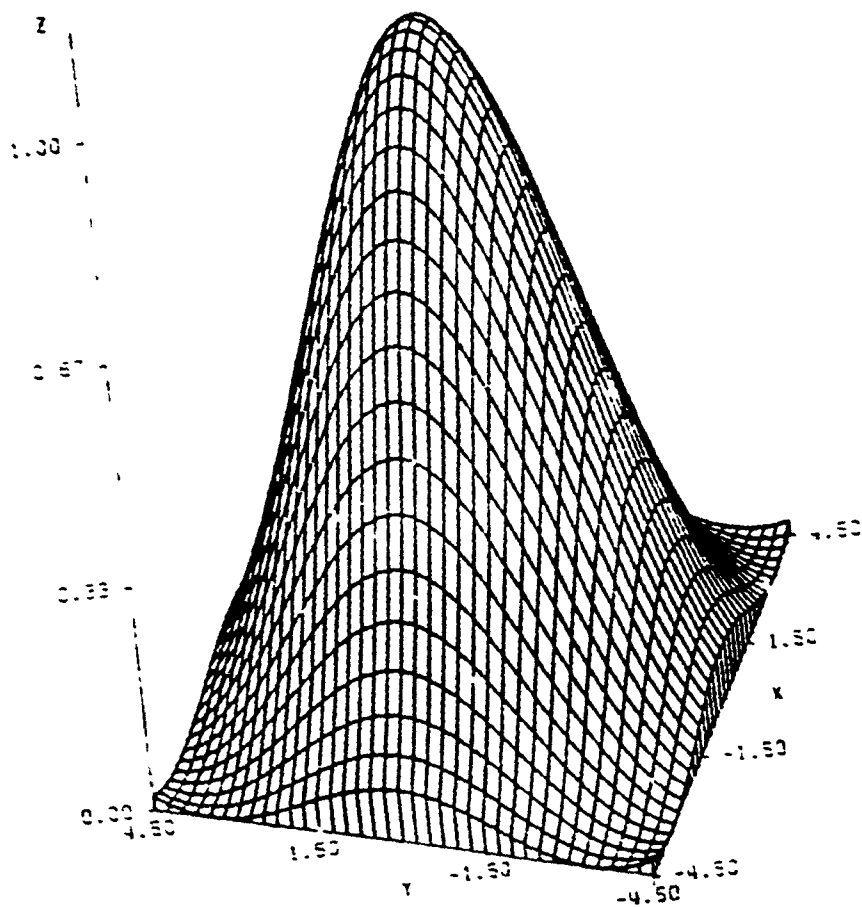
Figure 5. Intensity of the LP01 Mode [11]

3 0 Modal Domain Sensing

ORIGINAL PAGE IS
OF POOR QUALITY
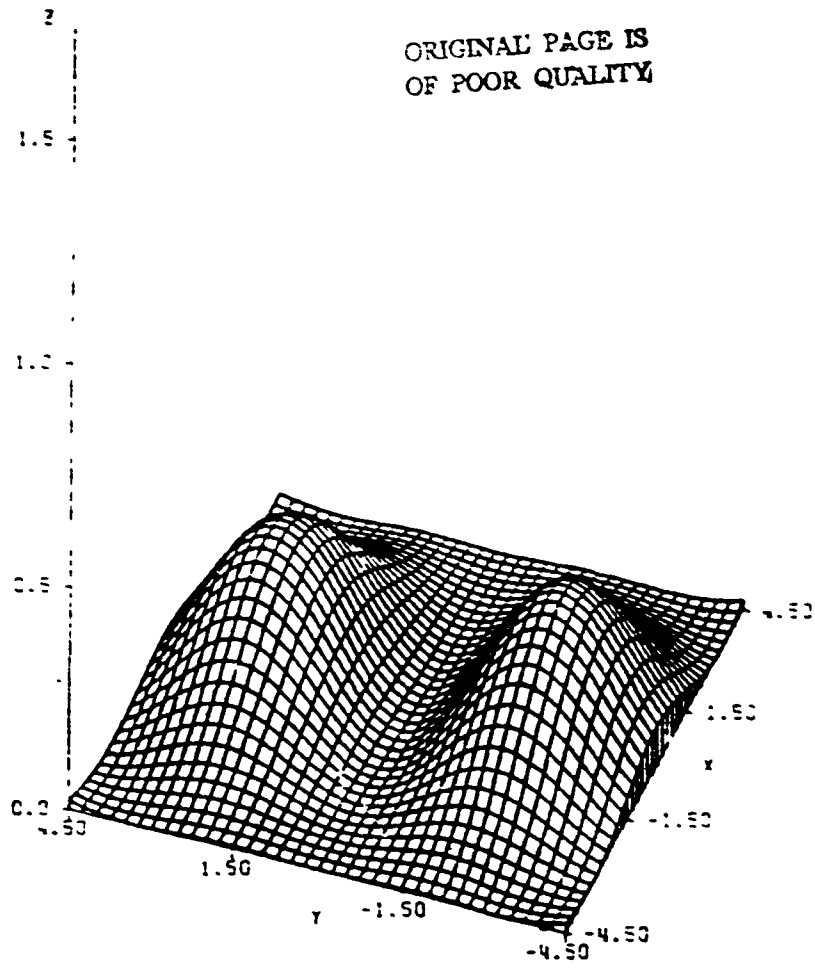
Figure 6.   Intensity of the LP$_{11}$ Mode [11]

3.0 Modal Domain Sensing

26
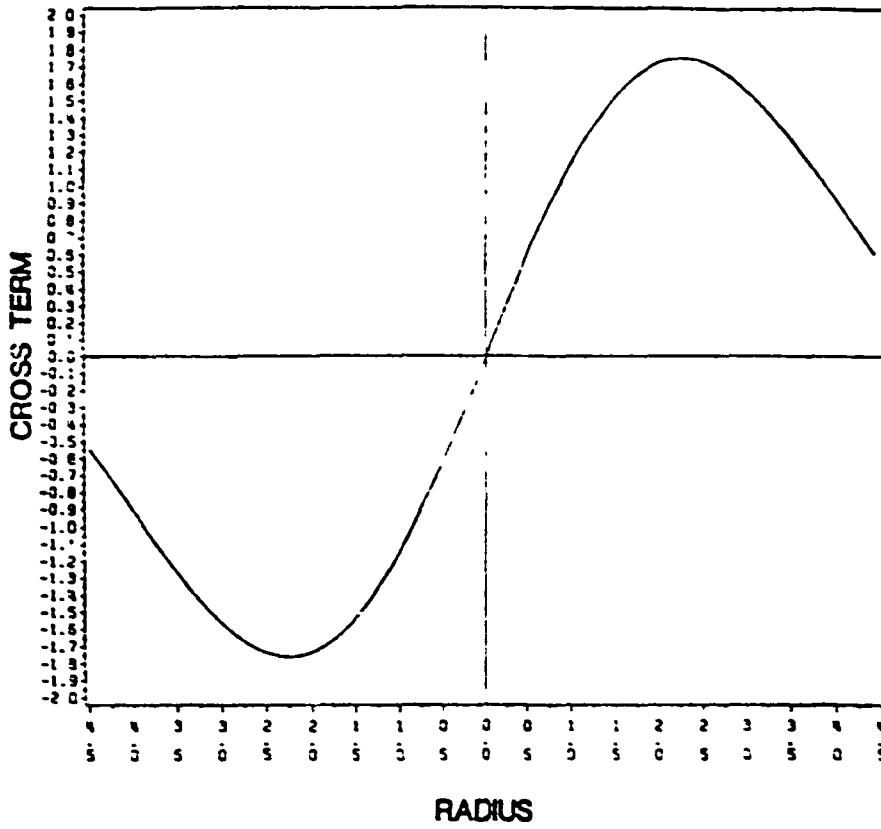
CROSS TERM

Figure 7. The Cross Term at a Maximum [11]

TOTAL INTENSITY
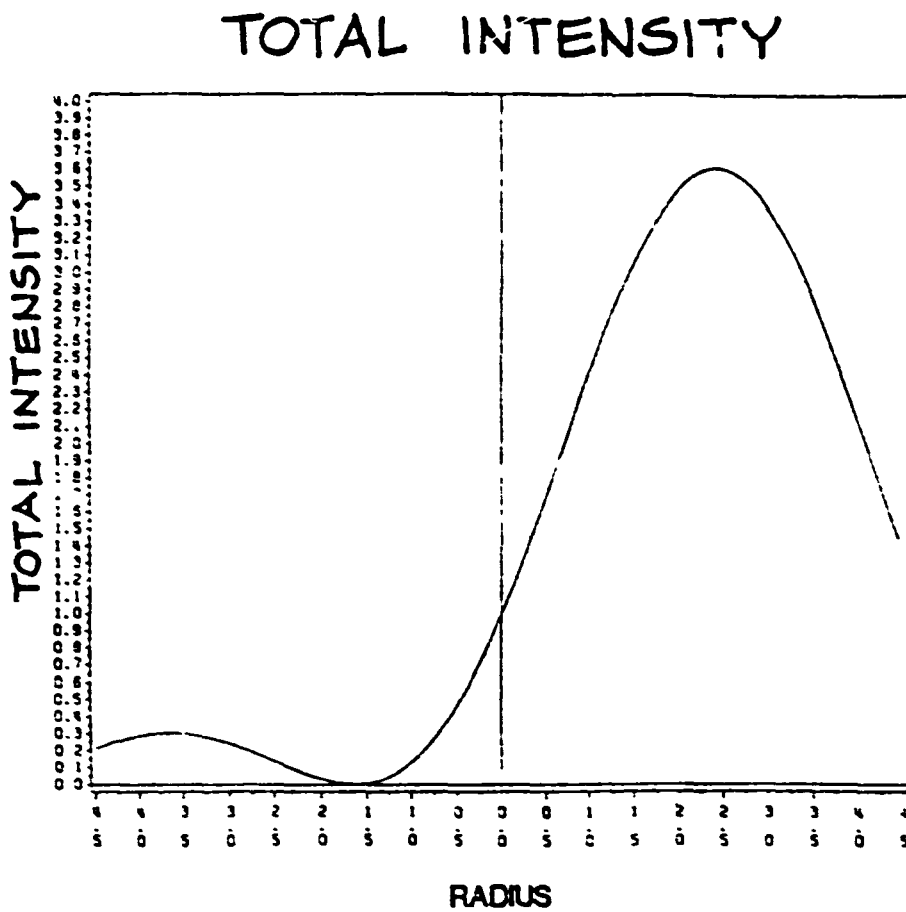
Figure 8. One Lobe Is A Maximum While The Other Is A Minimum [11]

The cross term intensity, $I_3(\bar{r}, \phi, z)$, causes a sinsusoidal oscillation between the two lobes as the optical fiber is perturbed. This change in intensity can be related to an applied strain for an applied axial strain or for small amplitude sinusoidal strain.

In the $I_3(r, \phi, z)$ term the differention phase modulation between two modes from Section 3.2 can be applied to the $\Delta\beta$ term. The intensity equation, Equation 3.3.1-8, can be rewritten as Equation 3.3.2-2 by applying the following trigonometric identity:

$$1 + \cos 2x = 2[\cos x]^2, \qquad (3\ 3.2-1)$$

$$I = I_o''\{1 + \cos(\Delta\beta z - \Delta\psi)\}, \qquad (3.3.2-2)$$

$$I = I_o'''\left\{ \cos\left(\frac{\Delta\beta z - \Delta\psi}{2} \right) \right\}^2.$$

I_*'' consists of I_*, $I_1(\bar{r})$ and $I_2(\bar{r}, \phi)$ from Equation 3.3.1-8, and $I_*''' = 2I_*''$.

The phase modulation between two modes from Section 3.2, Differential Phase Modulation, can be applied to the $\Delta\beta z$ term. Δz can be defined as a function of strain where

$$\Delta z = \varepsilon_z z, \ where \qquad (3\ 3.2-3)$$

$z = L_f$, *the length of the optical fiber, and*

ε_z = *axial strain in the z − direction*

Equation 3.3.2-2 can be explained as a function of strain, i e.

$$I = I_o''' \left[\cos\left(\frac{\Delta\beta(x)\varepsilon_z L_f - \Delta\psi}{2} \right) \right]^2, \qquad (3.3.2-4)$$

where x is optical fiber parameters related to the phase modulation, i.e. indices of refraction, photoelastic constants, Poisson's ratio.

A change in intensity, ΔI, can be directly related to a change in an applied axial strain (Equation 3.3 2-5). Assume that $\Delta\psi = \frac{\pi}{2}$ [11].

For axial strain:

$$\Delta I(\Delta\varepsilon_z) = \frac{\partial}{\partial\varepsilon_z} I(\varepsilon_z) = \frac{I_o'''}{2} x\Delta\beta L_f \Delta\varepsilon_z. \qquad (3.3.2-5)$$

For small amplitude sinsusoidal axial strain:

$$\Delta I(\Delta\varepsilon_{z\,peak}, t) = \frac{I_o'''}{2} (x\Delta\beta L_f)\Delta\varepsilon_{z\,peak} \cos \omega t. \qquad (3.3.2-6)$$

$\Delta\varepsilon_{z\,peak}$ is the peak of the sinusoidal strain and ω is the frequency of the sinusoidal strain. Equation 3.3.2-6 means that there are sinusoidal variations in intensity when the bending of a vibrat ng structure is quite small.

Theoretically, Duncan has shown that the minimum detectable axail strain, $\Delta\varepsilon_n$ is 0 3x10^{-9} by a PIN diode and is 2x10^{-12} by an Avalanche PIN diode (APD), which is the shot noise limit of the detector.

Two of the micro-optical fiber devices presented in this paper will be discussed in conjunction with the ideas presented in this chapter, modal domain sensing

4.0 Principles of Operation of Micro-Optical Fiber Devices

Three micro-optical fiber devices will be considered: the modal conversion coupler, the asymmetrical splice and an air-gap splice. Two of these devices, the modal conversion coupler and the asymmetrical splice can be used for signal processing in conjunction with modal domain sensing. The third micro-optical fiber device, the air-gap splice, detects modal effects in multimode step-index optical fibers. The air-gap splice is used with Optical Time Domain Reflectometry (OTDR) techniques to detect localized changes in strain.

4.1 Modal Conversion Coupler

A modal conversion coupler is a fused biconical taper coupler that is not made to split power in a $50-50$ ratio, but uses the taper and the coupler region to generate new

modes at the one of the coupler's output arms. The modal conversion coupler that was fabricated in the Fiber and Electro-Optics Lab by Kent Murphy is shown in Figure 9.

A similiar device, a modal filter, has been fabricated by Sorin, Kim, and Shaw [14]. This device is shown in Figure 10. This device is an optical fiber coupler fabricated from a dual core optical fiber and a single mode optical fiber. This device uses an applied acoustic wave to couple between the LP_{01} and the LP_{11} modes. This system can then generate the LP_{11} mode from the LP_{01} mode. However, this system is not entirely optical like the modal conversion coupler and requires external perturbations to induce modal conversion.

The all optical modal conversion coupler was fabricated from a $9\mu m$ core optical fiber, which is single mode at $1300nm$. The modal conversion optical fiber coupler was excited at $633nm$ using a Helium - Neon (HeNe) laser. At $633nm$ the $V - number$ for this optical fiber is 4.467. At this $V - number$ this optical fiber supports the following modes: HE_{11}, HE_{21}, HE_{12}, EH_{11}, and HE_{21} [5]. This optical fiber also supports the degeneracies of these modes, the x- and y- polarizations of the these modes and the TE and TM modes. The modes that are launched into the optical fiber depend on the launching conditions.

As seen in Figure 9, the EH_{11} and HE_{31} modes plus minor amounts of some other modes are launched into Arm 1 [15]. Arm 1-3 is one optical fiber, and Arm 2-4 is the other optical fiber, the coupled optical fiber. In Arm 3 another mode combination is generated. This optical fiber has the HE_{12} mode and probably some of the HE_{11} mode [15]. These two modes were deduced to be present experimentally by observing the concentricity of the far field pattern. Arm 4 has another mode combination, but the signal in this arm is about 10 dB down in power from that in Arm 3. Therefore, this
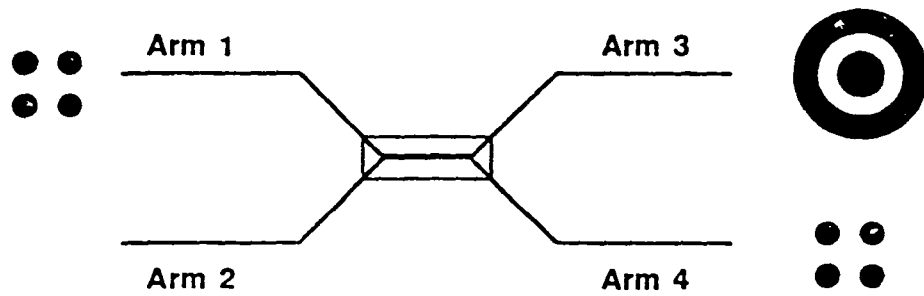
Figure 9. A Modal Conversion Coupler

Mode   Polariza⁻ᵒⁿ
Strippᵉʳ   Contrᵉ ᵉˡ

LP̲̲⁻

Mod̲ᵃˡ Fⁱˡter
Coupⁱer

(parallel fⁱbers
ⁱⁿ a
dⁱrecᵗⁱoⁿal coupᵉr)

Sⁱⁿgˡe ̲ ̲aˡᵉ Fⁱⁿer

Dcuble Moded Fiber

(suppᵤ₋rts tʰe
LP01 and LP11
modᵉs)

O̲⁻ᵗᵖ̲̲
ᵗ⁻ᵉ LP̲̲
⁻ᵍᵈ⁻

Cᵤ₋ᵗput
ᵗʰe LP1ᵢ
⁻ᵗode
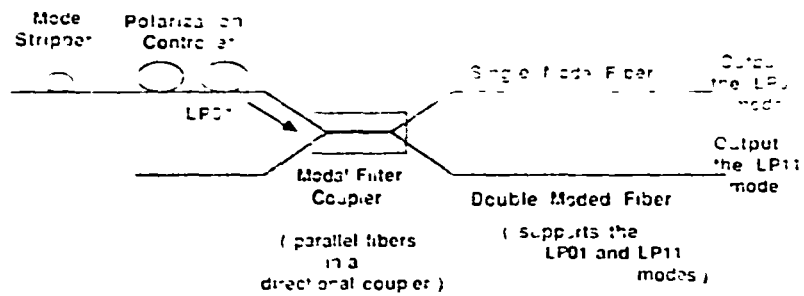
Figure 10.   A Modal Filter [14]

coupler converts modes in the input arm, Arm 1, to other modes in the output arm, Arm 3

How this coupler converts modes is qualitatively described. In the coupler region, the $V-number$ becomes quite large, and new modes are generated in this region. At both ends of the coupler is a taper region. In this taper region higher modes are lost due to the decrease in the $V-number$. Due to the combination of new modes being generated in the coupler region and modes being lost in the taper regions, some new modal combinations, which are different than the input modal combinations, can propagate in the $9\mu m$ optical fiber. This modal conversion coupler is a method of creating other modes from a given set of input conditions

4.2 An Asymmetrical Optical Fiber Splice

This micro-optical device is used for signal processing in modal domain sensing systems This splice is designed to work in conjunction with the LP_{01} and LP_{11} x-polarized even modal combinations. As strain is applied to the optical fiber, the two lobes exchange power. The asymmetrical splice is designed to collect the change in intensity of one lobe of the speckle pattern as shown in Figure 11. The intensity changes in the filtering optical fiber can be correlated to perturbations applied to the sensing optical fiber.

One way this asymmetrical splice can be fabricated is shown in Figure 12. The filtering fiber is identical to the sensing fiber, but the filtering fiber is laterally offset with respect

LPO and LP11
modes

Sensing Fiber | Asymmetrical Splice | Filtering Fiber

CLAD

The splice filters
one mode from the
sensing fiber
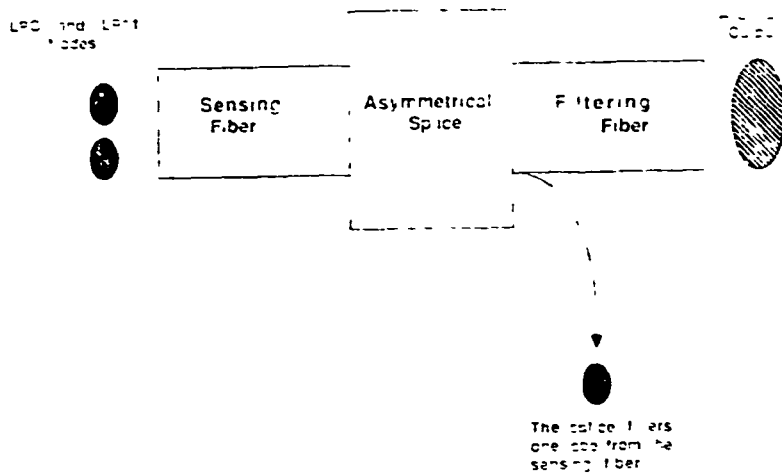
Figure 11. An Asymmetrical Splice for Modal Domain Sensing

to the sensing fiber. The offset filter fiber can detect the intensity changes of one lobe of the LP_{01} and LP_{11} modal pattern due to perturbations applied to the sensing fiber

Another method of achieving this same effect is to have the filtering fiber's core diameter be one half of the sensing fiber's core diameter as in Figure 13. The filtering fiber's core then will sit inside of the sensing fiber's core.

4.2.1 Analysis of Laterally Offset Optical Fiber Splices

To analyze this asymmetrical splice problem for few-moded optical fibers, one may want to apply the standardized splice loss formulas for multimode optical fibers which are reviewed in Section 4.2.2 Alternatively, one may want to apply standardized splice loss formulas for single mode optical fibers which are reviewed in Section 4.2.3. This splice problem is neither in the single mode nor the multimode regime. A method for evaluating lateral splice losses for few-modes optical fibers is developed in Section 4.2.4.

4.2.2 Laterally Offset Splices for Multimode Optical Fibers

For multimode optical fibers ($V > 10$) the anaylsis of the laterally offset splice is based upon the fact that many modes propagate in the sensing fiber and the filtering fiber. The number of modes that propagate in a multimode optical fiber can be approximated by Equation 4.2.3-1 [5]

$$M = \frac{V^2}{2}.$$

$$(4.2\,2-1)$$

Sensing fiber's core radius   Filtering fiber's core radius
         is a_s is a_f
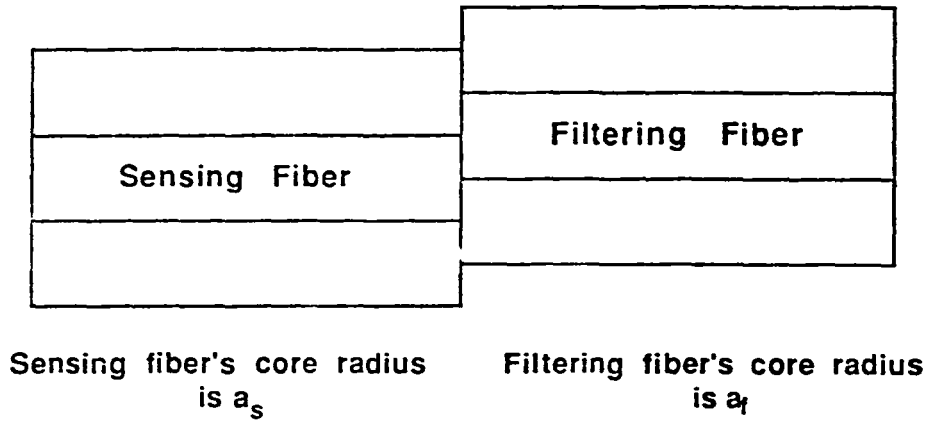
$$a_s = a_f$$

Figure 12. Two Identical Fibers Laterally Offset

Sensing Fiber
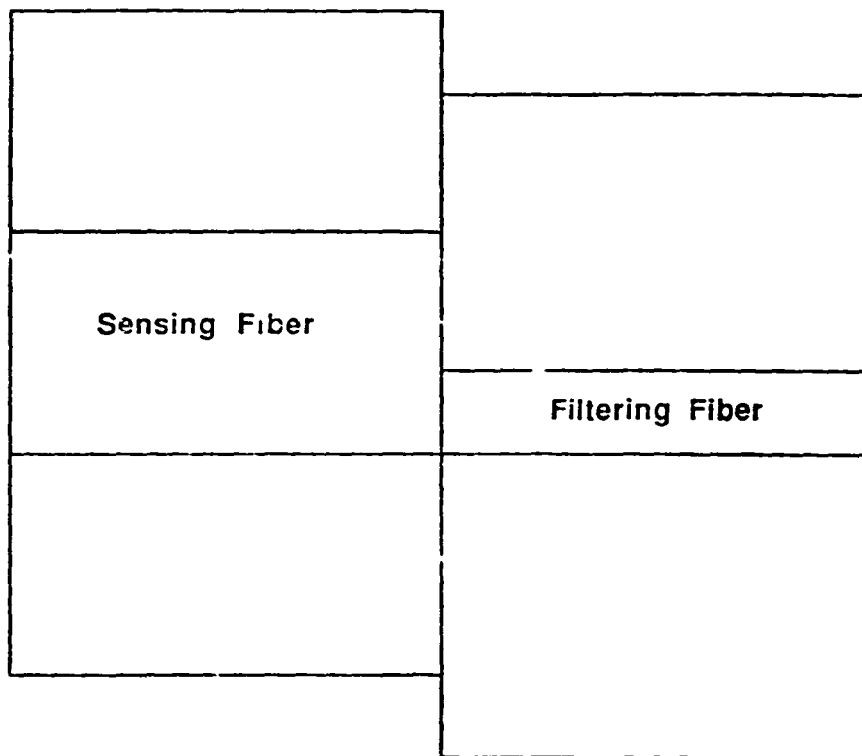
Filtering Fiber

Sensing fiber's core
radius is a_s

Filtering fiber's core
radius is a_f

a_s is at least 2 times
greater than a_f

Figure 13. The Filtering Fiber's Core Inside The Sensing Fiber's Core

Lateral displacement between two optical fibers can be approximated as Equation 4 2 2-2 [5]

$$\eta = \frac{A_{corn}}{\pi a^2} = \frac{2}{\pi}\cos^{-}\left(\frac{d}{2a}\right) - \frac{d}{\pi a}\left\{1 - \left(\frac{d}{2a}\right)^2\right\}^{1/2},$$ (4 2.2 − 2)

where,

$a = core\ radius$,

$d = lateral\ offset$,

$A_{comn} = common\ core\ area\ between\ the\ sensing\ and\ the\ filtering\ fiber$

$$= 2a^2\cos^{-}\left(\frac{a}{2a}\right) - \frac{d}{\pi a}\left\{1 - \left(\frac{d}{2a}\right)^2\right\}^{1.}$$

This formula can also be applied to two fibers of slightly different sizes except $A_{comn} = \pi a_1^2$, where a_1 is the core radius of the filtering fiber. For the asymmetrical splice for the LP_{01} and LP_{11} modes, these formulas cannot be applied. The few-moded optical fiber is not operating in the true "multimode regime". The $V - number$ that supports the propagation of only the LP_{01} and LP_{11} modes falls between 2.405 and 3 9.

4.2.3 Laterally Offset Splices for Singlemode Optical Fibers

For singlemode optical fibers ($V < 2.405$) the propagating electromagnetic wave can be modeled as a Gaussian beam. The splice losses can be defined in terms of the beam

waist, w. The loss in a single mode splice due to a transverse offset can be defined by Equation 4.2 3-1 [16].

$$\eta = 4.34\left(\frac{d}{w}\right) (dB).$$ (4.2.3 – 1)

where,

d = transverse offset distance between the filtering fiber and the sensing fiber, and

w = waist of the Gaussian beam.

If two different optical fibers (i.e. different core radii) are used for the asymmetrical splice, mode field radius mismatch needs to be considered. The mode field radius is defined as the beam width of the Gaussian beam [16]. This splice loss is defined in Equation 4.2.3-2.

$$\eta = -10\log\left[\frac{4 w_T^2 w_R^2}{\left(w_T^2 + w_R^2\right)^2}\right]$$ (4.2.3 – 2)

where,

w_T = waist of the Gaussian beam of the filtering fiber, and

w_R = waist of the Gaussian beam of the receiving fiber.

For the asymmetrical splice that supports the LP_{21} and LP_{11} modes cannot be modeled as a Gaussian beam These modes do not fall in the single mode regime of operation ($V < 2.405$). Another method needs to be developed for few-moded optical fibers. This method will be presented in the following section.

4.2.4 Laterally Offset Splices for Few-Moded Optical Fibers

This problem needs to be solved by working with the individual modes. The methods for splice loss evaluation developed for single mode or multimode fibers cannot be applied to few-moded fibers. Another method for evaluation is presented in this section.

For the few-moded sensing fiber, it is assumed that the LP_{01} and the LP_{11} modes are propagating in the core

$$\vec{E}_{sensing} = [A_0 J_0(U_0 r/a)e^{-j\beta_0 z} + A_1 J_1(U r/a)\cos\phi e^{-j\beta_1 z}]\hat{a}_x.\qquad (4.2\,4-1)$$

The fields that are propagating in the sensing fiber's cladding are defined by Equation 4.2.4-2.

$$\vec{E}_{sensing} = [B_0 K_0(W_0 r/a)e^{-j\beta_0 z} - B_1 K_1(W_1 r/a)\cos\phi e^{-j\beta_1 z}]\hat{a}_x.\qquad (4\,2.4-2)$$

The interface of the splice is shown in Figure 14. Both fibers are identical in this configuration. At this point each fiber will be referred to its own coordinate system. The sensing fiber will be defined in terms of unprimed coordinates: r, ϕ, z. The filtering fiber will be defined in terms of primed coordinates: r', ϕ', z'.

A method of determining the amount of power which is received by the filtering fiber is to determine the modes propagating in the filtering fiber from the sensing fiber, and then an intensity in the filtering fiber can be determined. A ratio of intensity between the filtering fiber and the sensing fiber can be expressed as Equation 4.2.4-3.

$$\eta = \frac{I_{filtering\,fiber}}{I_{sensing\,fiber}}.\qquad (4\,2.4-3)$$
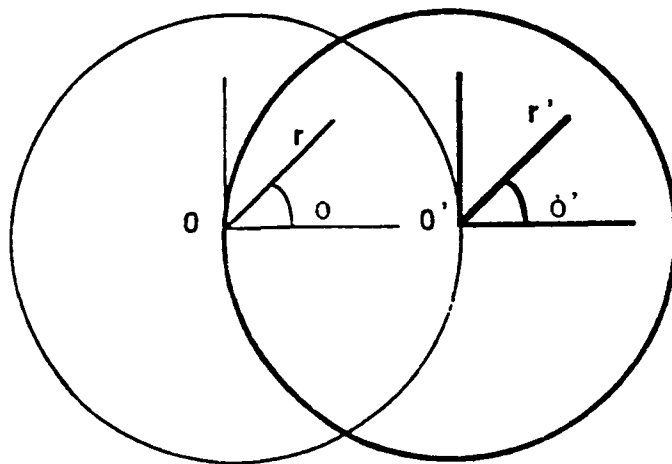
r ,o — sensing fiber
r',o' — filtering fiber

Figure 14. Cross-Section of the Asymmetrical Splice with Identical Fibers

This ratio is the efficiency of the splice.

Another loss across the interface is reflection losses, i.e. loss due the to index of refraction mismatch Since $n_1 \cong n_2$, the transmission across the interface will be approximated as 1 .

Since weak guidance is assumed because the *LP* modes are dependent on the weak guidance condition, the modal amplitudes in the second fiber can be determined from the propagating modes in the sensing fiber [17]

$$A_f = \frac{\int_S \left(\sum_{=0}^{\infty} f_s(r) \cos(s\phi) \right) f_k(r') \cos(f\phi') r' dr' d\phi'}{\int_s |f_f(r') \cos(f\phi)|^2 r' dr' d\phi'} \qquad (4.2.4-4)$$

where,

$$f_s(r) = \begin{cases} A_s J_s(U_s r/a), \ r < a \\ B_s K_s(W_s r/a), \ r > a \end{cases},$$

$$f_f = \begin{cases} J_f(U_f r'/a), \ r < a \\ K_f(W_f r'/a), \ r > a \end{cases}, \text{ and}$$

S = *the surface area to be integrated.*

In Equation 4.2.4-4 $f_s(r) \cos(s\phi)$ are the modes propagating in the sensing fiber. A_s and B_s are the amplitude coefficients associated with the modes in the sensing fiber. $f_f(r') \cos(f\phi')$ are the modes propagating in the filtering fiber. A_f is the resultant modal amplitude associated with the $f_f(r') \cos(f\phi')$ mode. The denominator of Equation 4.2.4-4

is a normalization factor of the $f(r')$ $\cos(f\phi')$ mode   The area which is to be integrated

over is the filtering fiber or the primed coordinates   The unprimed coordinates need to

be converted to primed coordinates in order to perform this integration   This operation

will be performed later

As seen in Figure 14, there are three distinct areas of integration·

1   the sensing core - the filtering core interface,

2   the sensing cladding - the filtering core interface, and

3   the sensing cladding - the filtering cladding interface.

It is important to note that each of these three integrations needs to be performed twice.

Since the LP_{21} and the LP_{11} modes are propagating in the sensing fiber, some of these

modes will be coupled into the LP_{01} and the LP_{11} modes in the filtering fiber. So a modal

amplitude integration needs to be performed for the LP_{01} and LP_{11} modes in each of these

three areas. These integrations are defined as follows:

1   The sensing core - filtering core interface

$$A_{f01} = \frac{\left\{\int_S [A_{s01}J_0(U_{0s}r/a)J_0(U_{0f}r'/a) + \; A_{s11}J_1(U_{1s}r/a)\cos\phi J_0(U_{0f}r'/a)]r'dr'd\phi'\right\}}{\int_S |J_0(U_{0f}r'/a)|^2 r'dr'd\phi'}$$

(4.2.4 − 5)

$$A_{s11} = \frac{\left\{ \iint_S [A_{01} J_0(U_{0s}r/a) J_1(U_{1f}r'/a) \cos \phi' + A_{s11} J_1(U_{1s}r/a) J_1(U_{1f}r'/a) \cos \phi \cos \phi'] r' dr' d\phi' \right\}}{\int_S |J_1(U_{1f}r'/a) \cos \phi'|^2 r' dr' d\phi'} \qquad (4.2.4-6)$$

2. The sensing cladding - filtering core interface

$$A_{f01} = \frac{\left\{ \iint_S [B_{s01} K_0(W_{0s}r/a) J_0(U_{0f}r'/a) + B_{s11} J_1(W_{1s}r/a) J_0(U_{0f}r'/a) \cos \phi'] r' dr' d\phi' \right\}}{\int_S |J_0(U_{0f}r'/a)|^2 r' dr' d\phi'} \qquad (4.2.4-7)$$

$$A_{f11} = \frac{\left\{ \iint_S [B_{s01} K_0(W_{0s}r/a) J_1(U_{1f}r'/a) \cos \phi' + B_{s11} K_1(W_{1s}r/a) J_1(U_{1f}r'/a) \cos \phi \cos \phi'] r' dr' d\phi' \right\}}{\int_S |J_1(U_{1f}r'/a) \cos \phi'|^2 r' dr' d\phi'} \qquad (4.2.4-8)$$

3. The sensing cladding - filtering cladding interface

$$B_{f01} = \frac{\left\{ \iint_S [B_{s01} K_0(W_{0s}r/a) K_0(W_{0f}r'/a) + B_{s11} K_1(W_{1s}r/a) K_0(W_{0f}r'/a) \cos \phi] r' dr' d\phi' \right\}}{\int_S |K_0(W_{0f}r'/a)|^2 r' dr' d\phi'} \qquad (4.2.4-9)$$

$$B_{f11} = \frac{\left\{ \iint_S [B_{s01} K_0'(W_{0s} r/a) K_1(W_{1f} r'/a) \cos\phi' + B_{s11} K_1(W_{1s} r/a) K_1(W'_{1f} r') \cos\phi \cos\phi'] r' dr' d\phi' \right\}}{\int_S |K_1(W'_{1f} r'/a) \cos\phi'|^2 r' dr' d\phi'} \qquad (4.2.4-10)$$

From these three regions, only the sensing core - filtering core interface and the sensing cladding - filtering core interface contribute to the filtering core's fields.

In order to solve this problem the unprimed functions need to be converted to primed coordinates. A method of converting the unprimed coordinates to the primed coordinates is to apply the Summation Theorem for Bessel functions [18]. The summation theorem is the following

$$e^{jv\psi} Z_v(mr) = \sum_{k=-\infty}^{\infty} J_k(md) Z_{v+k}(mr') e^{jk(\pi - \phi')} \qquad (4.2.4-11)$$

where,

$$Z_v = J_v, Y_v, H_v^{(1)}, \text{ or } H_v^{(2)}$$

where,

J, is a Bessel Function of the first kind.

Y, is a Bessel Function of the second kind.

$H_\nu^{(1)}$ is a Hankel Function of the first kind.

$H_\nu^{(2)}$ is a Hankel Function of the second kind.

I_ν is a modified Bessel Function of the first kind.

K_ν is a modified Bessel Function of the second kind.

m is arbitrary.

The relationship between the primed and the unprimed cooordinates is shown in Figure 15. d is the distance that the sensing fiber's core is offset from the filtering fiber. The angles relate to one another from simple geometry.

$$\psi + \phi = \phi' \qquad (4.2.4 - 12)$$

$$\psi = \phi' - \phi \qquad (4.2.4 - 13)$$

Equation 4.2 4-11 can be rewritten in terms of primed and unprimed coordinates.

$$e^{j\nu(\phi'-\phi)} = \sum_{k=-\infty}^{\infty} J_k(\eta d) Z_{\nu+k}(\eta r') e^{jk(\pi - \phi)} \qquad (4.2.4 - 14)$$

To convert $J_0(U_0 r/a)$ into the primed coordinate system via Equation 4.2 4-14, the following relationships are true.

$$\nu = 0$$

$$Z_\nu = J_0$$
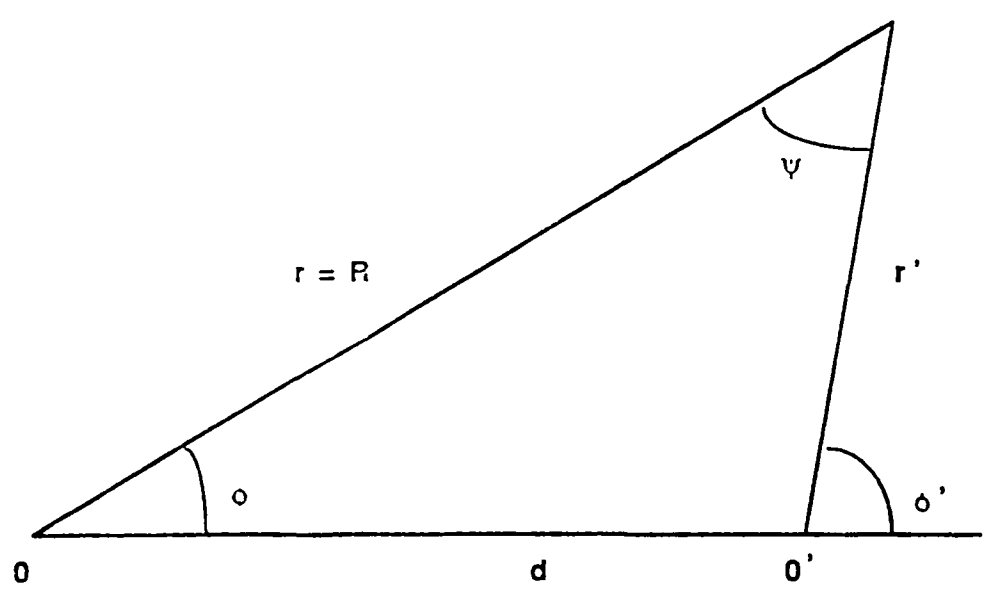
Figure 15. Relationship Between Unprimed and Primed Coordinates

$$m = U_0/a$$

In order to write Equation 4 2 4-14 in a more compact form, the following recurrence relationship will be envoked.

$$J_{(-k)} = (-1)^k J_k \qquad (4\ 2.4-15)$$

Now, $J_0(U_c r/a)$ can be written in terms of the primed coordinates.

$$J_0(U_c r/a) = \frac{J_0(U_0 d/a) J_0(U_0 r'/a) +}{2 \sum_{k=1}^{\infty} (-1)^k J_k(U_0 d/a) J_k(U_0 r'/a) \cos(k\phi')} \qquad (4\ 2\ 4-16)$$

To convert $J_1(U_1 r/a) \cos \phi$ into primed coordinates can be rewritten as Equation 4 2-4-17.

$$J_1(U_1 r/a) \cos \phi = Re\left[e^{-j\phi} J_1(U_1 r/a)\right] \qquad (4.2\ 4-17)$$

$J_1(U_1 r/a) \cos \phi$ in terms of the primed coordinates can be expressed as Equation 4 2-4-18

$$J_1(U_1 r/a) \cos \phi = \left\{ \frac{J_0(U_1 d/a) J_1(U_1 r'/a) \cos \phi' +}{\sum_{k=1}^{\infty} J_k(U_1 d/a)(-1)^k [J_{k+1}(U_1 r'/a) \cos[(k+1)\phi']} \right. \qquad (4.2.4-18)$$
$$\left. - J_{k-1}(U_1 r'/a) \cos[(k-1)\phi']]\right\}$$

$K_0(W_0 r/a)$ needs to be expressed in terms of the primed coordinates. It is important to note the following relationships.

$$H_v^{(1)}(jx) = \left(\frac{2}{\pi}\right) j^{-(v+1)} K_v(x) \tag{4.2.4-19}$$

$$J_v(jx) = j^v I_n(x)$$

So Equation 4 2.4-14 can be rewritten in terms of the Hankel of the first kind.

$$H_0^{(1)}(\overline{W}_0 r/a) = 2 \sum_{k=1}^{\infty} \frac{J_0(\overline{W}_0 d/a) H_0^{(1)}(\overline{W}_0 r'/a) +}{(-1)^k J_k(\overline{W}_0 d/a) H_k^{(1)}(\overline{W}_0 r'/a) \cos(k\phi')} \tag{4.2.4-20}$$

where

$$\overline{W}_0 = j W_0$$

By applying the relationships of Equation 4.2.4-19 to Equation 4.2.4-20, $K_0(W_0 r/a)$ can be written in terms of the primed coordinates.

$$K_0(W_0 r/a) = 2 \sum_{k=1}^{\infty} \frac{I_0(W_0 d/a) K_0(W_0 r'/a) +}{(-1)^k I_k(W_0 d/a) K_k(W_0 r'/a) \cos(k\phi')} \tag{4.2.4-21}$$

Finally, $K_1(W_1 r/a) \cos\phi$ needs to be expressed in terms of the primed coordinates.

$$K_1(W_1 r/a) \cos\phi = \left\{ \sum_{k=1}^{\infty} \frac{I_0(W_1 d/a) K_1(W_1 r'/a) \cos\phi' +}{I_k(W_1 d/a)[K_{k+1}(W_1 r'/a) \cos[(k+1)\phi'] +} \atop K_{k-1}(W_1 r'/a) \cos[(k-1)\phi']] \right\} \tag{4.2.4-22}$$

Now all of the unprimed coordinates are expressed in terms of the primed coordinates. The integrations discussed earlier can be performed. However, it is important to point

out that this integration is still difficult to perform. The geometry of this problem as shown in Figure 14 does not lend itself to a readily doable integration in polar coordinates. The symmetry is lost. This problem could be modified, so the splice loss due to a lateral offset could be evaluated. Instead of offsetting the two identical fibers, the filtering fiber could be a fiber that has a core diamenter half of the sensing fiber's core, as shown in Figure 16. This filtering fiber's core would sit in the core of the sensing fiber. This configuration would still pick-up one lobe of the LP_{01} and LP_{11} modal pattern. However, the filtering fiber will only support the LP_{01} mode because due to the decrease in the filtering fiber's core size, the $V-number$ will be halved. The integrations presented earlier will only deal with the LP_{0}. amplitude coefficient. Finally, it will be assumed that the power contribution to the filtering fiber s core will be due to the sensing fiber's core

Note. The filtering fiber s core inset in the sensing fiber's core will be considered an approximation for the case where two identical fibers are laterally offset.

The modified integration can be written as Equation 4.2.4-23.

$$
A_{\rho 01} = \frac{\left\{\int_S A_{s01}J_0(U_{0\prime}r'2/a)[J_0(U_{0s}d/a)J_0(U_{0s}r'/a) + 2\sum_{k=1}^{\infty}(-1)^k J_k(U_{0s}d/a)J_k(U_{0s}r'/a)\cos(k\phi')\right] + A_{s11}J_0(U_{0\prime}r'2/a)[J_0(U_{0s}d/a)J_1(U_{1s}r'/a)\cos\phi' + \sum_{k=1}^{\infty}J_k(U_{1s}d/a)(-1)^k[J_{k+1}(U_{1s}r'/a)\cos[(k+1)\phi'] \atop J_{k-1}(U_{1s}r'/a)\cos[(k-1)\phi']]\right\}}{\int_S |J_0(U_{0\prime}r'2/a)|^2 r'dr'd\phi'}
$$

(4 2.4 – 23)
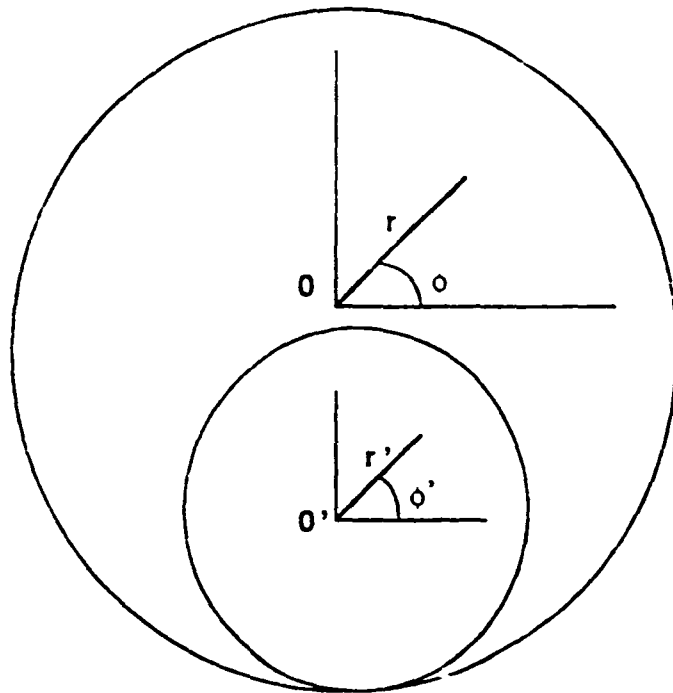
Figure 16. Cross-Section of the Asymmetrical Splice: The Filtering Fiber Is Half The Core Diameter of the Sensing Fiber

This equation can be simplified because the limits of integration for ϕ' are 0 to 2π. Any $\cos(n\phi)$ integrated from 0 to 2π, where n is an integer, is zero

$$A_{f01} = \frac{\int_0^{2\pi}\int_0^{a/2} A_{s01}J_0(U_{0f}r'2/a)J_0(U_{0s}d/a)J_0(U_{0s}r'/a)r'dr'd\phi'}{\int_0^{2\pi}\int_0^{a/2}|J_0(U_{0f}r'2/a)|^2r'dr'd\phi'} \qquad (4\,2.4-24)$$

This can be further simplified to Equation 4.2.4-25.

$$A_{f01} = \frac{A_{s01}J_0(U_{0s}d/a)\int_0^{a/2} J_0(U_{0f}r'2/a)J_0(U_{0s}r'/a)r'dr'}{\int_0^{a/2}|J_0(U_{0f}r'2/a)|^2r'dr'} \qquad (4.2\,4-25)$$

The integration in Equation 4.2.4-2. can be carried out after knowing the dimensions of the filtering and sensing fibers. This will be done in Section 4.2.5, Implementation of the Asymmetrical Splice. After the integration is performed, Equation 4.2.4-25 will take the form of Equation 4 2.4-26,

$$A_{f01} = A_{s01}X \qquad (4\,2.4-26)$$

where X is a number.

The field propagating in the filtering core is defined by Equation 4.2.4-27.

$$\vec{E} = A_{s01}XJ_0(U_0r'2/a)e^{-j\beta_{01}z}\hat{a}_x \qquad (4.2.4-27)$$

The efficiency of this splice can be expressed in terms of the intensities of the modes propagating in the sensing fiber, and the intensity of the LP_{01} mode propagating in the filtering fiber. The intensity of the field propagating in the filtering core is

$$I_{f01} = \frac{Y_1}{2} |\vec{E} \cdot \vec{E}^*| = \frac{Y_1}{2} A_{f01}{}^2 X^2 J_0{}^2 (U_{0f} r'2/a). \qquad (4.2.4-28)$$

The intensity of the LP_{01} mode in the sensing fiber is

$$I_{s01} = \frac{Y_1}{2} A_{s01}{}^2 J_0{}^2 (U_{0s} r/a). \qquad (4\,2\,4-29)$$

The intensity of the LP_{11} mode in the sensing fiber is

$$I_s = \frac{Y_1}{2} A_{s11}{}^2 J_1{}^2 (U_{1s} r/a) \cos{}^2 \phi. \qquad (4.2.4-30)$$

In determining the efficiency of the splice, Equation 4 2 4-34, the intensity functions, I_{f01}, I_{s01}, and I_{s11} need to be integrated over their respective fiber core areas. The filtering fiber's intensity function, I_{f01}, is integrated over the primed coordinates as indicated in Equation 4.2.4-31. The sensing fiber's intensity functions, I_{s01} and I_{s11}, are integrated over the unprimed coordinates as indicated in Equations 4.2.4-32 and 4.2 4-33.

$$I_{f01,\,t} = \int_0^{2\pi} \int_0^{a/2} \frac{Y_1}{2} X^2 A_{s01}{}^2 J_0{}^2 (U_{0f} r'2/a) r' dr' d\phi' \qquad (4.2.4-31)$$

$$I_{s01,\,t} = \int_0^{2\pi} \int_0^{a} \frac{Y_1}{2} A_{s01}{}^2 J_0{}^2 (U_{0s} r/a) r dr d\phi \qquad (4\,2.4-32)$$

$$I_{s11\ l} = \int_0^{2\pi} \int_0^a \frac{Y_1}{2} A_{s11}{}^2 J_1{}^2 (U_{1s}r/a) \cos{}^2\phi\, r\, dr\, d\phi \qquad (4.2.4-33)$$

The efficiency of this splice, η, is described in Equation 4 2.4-31.

$$\eta = \frac{A_{s01}\eta_{01} \dotplus A_{s11}\eta_{11}}{A_{s01} + A_{s11}} \qquad (4.2.4-31)$$

where $\eta_{01} = \dfrac{I_{r_1}}{I_{s01,\ l}}$, coupling efficiency of the LP_{01} mode in the sensing fiber to the LP_{01} in the filtering fiber, $\eta_{11} = \dfrac{I_{r_{11},l}}{I_{s11,l}}$, coupling efficiency of the LP_{11} mode in the sensing fiber the LP_{01} in the filtering fiber, and A_{s01} and A_{s11} are weighting factors. As seen in Equation 4 2.4-25, the only mode which contributes to the filtering fiber is the LP_{01} mode Equation 4 2.4-26 can be rewritten as

$$A_{f01} = A_{s01}X_{01} \dotplus A_{s11}X_{11} \qquad (4.2.4-35)$$

where

$$X_{11} = 0.$$

The coupling efficiency of the LP_{11} mode in the sensing fiber to LP_{01} mode in the filtering fiber, η_{11}, is zero. Equation 4.2.4-34 simplifies to

$$\eta = \frac{A_{s01}\eta_{01}}{A_{s01} + A_{s11}}. \qquad (4.2.4-36)$$

This splice loss calculation can be used to approximate the case where two identical fibers are laterally offset, as well as the case where the filtering fiber's core sits inside of

the sensing fiber's core   10 log of the efficiency, Equation 4 2.4-36, will yield the splice loss. However, the splice loss can not be explicitly evaluated because A_{o1} and A_{n1} are unknown.

4.2.5 Implementation of the Laterally Offset Splice

This section will examine a system which uses a few-moded laterally offset splice for in-line signal processing with a modal domain sensing system. This splice could be fabricated with two identical fibers laterally offset, but the simplified version of this splice will be considered in this section. The splice will consist of a filtering fiber which is half the core diameter of the sensing fiber. Thus, the main interest will be the core-core transfer of power.

Parameters of the sensing fiber are·

$a = 4.5 \mu m$

$NA = 0.1$

$n_1 = 1.458$

$n_2 = 1.4543$

$\lambda_{operating} \approx 780 nm$

$V = 3.6249$

$$U'_{0u} = 1.9571182$$

$$U_{1u} = 3.0220145$$

$$\lambda_{single\ mode\ operation} = 1300nm$$

Parameters of the filtering fiber are:

$$a = 2\mu m$$

$$NA = 0.1$$

$$n_1 = 1\ 458$$

$$n_2 = 1\ 4543$$

$$\lambda_{of\ operation} = 780nm$$

$$V = 1.611073$$

$$U_{\gamma} = 1.57061$$

$$\lambda_{single\ mode\ operation} = 633nm$$

The filtering fiber could have been singlemode at $780nm$, but the core diameter is $5\mu m$. That is more than half of the sensing fiber's radius. This optical fiber will filter more than one lobe of the speckle pattern. So it seems more feasible to use an optical fiber which is slightly less than half of the sensing fiber's diameter. This filtering fiber has a diameter of $4\mu m$.

Equation 4.2.4-25 can be rewritten with the parameters of the optical fiber.

$$A_{f01} = \frac{A_{s01}J_0(U'_{0s}d/a_s)\int_0^{2\mu m} J_0(U_{0f}r'/a_f)J_0(U_{0s}r'/a_s)r'dr'}{\int_0^{2\mu m} |J_0(U'_{0f}r'/a_f)|^2 r'dr'} \qquad (4.2.5-1)$$

where

$d = 2.0\mu m \; to \; 2.5\mu m,$

$a_f = 2\mu m,$

$a_s = 4.5\mu m,$

$U'_{0s} = 1.9571182, \; and$

$U'_{0f} = 1.57061.$

After integrating Equation 4.2 5-1, A_{f01} can be expressed as Equation 4.2.5-2,

$$A_{f01} = A_{s01}X, \qquad (4.2\;5-2)$$

where X is calculated from the program, Amp Fortran, which is found in the Appendix A. Then η_{t1}, Equation 4 2.5-3, can be calculated after integrating I_{f01} and I_{s01} These calculations are performed by using the fortran program, Int Fortran which is found in Appendix B.

$$\eta_{01} = \frac{I_{f01,i}}{I_{s01,i}} = \frac{\int_0^{2\pi}\int_0^{a_f} \frac{Y_1}{2} A_{f01}{}^2 X^2 J_0{}^2(U_{0f}r'/a_f)r'dr'd\phi'}{\int_0^{2\pi}\int_0^{a_s} \frac{Y_1}{2} A_{01}{}^2 J_0{}^2(U_{0s}r/a_s)rdrd\phi} \qquad (4.2.5-3)$$

Finally, the efficiency of the splice can be determined from Equation 4.2.4-36. The assumption which was made in Chapter 3, that $A_{s11} = 2A_{s01}$, will be used to crudely examine the splice efficiency Equation 4.2 4-36 can be rewritten as Equation 4.2.5-4.

$$\eta = \frac{\eta_{01}}{3} \qquad (4.2.5-4)$$

The following values for X, η_{01}, and L, the splice loss, were calculated for various lateral offsets, d:

$d = 2.50\mu m$: $X = 0.8847932$, $\eta_{01} = 0.2118394$, $L = 11.51\,dB$

$d = 2.25\mu m$: $X = 0.944511$, $\eta_{01} = 0.2413998$, $L = 10.94\,dB$

$d = 2.00\mu m$: $X = 0.9994462$, $\eta_{01} = 0.2676080$, $L = 10.496\,dB$.

The filtering fiber will detect more of the sensing fiber's LP_{01} mode, as the filtering fiber is brought closer to the center of the sensing fiber (d goes to $2\mu m$). This is due to the fact that LP_{01} mode is a Gaussian beam. The optimum placement of the filtering fiber for power considerations is a lateral offset of $d = 2.0\mu m$. Now, the propagating field in the filtering fiber s core for $d = 2\mu m$ can be written as Equation 4.2.5-3.

$$\vec{E} = A_{s01}(0.9994462)J_0(U_{0f}r'/a_f)\hat{a}_x \qquad (4\,2.5-5)$$

In order to perform the splice calculation exactly, the amplitude coefficients in Equation 4.2.5 need to be determined. This splice will enable in-line signal processing of the perturbations applied to the sensing fiber.

4.3 The Air-Gap Splice

A third micro-optical fiber device that is presented is the air-gap splice as shown in Figure 17 [3]. Unlike the last two devices, the modal conversion coupler and the asymmetrical splice, the air-gap splice is not used in conjunction with modal domain sensing. The air-gap splice is used with an OTDR system to monitor localized strain effects, Figure 18 [3] The fiber which is used with the air-gap splice has a $100\mu m$ core diameter and $140\mu m$ cladding diameter; this fiber has a step-index profile.

There is a Fresnel reflection at each of this air-gap splices, a pulse (4%reflected power) can be seen on the OTDR due to the air-gap splice. Due to the change in the medium at the air-gap splice (from glass to air), some of the higher order modes will be lost as light propagates in the air regime. The light will diverge, and the modes which travel closest to the core-cladding interface, the higher order modes will be lost as cladding modes.
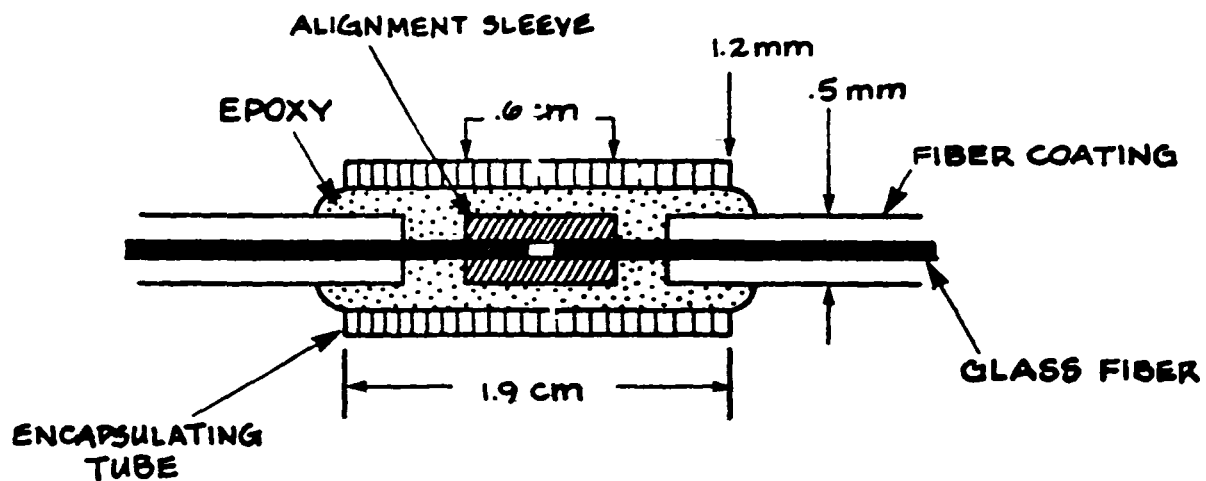
Figure 17. The Air-Gap Splice [3]

EXPERIMENTS

System Description
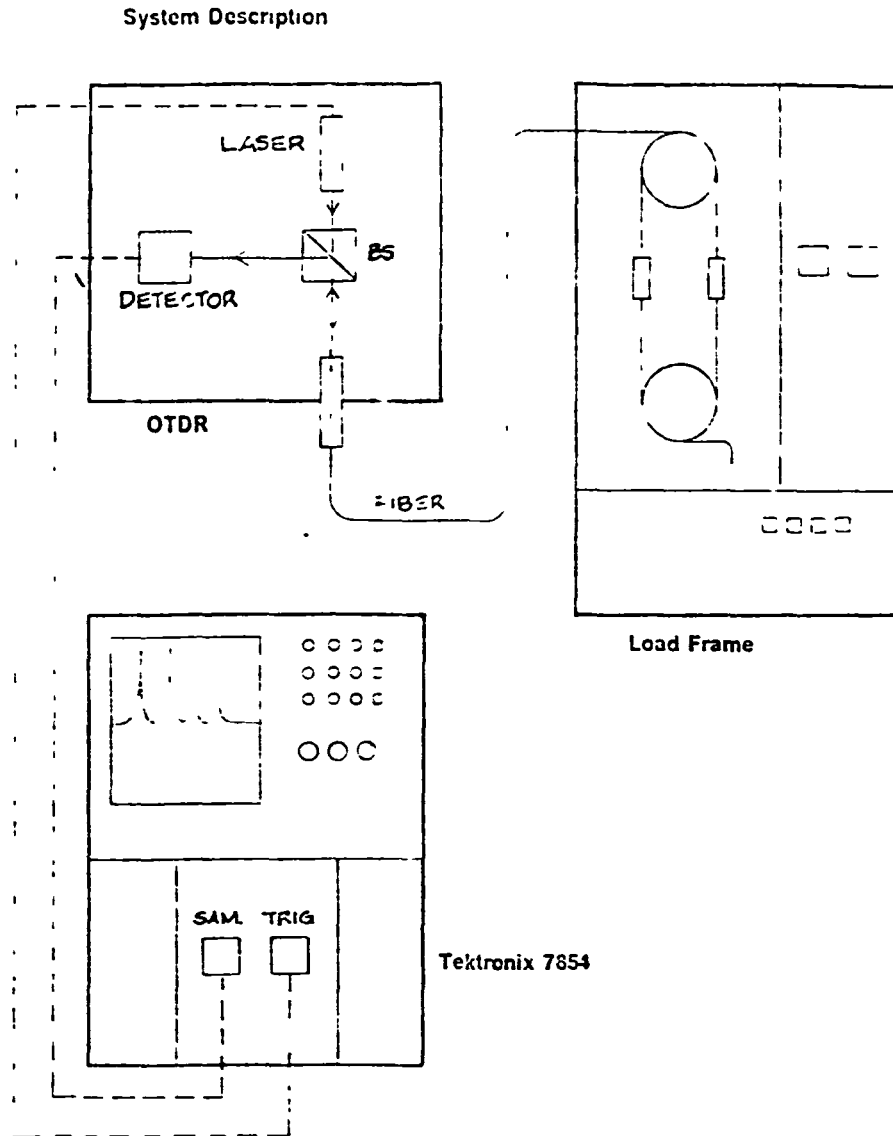
Figure 18. OTDR Set-Up With Air-Gap Splices to Detect Localized Strain [3]

The air-gap splice will magnify modal effects such as the modal content of the optical fiber and modal dispersion. Modal effects due to modal dispersion are shown in Figure 19 [3]. Modal dispersion can be expressed as Equation 4.3-1 [5]

$$T_{mod} = T_{max} - T_{min} = \frac{n_1 \Delta L}{c} \qquad (4.3-1)$$

where

T_{mod} = modal dispersion in time ,

T_{max} = path of the highest order mode,

T_{min} = path of the lowest order mode,

n_1 = index of refraction, core,

$\Delta = \frac{n_1{}^2 - n_2{}^2}{2n_1{}^2}$,

L = length of the fiber, and

$c = 3 \times 10^8 \, m/s.$

T_{mod} is dependent upon the launching conditions, as shown in Figure 19 [3]. If mainly lower order modes are launched as in a of Figure 19, the pulse is not as very board. If higher order modes are launched into the optical fiber as in b of Figure 19, the pulse tends to be more boarden than the case where mainly lower order modes are launched into the optical fiber. This is true due to the later arrival times of the higher order modes.
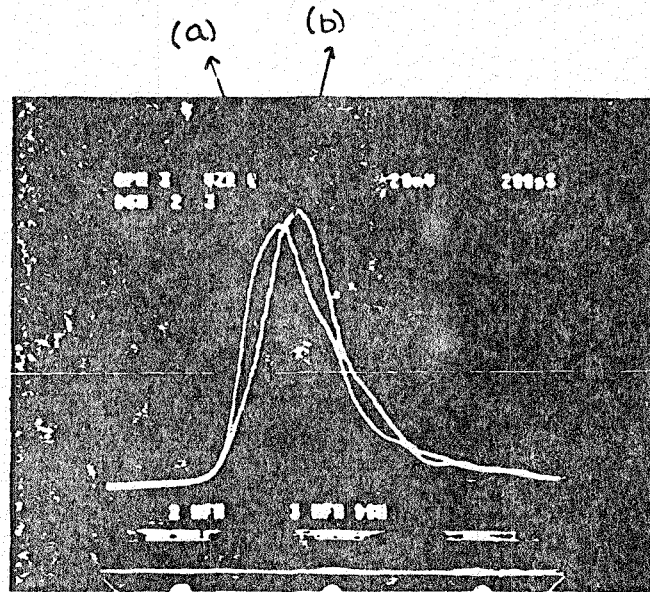
Figure 19. Modal Dispersion Due to Launching Conditions [3]: a) Lower Order Modes b) Higher Order Modes

As the fiber is strained, the pulses become boardened and elongated as in Figure 20 [3]. This is due to modal dispersion As the modes travel down the fiber as the fiber is elongated (strained), the pulses will boarden. This effect is demonstrated in Equation 4 3-2

$$T_{mod} = \frac{n_1 \Delta[L + \Delta L]}{c} \qquad (4.3 - 2)$$

where,

$\Delta L = $ *change in length of the optical fiber due to an applied axial strain*

The same effect can be seen with a fiber which has several air-gap splices. The further away from the beginning of the fiber each air-gap splice is located, the more boardened the pulse becomes. This boardening is due to modal dispersion. This is related to L in the numerator of Equation 4 3-1. The longer the light propagates the more dispersed it becomes.
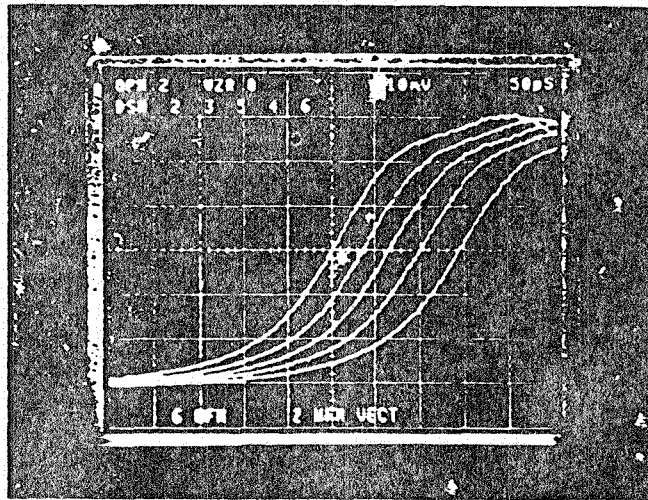
Figure 20. Modal Dispersion Due To Applied Strain [3]

4.0 Principles of Operation of Micro-Optical Fiber Devices

5.0 Future Work and Applications

These three micro-optical fiber devices, the modal conversion coupler, the asymmetrical splice and the air-gap splice, can help further research in fiber optic sensing and communications.

In conjunction with modal domain sensing, the modal conversion coupler is a method of generating new modes from a given set of input conditions. The modal conversion coupler needs to be mathematically described. The mechanisms behind the modal conversions in the taper regions and the coupler region needs to be modeled. Once a model is established for the modal conversion coupler, a repeatable method for fabricating these couplers needs to be established. This method must be consistent to generate the same output modes from a given set of input modes.

An application of this device is that a modal conversion coupler could generate the LP_{11} mode. The LP_{11} mode amplitude could be measured from the output of the modal conversion coupler. This field could be superimposed with a known LP_{01} field. With the correct modal amplitudes these two superimposed modes could generate the two-lobed

speckle pattern used for modal domain sensing. This would solve the present problem of unknown modal amplitudes due to variable launching conditions.

Another application of this device is a multiplexer in a communications system. This device would use the method of modal multiplexing. Certain modal combinations could carry a "channel of data" The coupler could be used for generating the modal combination to be multiplexed onto a fiber. All of these modal channels would need to be superimposed onto the data carrying optical fiber. An analogous device would need to be fabricated to demultiplex the modal channels. This modal conversion coupler could increase the information carrying capacity of a multimode optical fiber.

Also, in conjunction with modal domain sensing, the asymmetrical splice is a means of performing in-line signal processing In order for this splice to be completely effective, a function correlating the intensity changes in the filtering fiber due to applied perturbations to the sensing fiber need to be derived. This function will be nonlinear, since the intensity is a point function, which is a linear function. This asymmetrical splice will allow for a compact and packageable modal domain sensing system. This splice will be in the near field as opposed to the far field, so more power can be coupled into this splice as opposed to fiber placed in the far field. In terms of the loss calculations associated with the asymmetrical splice, the modal amplitudes for the sensing fields in the core need to be determined, so this calculation can be complete As mentioned earlier, to solve the problem of unknown modal amplitudes, the modal conversion coupler could be applied for a completely characterizable modal domain sensing system. Once the modal amplitudes are known, the theoretical results can be compared to an experimental asymmetrical splice with the filtering fiber's core inside the sensing fiber's core as in Figure 16. Then, the theoretical approximation of the filtering

fiber's core inside the sensing fiber's core can then be compared to the experimental asymmetrical splice with two identical fibers laterally offset as in Figure 15.

Finally, the air-gap splice exhibits modal effects evident in multimode optical fibers. For applications where modal dispersion effects are undesireable, the air-gap splice could be fabricated with single mode optical fibers. However, the air-gap splice could be used to monitor modal dispersion effects as a fiber is strained, or monitor disperson along the length of the optical fiber. The air-gap splice could be used to analyze the modal content which is launched into the optical fiber. This could be a method of determining whether lower, higher, or evenly distributed modes are propagating in the optical fiber.

6.0 Conclusions

Three micro-optical fiber devices, a modal conversion coupler, an asymmetrical splice, and an air-gap splice, were presented. Two of these devices can be used in conjunction with modal domain sensing, the modal conversion coupler and the asymmetrical splice.

The modal conversion conversion coupler can be a method of describing launching conditions. Modal amplitudes in conjunction with modal domain sensing are unknown at this time. The modal conversion coupler can generate a mode from a given set of input conditions. The modal amplitude from the output of the coupler can be determined, and then superimposed with other known modal amplitudes. This is a possible solution to unknown launching conditions.

The asymmetrical splice is a method of performing in-line signal processing. The asymmetrical splice allows a modal domain sensing system to be a compact and packageable system. Intensity changes in the filtering fiber can be correlated to perturbations in the sensing fiber. Finally, splice loss calculations for laterally offset multimode and single mode fibers is not applicable to few-moded fibers. A new method

for evaluating splice loss for few-moded fibers has been developed In order to determine the splice loss explicitly, amplitude coefficients for the modes propagating in the filtering fiber need to be determined from the modes propagating in the sensing fiber.

The air-gap splices exhibit modal effects when used with multimode fibers. The air-gap splice is a method of viewing modal dispersion, whether modal dispersion is dependent upon the modal content launched into the optical fiber or is due to length elongation due to axial strain applied to the optical fiber

Appendix A: Amp Fortran Listing

```
CCCCCCCCCCCCCCCCCCCCCCCCCCCCCCCCCCCCCCCCCCCCCCCCCCCCCCCCCCCCCCCCCCCCC
C                                                                   C
C                        AMP FORTRAN                                C
C                                                                   C
C                                                                   C
C                                                                   C
C                     WRITTEN BY AMY FLAX                           C
C                                                                   C
CCCCCCCCCCCCCCCCCCCCCCCCCCCCCCCCCCCCCCCCCCCCCCCCCCCCCCCCCCCCCCCCCCCCC


CCCCCCCCCCCCCCCCCCCCCCCCCCCCCCCCCCCCCCCCCCCCCCCCCCCCCCCCCCCCCCCCCCCCC
C                                                                   C
C  THIS PROGRAM IS DESIGNED TO AID IN CALCULATING AF01 IN           C
C                                                                   C
C  EQUATION  4 2.5-1, WHERE AF01 = AS01 X.   THIS PROGRAM CALCULATES C
C                                                                   C
C  X.  THE MAIN PROGRAM USES AN IMSL ROUTINE, DCADRE, TO DO THE     C
C                                                                   C
C  INTEGRATIONS.  DCADRE USES THE FOLLOWING PARAMETERS:             C
C                                                                   C
C       F=FUNCTION TO BE INTEGRATED, WHICH IS CALLED EXTERNALLY     C
C       A=LOWER LIMIT OF INTEGRATION                                C
C       B=UPPER LIMIT OF INTEGRATION                                C
C       AERR=INPUT ERROR                                            C
C       RERR=RETURN ERROR                                           C
C       ERROR=ERROR MESSAGES                                        C
C       C=INTEGRATED ANSWER                                         C
C                                                                   C
CCCCCCCCCCCCCCCCCCCCCCCCCCCCCCCCCCCCCCCCCCCCCCCCCCCCCCCCCCCCCCCCCCCCC

CCCCCCCCCCCCCCCCCCCCCCCCCCCCCCCCCCCCCCCCCCCCCCCCCCCCCCCCCCCCCCCCCCCCC
C                                                                   C
C  DCADRE IS USED TWICE.                                            C
C                                                                   C
C       1) TO INTEGRATE THE NUMERATOR OF EQUATION 4.2.5-1.          C
C          THE EXTERNAL FUNCTION TO BE INTEGRATED IS 'F'.           C
C          THE RESULT IS 'C'.                                       C
C                                                                   C
C       2) TO INTEGRATE THE DENOMINATOR OF EQUATION 4.2.5-1.        C
C          THE EXTERNAL FUNCTION TO BE INTEGRATED IS 'FX'.          C
C          THE RESULT IS 'D'.                                       C
C                                                                   C
CCCCCCCCCCCCCCCCCCCCCCCCCCCCCCCCCCCCCCCCCCCCCCCCCCCCCCCCCCCCCCCCCCCCC



      INTEGER IER
      REAL  DCADRE,F,A,B, AERR, RERR, ERROR,C,D,FX,J,DI,UF,AF
      EXTERNAL F,FX
      A=0.0
      B=2.0
```

```
      RERR=0.
      AERR= 1.0E-5

CCCCCCCCCCCCCCCCCCCCCCCCCCCCCCCCCCCCCCCCCCCCCCCCCCCCCCCCCCCCCCCC
C                                                                C
C   DCADRE IS CALLED TO INTEGRATE F AND FX, WHICH ARE FOUND IN    C
C                                                                C
C   SUBROUTINES AT THE BOTTOM OF THE PROGRAM.                     C
C                                                                C
CCCCCCCCCCCCCCCCCCCCCCCCCCCCCCCCCCCCCCCCCCCCCCCCCCCCCCCCCCCCCCCC


      C = DCADRE (F,A,B,AERR,RERR,ERROR,IER )
      D = DCADRE (FX,A,B,AERR,RERR,ERROR,IER)


CCCCCCCCCCCCCCCCCCCCCCCCCCCCCCCCCCCCCCCCCCCCCCCCCCCCCCCCCCCCCCCC
C                                                                C
C   THIS SECTION CALCULATES J0( UOS DI/AS) OF EQUATION 4.2.5-1.   C
C                                                                C
C   THIS TERM ACCOUNTS FOR THE LATERAL OFFSET OF THE FILTERING    C
C                                                                C
C   FIBER.                                                        C
C                                                                C
C        US = UOS/AS, FIBER PARAMETER CALCULATED                 C
C                                                                C
C        DI = DISTANCE CENTER OF FILTERING FIBER OFFSET FROM      C
C             CENTER OF SENSING FIBER                             C
C                                                                C
C        J = J0S (US DI ), BESSEL FUNCTION OF THE FIRST KIND      C
C            APPROXIMATED BY A POLYNOMIAL. THE APPROXIMATION      C
C            OF THIS FUNCTION IS FOUND IN REFERENCE    .          C
C                                                                C
CCCCCCCCCCCCCCCCCCCCCCCCCCCCCCCCCCCCCCCCCCCCCCCCCCCCCCCCCCCCCCCC



      DI=2.00
      US=0.434915159

      J=(1- 2.2499997* ((US*DI/3.0)**2 ) + 1.2656208*((US*DI/3.0)**4)
      C - 0.3163866*((US*DI/3 0)**6) + 0.0444479*((US*DI/3.0)**8) -
      C0.0039444*((US*DI/3.0)**10) - 0.0002100*((US*DI/3.0)**12))


CCCCCCCCCCCCCCCCCCCCCCCCCCCCCCCCCCCCCCCCCCCCCCCCCCCCCCCCCCCCCCCC
C                                                                C
C   X OF EQUATION 4.2.5-1 IS CALCULATED, WHERE AF = X.            C
C                                                                C
C   X IS PRINTED OUT ON THE TERMINAL SCREEN.                     C
C                                                                C
CCCCCCCCCCCCCCCCCCCCCCCCCCCCCCCCCCCCCCCCCCCCCCCCCCCCCCCCCCCCCCCC
```

```fortran
      AF=J*C/D

      WRITE (*,*) AF
      STOP
      END
```

```
CCCCCCCCCCCCCCCCCCCCCCCCCCCCCCCCCCCCCCCCCCCCCCCCCCCCCCCCCCCCCCCCCCCC
C                                                                  C
C    THIS IS A SUB ROUTINE TO CALCULATE THE FUNCTION IN THE        C
C                                                                  C
C    NUMERATOR OF EQUATION 4.2-5,(JO (UOS X / AS )) (JO (UOF X /AF)).C
C                                                                  C
C          1) US = UOS/AS                                          C
C          2) UF = UOF/AF                                          C
C          3) THE BESSELS FUNCTION ARE APPROXIMATED BY A POLYNOMIAL C
C          4) S = JO (US X)                                        C
C          5) FF= JO (UF X)                                        C
C          6) F=S*FF*X, WHICH IS THE FUNCTION TO BE INTEGRATED     C
C                                                                  C
CCCCCCCCCCCCCCCCCCCCCCCCCCCCCCCCCCCCCCCCCCCCCCCCCCCCCCCCCCCCCCCCCCCC
```

```fortran
      REAL FUNCTION F(X)
      REAL X,UF,US,S,FF
      UF=0.7853052
      US=0.434915159
      FF=(1- 2 2499997* ((UF*X/3.0)**2 ) + 1.2656208*((UF*X/3.0)**4)
     C - 0.3163866*((UF*X/3.0)**6) + 0.0444479*((UF*X/3.0)**8) -
     C0.0039444*((UF*X/3.0)**10) - 0.0002100*((UF*X/3.0)**12))

      S=(1- 2.2499997* ((US*X/3 0)**2 ) + 1.2656208*((US*X/3.0)**4)
     C-0.3163866*((US*X/3.0)**6) + 0.0444479*((US*X/3.0)**8) -
     C0.0039444*((US*X/3.0)**10) - 0.0002100*((US*X/3.0)**12))
      F=S*FF*X

      RETURN
      END
```

```
CCCCCCCCCCCCCCCCCCCCCCCCCCCCCCCCCCCCCCCCCCCCCCCCCCCCCCCCCCCCCCCCCCCC
C                                                                  C
C    THIS SUBROUTINE CALCULATES THE FUNCTION IN THE DENOMINATOR    C
C                                                                  C
C    IN EQUATION 4.2.5-1.  THE METHOD IS THE SAME AS IN THE OTHER  C
C                                                                  C
C    SUBROUTINE, EXCEPT THESE MODIFICATIONS:                       C
C                                                                  C
C          1) FF, UF ARE THE SAME AS IN THE OTHER SUBROUTINE       C
C          2) THE FUNCTION TO BE INTEGRATED IS FX                  C
C          3) FX = (ABS (FF))**2 X                                 C
C                                                                  C
CCCCCCCCCCCCCCCCCCCCCCCCCCCCCCCCCCCCCCCCCCCCCCCCCCCCCCCCCCCCCCCCCCCC
```

```
REAL FUNCTION FX(X)
REAL X,UF,FF
UF=0.7853052
FF=(1- 2.2499997* ((UF*X/3.0)**2 ) + 1.2656208*((UF*X/3.0)**4)
C - 0.3163866*((UF*X/3.0)**6) + 0.0444479*((UF*X/3.0)**8) -
C0.0039444*((UF*X/3.0)**10) - 0.0002100*((UF*X/3.0)**12))

FX= (( ABS (FF) )**2 )*X
RETURN
END
```

Appendix B: Int Fortran Listing

```
CCCCCCCCCCCCCCCCCCCCCCCCCCCCCCCCCCCCCCCCCCCCCCCCCCCCCCCCCCCCCCCCCC
C                                                                C
C                       INT FORTRAN                              C
C                                                                C
C                                                                C
C                                                                C
C                   WRITTEN BY AMY FLAX                          C
C                                                                C
CCCCCCCCCCCCCCCCCCCCCCCCCCCCCCCCCCCCCCCCCCCCCCCCCCCCCCCCCCCCCCCCCC


CCCCCCCCCCCCCCCCCCCCCCCCCCCCCCCCCCCCCCCCCCCCCCCCCCCCCCCCCCCCCCCCCC
C                                                                C
C  THIS PROGRAM IS DESIGNED TO AID IN CALCULATING NO1 IN         C
C                                                                C
C  EQUATION  4.2.4-31.  THIS PROGRAM CALCULATES                  C
C                                                                C
C  NO1. THE MAIN PROGRAM USES AN IMSL ROUTINE, DCADRE, TO DO THE C
C                                                                C
C  INTEGRATIONS   DCADRE USES THE FOLLOWING PARAMETERS:          C
C                                                                C
C      F=FUNCTION TO BE INTEGRATED, WHICH IS CALLED EXTERNALLY   C
C      A=LOWER LIMIT OF INTEGRATION                              C
C      B=UPPER LIMIT OF INTEGRATION                              C
C      AERR=INPUT ERROR                                          C
C      RERR=RETURN ERROR                                         C
C      ERROR=ERROR MESSAGES                                      C
C      C=INTEGRATED ANSWER                                       C
C                                                                C
CCCCCCCCCCCCCCCCCCCCCCCCCCCCCCCCCCCCCCCCCCCCCCCCCCCCCCCCCCCCCCCCCC

CCCCCCCCCCCCCCCCCCCCCCCCCCCCCCCCCCCCCCCCCCCCCCCCCCCCCCCCCCCCCCCCCC
C                                                                C
C  DCADRE IS USED TWICE.                                         C
C                                                                C
C      1) TO INTEGRATE THE NUMERATOR OF EQUATION 4.2.4-31.       C
C         THE EXTERNAL FUNCTION TO BE INTEGRATED IS 'F'.         C
C         THE RESULT IS 'C' WHICH IS INTEGRATED FROM 0 TO 2.     C
C                                                                C
C      2) TO INTEGRATE THE DENOMINATOR OF EQUATION 4.2.4-3.      C
C         THE EXTERNAL FUNCTION TO BE INTEGRATED IS 'FX'.        C
C         THE RESULT IS 'D' WHICH IS INTEGRATED FROM 0 TO 4.5.   C
C                                                                C
CCCCCCCCCCCCCCCCCCCCCCCCCCCCCCCCCCCCCCCCCCCCCCCCCCCCCCCCCCCCCCCCCC



        INTEGER IER
        REAL DCADRE,F,A,B, AERR, RERR, ERROR,C,D,FX,E,X1,A2,B2
        EXTERNAL F,FX
        A=0.0
        B=2.0
```

```
      RERR=0.
      AERR= 1.0E-5
      A2 =0.0
      B2= 4.5
CCCCCCCCCCCCCCCCCCCCCCCCCCCCCCCCCCCCCCCCCCCCCCCCCCCCCCCCCCCCCCCCCC
C                                                                C
C    DCADRE IS CALLED TO INTEGRATE F AND FX, WHICH ARE FOUND IN   C
C                                                                C
C    SUBROUTINES AT THE BOTTOM OF THE PROGRAM.                   C
C                                                                C
CCCCCCCCCCCCCCCCCCCCCCCCCCCCCCCCCCCCCCCCCCCCCCCCCCCCCCCCCCCCCCCCCC


      C = DCADRE (F,A,B,AERR,RERR,ERROR,IER )
      D = DCADRE (FX,A2,B2,AERR,RERR,ERROR,IER)


CCCCCCCCCCCCCCCCCCCCCCCCCCCCCCCCCCCCCCCCCCCCCCCCCCCCCCCCCCCCCCCCCC
C                                                                C
C  X=X1, CALCULATED FROM THE AMP FORTRAN PROGRAM IS ENTERED HERE. C
C                                                                C
CCCCCCCCCCCCCCCCCCCCCCCCCCCCCCCCCCCCCCCCCCCCCCCCCCCCCCCCCCCCCCCCCC
      X1 = 0.994462


CCCCCCCCCCCCCCCCCCCCCCCCCCCCCCCCCCCCCCCCCCCCCCCCCCCCCCCCCCCCCCCCCC
C                                                                C
C    NO1 OF EQUATION 4.2.4-31 IS CALCULATED, WHERE NO1 = IFO1/ISO1 C
C                                                                C
C    E = NO1                                                     C
C                                                                C
CCCCCCCCCCCCCCCCCCCCCCCCCCCCCCCCCCCCCCCCCCCCCCCCCCCCCCCCCCCCCCCCCC


      E=(X1 ** 2 ) * C /D

      WRITE (*,*) E
      STOP
      END
CCCCCCCCCCCCCCCCCCCCCCCCCCCCCCCCCCCCCCCCCCCCCCCCCCCCCCCCCCCCCCCCCC
C                                                                C
C   THIS IS A SUBROUTINE TO CALCULATE THE FUNCTION IN THE        C
C                                                                C
C   NUMERATOR OF EQUATION 4.2.4-31, J0 ( UOF X /AF).             C
C                                                                C
C   1) UF = UOF/AF                                              C
C   2) THE BESSELS FUNCTION ARE APPROXIMATED BY A POLYNOMIAL [19] C
C   3) FF= J0 (UF X)                                            C
C   4) F=((FF)**2)*X, WHICH IS THE FUNCTION TO BE INTEGRATED    C
C                                                                C
CCCCCCCCCCCCCCCCCCCCCCCCCCCCCCCCCCCCCCCCCCCCCCCCCCCCCCCCCCCCCCCCCC
```

```
      REAL FUNCTION F(X)
      REAL X,UF,FF
      UF=0.7853052
      FF=(1- 2.2499997* ((UF*X/3.0)**2 ) + 1.2656208*((UF*X/3.0)**4)
     C - 0.3163866*((UF*X/3.0)**6) + 0.0444479*((UF*X/3.0)**8) -
     C0 0039444*((UF*X/3.0)**10) + 0.0002100*((UF*X/3.0)**12))
      F= ((FF)**2 )*X

      RETURN
      END
```

```
CCCCCCCCCCCCCCCCCCCCCCCCCCCCCCCCCCCCCCCCCCCCCCCCCCCCCCCCCCCCCCCCCCC
C                                                                 C
C    THIS SUBROUTINE CALCULATES THE FUNCTION IN THE DENOMINATOR    C
C                                                                 C
C    IN EQUATION 4.2.4-31.  THE METHOD IS THE SAME AS IN THE OTHER C
C                                                                 C
C    SUBROUTINE, EXCEPT THESE MODIFICATIONS:                       C
C                                                                 C
C        1) S AND US, WHERE US = UOS/AS, REPLACE FF AND UF         C
C        2) THE FUNCTION TO BE INTEGRATED IS FX                    C
C        3) FX = (S)**2 * X                                        C
C                                                                 C
CCCCCCCCCCCCCCCCCCCCCCCCCCCCCCCCCCCCCCCCCCCCCCCCCCCCCCCCCCCCCCCCCCC
```

```
      REAL FUNCTION FX(X)
      REAL X,US,S
      US=0.434915159
      S=(1- 2.2499997* ((US*X/3.0)**2 ) + 1.2656208*((US*X/3.0)**4)
     C - 0.3163866*((US*X/3.0)**6) + 0.0444479*((US*X/3.0)**8) -
     C0.0039444*((US*X/3.0)**10) + 0.0002100*((US*X/3.0)**12))

      FX= ( (S)**2 )*X
      RETURN
      END
```

References

1. P.A. Ehrenfeuchter, "Modal Domain Sensing of Vibration in Beams," M.S. Thesis, Virginia Tech, December 1986.

2. N.K Shankaranarayanan, "Mode-Mode Interference in Optical Fibers: Analysis and Experiment," M.S. Thesis, Virginia Tech, April 1987.

3. B.D. Zimmermann, "High Resolution Optical Time Domain Reflectometry and Its Applications," M.S. Thesis, Virginia Tech, January 1988.

4. *Designers Guide to Fiber Optics*, AMP Inc, 1982.

5. G. Keiser, *Optical Fiber Communications*, McGraw-Hill, New York, 1983.

6. A. Yariv, *Optical Electronics*, Holt, Rinehart and Winston, New York, 1985.

7. M.R. Layton and J.A. Bucaro, "Optical Fiber Acoustic Sensor Utilizing Mode-Mode Interference," *Applied Optics*, vol 18, no. 5, p. 666, March 1979.

8. S.A. Kingsley and J.A. Bucaro, "Multimode Optical Fibre Phase Modulation and Discrimination I & II," *Electronics Letters*, vol. 14, no. 11, p.322/335, May 1978.

9. K D. Bennett, "Fiber Optic Methods for Remote Sensing," M.S. Thesis, Virginia Tech, August 1985.

10. K.T. Srinivas, "Axial Strain Effects on Optical Fiber Mode Patterns," M.S. Thesis, Virginia Tech, January 1987.

11. B.D. Duncan, "Modal Interference Techniques for Strain Detection in Few-Mode Optical Fibers," M.S. Thesis, Virginia Tech, April 1988.

12. G.B. Hocker, "Fiber Optic Sensing of Pressure and Temperature," *Applied Optics*, vol. 18, no. 9, p.1445, 1 May 1979.

13. C.D. Butter and G B. Hocker, "Fiber Optic Strain Gauge," *Applied Optics*, vol. 17, no. 18, p.2867, 15 September 1978

14. W.V. Sorin, B.Y. Kim and H.J. Shaw, "Highly Selective Evanescent Modal Filter for Two-Moded Optical Fibers," *Optics Letters*, vol.11, no. 9, p.581, September 1986.

15. N.S. Kapany and J.J. Burke, *Optical Waveguides*, Academic Press, New York, 1972.

16. C.M. Miller, *Optical Fiber Splices and Connectors· Theory and Methods*, Marcel Dekker Inc., New York, 1986.

17. A.W. Snyder and J.D. Love, *Optical Waveguide Theory*, Chapman and Hall, New York, 1983.

18. I.S. Gradshteyn and I.W. Ryzik, *Table of Integrals, Series and Products*, Academic Press, New York, 1965

19. M. Abramkositz and I. Stegum, ed., *Handbook of Mathematical Functions*, Dover Publications, Inc., New York, 1972.

Vita

Amy Flax was born on August 26, 1964 in Framingham, Massachusetts. She graduated from Virginia Tech in June. 1986 with a Bachelor of Science in Electrical Engineering. Amy decided to pursue graduate studies in electrical engineering at Virginia Tech, specializing in fiber optics. During her stay at Virginia Tech, she worked under Dr. R.O. Claus at the Fiber and Electro-Optics Research Center. Amy enjoys theatre, travelling, aerobics, and Bruce Springsteen. Amy is going to be a world traveller this summer as she crosses the Atlantic to explore older civilizations and the night life in Paris. Then, after many years of being a student Amy will be gainfully employed with AT&T in New Jersey.

Modal Interference Techniques for Strain Detection in Few-Mode Optical

Fibers

by
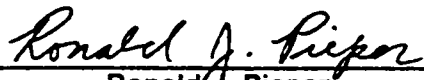
Bradley Dean Duncan

Thesis submitted to the Faculty of the

Virginia Polytechnic Institute and State University

in partial fulfillment of the requirements for the degree of

Master of Science

in

Electrical Engineering

APPROVED:

Richard O. Claus

Richard O Claus, Chairman

A. Safaai-Jazi   _Ronald J. Pieper_

Ahmad Safaai-Jazi   Ronald J. Pieper

April 1988

Blacksburg, Virginia

Modal Interference Techniques for Strain Detection in Few-Mode Optical Fibers

by

Bradley Dean Duncan

Richard O Claus. Chairman

Electrical Engineering

(ABSTRACT)

Interference between the modes of an optical fiber results in specific intensity patterns which can be modulated as a function of disturbances in the optical fiber system These modulation effects are a direct result of the difference i. propagation constants of the constituent modes. In this presentation it is shown how the modulated intensity patterns created by the interference of specific mode groups in few-mode opt· al fibers (V < 5.0) can be used to detect strain. A detailed discussion of the modal phenomena responsible for the observed strain induced pattern modulation is given and it is shown that strain detection sensitivities on the order of 10^{-9} can be expected. Data taken during the evaluation of an actual experimental strain detection system based on the developed theory is also presented.

Acknowledgements

I would like to express my sincere gratitude to Dr R.O. Claus, my graduate advisor, for his guidance, assistance and patience. Special thanks goes to Dr. A Safaai-Jazi for his encouragement and help in understanding the many subtle concepts of modal analysis. Thanks also goes to Dr. R. Pieper for serving on my graduate Committee.

I wish also to gratefully acknowledge Brian Brennan, Bill Spillman, Jeff Lord and the other members of the Advanced Development Organization of Simmonds Precision, Vergennes, VT, for providing me with the resources with which to carry out the experimental tests of the modal domain sensing concepts developed in this thesis and for making my brief stay in Vermont a very pleasant one.

Many thanks to my fellow graduate students at the Fiber & Electro-Optics Research Center, Virginia Tech, for their advice, consultation and lasting friendship. Thanks also to Robin Rogers for her assistance in preparing the figures. And finally, sincere thanks to my parents and to my very dear friend Lucie Pelletier for their unending support and encouragement.

Table of Contents

List of Illustrations

1.0 INTRODUCTION

The past several years have given rise to many optical fiber sensing techniques which may be employed in systems to detect such physical observables as temperature. pressure, displacement and strain [1]. As sensing devices, optical fibers are attractive in part due to their small size. flexibility, ruggedness and intrins'c dielectric nature. In addition, their proclivity to be highly sensitive to external perturbations is quickly making optical fibers the sensing devices of choice for many passive non-intrusive sensor applications.

Simply put. optical fiber sensors exploit the effects of perturbations and external factors on the light in the fiber. S¡ɔcifically, the intensity. phase and polarization are among those properties of light which are available for alteration and the detection of these changes is the basis of most fiber optic

sensors. Unparalleled in sensitivity are the phase modulated sensors. a classic example of which is the dual-fiber Mach-Zehnder interferometer [2]. Because it is based on an absolute phase modulation scheme, however, such a sensor tends to be quite complex, with the reference phase and quadrature point often needing to be actively controlled.

By comparison, sensor systems utilizing single-fiber modal interference schemes, such as those to be discussed in this thesis, essentially have the two arms of the interferometer within the same environment. This provides for a high common mode rejection capacity while affording the system the further advantages of simplicity and increased ruggedness. with no need for couplers. Though remaining highly sensitive, as will be shown. some sensitivity will be sacrificed in a single-fiber interferometer, or modal domain sensor, due to the fact that the sensor mechanism will now be based on differential phase modulation.

Previous work with modal domain sensors has involved the detection of such observables as quasi-static strain [3,4], vibration [5], and acoustic emission [6]. Often, though, this work was done without the prior benefit of a rigorous theoretical basis for interpreting the sensor output. Also, no effort as yet has been made to theoretically predict and experimentally verify the ultimate sensitivities achieveable with given modal domain sensor systems. Finally,

no attempt has yet been made to use anything but large discrete optical components in a modal domain sensor system design. This last point will, of course, limit the practicality of single-fiber modal interference based systems.

The objectives of this thesis are therefore several. First the theoretical considerations of the behavior of the intensity patterns caused by the interference of specific mode groups in few-mode optical fibers (V < 5 0) will be thoroughly discussed and it will be shown how these intensity patterns, when modulated as a function of strain, can be used as a sensor mechanism. Secondly, the ultimate sensitivities achieveable with modal domain sensor systems will be investigated both theoretically and experimentally. And finally, a discussion of how modal interference techniques can be used in simple, practical sensor systems which avoid the use of large discrete optics will be presented. To begin, however, a brief review of several topics relevant to the understanding of fiber optics will be presented.

2.0 REVIEW OF BASIC FIBER OPTICS

This chapter primarily consists of a series of discussions of topics relevant to the understanding of basic fiber optics and is meant as a review   More detailed considerations of all topics may be obtained from their respective references. Subjects tc be addressed include linearly polarized (LP) modes in weakly guiding fibers. photodetectors and their associated noise factors and the photoelastic effect in optical fibers under strain. We will begin, however, with a brief review of optical fiber classification.

2.1 Optical Fiber Classification

Fibers used for optical communications and sensing are waveguides made of transparent dielectrics whose function is to guide visible and infrared light. A typical optical fiber consists of an inner cylinder of glass, called the core, surrounded by a cylindrical shell of slightly lower index of refraction called the cladding. Optical fibers may be classified in terms of the refractive index profile of the core and whether one mode (single-mode) or many modes (multimode) are allowed to propagate in the waveguide. If the core has a uniform index of refraction n_1 it is called a *step-index fiber*. If the core has a nonuniform index of refraction that gradually decreases from the center toward the core-cladding interface the fiber is called a *graded-index fiber*. The cladding surrounding the core typically is of a uniform index of refraction n_2, where

$$n_2 = n_1(1 - \Delta) \qquad (2.1.2)$$

in a step-index fiber. This relation is also approximately true for graded-index fibers where n_1 would then represent the index of refraction at the center of the core. The parameter Δ is called the *core-cladding index difference* and nominally $\Delta \leq 0.01$. Figure 1 shows typical dimensions of commonly used optical fibers. And finally, as the chapters to follow will be dedicated to

describing modal interference as a sensor mechanism in step-index optical fibers we note here that a typical value of the core index in a step-index fiber is $n_1 \simeq 1.458$ [7]. We now turn our attention to the guided modes allowed to propagate in step-index optical fibers.

2.2 Linearly Polarized Modes

Put simply, a *mode* in an optical fiber waveguide (or any other waveguide) is an allowable field configuration, for a given waveguide geometry, that satisfies Maxwell's equations (or the derived wave equations) and all the boundary conditions of the problem [7]. In an optical fiber a guided mode is one in which electromagnetic energy is carried along the fiber axis only and whose transverse field components decay to zero in an approximately exponential manner at distances far from the core. For these modes the integral

$$P = \int_{z=const} |\vec{E}|^2 \, dx \, dy,\tag{2.2.1}$$

which is a measure of the power flow, is finite. Also, at any given operating frequency the number of guided modes is finite with each mode being associated with a cutoff frequency. That is, for a guided mode to be allowed

to exist, its cutoff must be less than the frequency of operation. It can further be shown that a mode will remain guided as long as its propagation constant β satisfies the condition

$$n_2 < \beta/k_0 \leq n_1 . \qquad (2.2.2)$$

where in the case of the step-index fiber, as presently under consideration, n_1 and n_2 are the indicies of refraction of the core and cladding, respectively, and where $k_0 = 2\pi/\lambda_0$, with λ_0 being the free space source wavelength. Note, though, that in order for a guided mode to carry power along the fiber it must be excited by an external source. Indeed, since modes are simply analytical solutions to the wave equations in a waveguide and represent *allowed* field configurations it is quite possible to have mode solutions of a fiber (or other waveguide) which do not carry power due to their not being externally excited [8]. A detailed discussion of selective mode excitation will not be given here, but it will be seen later that the excitation of specific mode groups in an optical fiber will give rise to some very interesting sensor mechanisms. Recall, however, that for light entering a fiber to excite a guided mode it must in general satisfy the condition that it enters the core through an acceptance cone defined by the numerical aperture, or NA, of the fiber. A physical interpretation of a fiber NA is given in Figure 2 with the analytical value of NA given as

$$NA = \sqrt{n_1^2 - n_2^2} \simeq n_1\sqrt{2\Delta} \qquad (2.2.3)$$

in a step-index optical fiber. This result is derived from considering that light guided in a fiber must satisfy the total internal reflection requirements at the core-cladding interface according to Snell's law of refraction [9].

In practical optical fibers the refractive indices of the core and cladding are nearly equal with $n_1 \geq n_2$ and $\Delta << 1 0$. The condition $\Delta << 1 0$ is called the *weak guidance* condition, and the corresponding optical fibers are called *weakly guiding fibers*. The concept of weak guidance is better appreciated if one notes that for $\Delta = 0$ the infinite clad optical fiber reduces to a homogeneous medium with no guidance properties. For $\Delta << 1.0$ but $\Delta \neq 0$ the guidance of energy is considered weak. However, this does not imply loose confinement of power to the core; at very high frequencies the energy can be tightly bound to the core, even in a weakly guiding fiber. Furthermore, the condition $\Delta << 1.0$ is mandated in both single-mode and multimode fibers. In multimode fibers $\Delta << 1.0$ is required for low inter-modal dispersion since the delay time between the lowest order and highest order modes is proportional to Δ. In a single mode fiber $\Delta << 1.0$ is necessary in order to have manageable core sizes. In addition, the weak guidance condition leads to greatly simplified modal expressions which are quite valid for short lengths of fiber, as is the case with typical fiber sensors.

In a step-index, lossless and non-magnetic optical fiber that is translationally invariant along the axial direction, the guided mode solutions can be summarized in phasor form as follows:

$$\bar{e}(r\,\varphi) = A\,J_\ell(Ur/a)\begin{Bmatrix}\cos(\ell\varphi)\\\sin(\ell\varphi)\end{Bmatrix}\begin{Bmatrix}\hat{a}_x\\\hat{a}_y\end{Bmatrix}\quad r<a \qquad (2\,2.4)$$

$$\bar{h}(r,\varphi) = -Y_1\big(\bar{e}(r,\phi)\times\hat{a}_z\big)$$

and

$$\bar{e}(r\,\varphi) = A\,K_\ell(Wr/a)\begin{Bmatrix}\cos(\ell\phi)\\\sin(\ell\phi)\end{Bmatrix}\begin{Bmatrix}\hat{a}_x\\\hat{a}_y\end{Bmatrix}\quad r>a\,. \qquad (2\,2\,5)$$

$$\bar{h}(r,\varphi) = -Y_2\big(\bar{e}(r,\varphi)\times\hat{a}_z\big)$$

where there is an implied multiplicative factor of $e^{-j(\beta z-\psi)}$, which represents the phase of the mode and where $\ell = 0,1\,2,\ldots$ with r, ϕ, and z being the cylindrical coordinates representative of the fiber geometry Also, $J_\ell(x)$ is the Bessel function of the first kind, order ℓ, and $K_\ell(x)$ is the modified Bessel function of the second kind, order ℓ $J_\ell(x)$ is plotted for orders 0,1 and 2 in Figure 3 The amplitude coefficient A is determined by the source input conditions and is assumed to absorb any signs (plus or minus) at present, while Y_1 and Y_2 are the characteristic admittances of the core and cladding, respectively. In addition, the parameters U and W are given by

$$U = K_0 a \sqrt{n_1^2 - \overline{\beta}^2} \qquad (2\ 2\ 6)$$

$$W = K_0 a \sqrt{\overline{\beta}^2 - n_2^2} \ . \qquad (2.2.7)$$

where "a' is the fiber core radius and $\overline{\beta} = \beta/k_0$, with β being the modal propagation constant [8]

Notice in equations (2 2.4) and (2 2.5) that the electric fields are either x or y directed Since polarization is defined by the direction of the electric field, the modes described by equations (2 2 4) and (2 2.5) are linearly polarized and are thus called *linearly polarized* or *LP* modes The bracketed quantities in equations (2 2.4) and (2 2.5) may be taken as multiplicative factors in any combination with the only stipulation being that the magnetic field vectors be orthogonally oriented with respect to the electric field vectors. Modes containing the $\cos(\ell\phi)$ multiplicative factor are called *even* modes while modes containing the $\sin(\ell\phi)$ multiplicative factor are called *odd* modes. For all cases except when $\ell = 0$ the modes have a degeneracy of four (i.e.. even, x-polarized; even, y-polarized; odd, x-polarized and odd, y-polarized). When $\ell = 0$ it is obvious that *LP* modes are independent of ϕ and therefore have a degeneracy of two (i e.. x-polarized and y-polarized) [8].

The propagation constants β for LP modes are found by solving the following characteristic equation, the solutions of which are plotted in Figure 4 [9,10]

$$\frac{J_\ell(U)}{UJ_{\ell-1}(U)} + \frac{K_\ell(W)}{WK_{\ell-1}(W)} = 0 , \quad \ell = 0,1,2,.. \quad . \tag{2.2.8}$$

Note that the solutions to this characteristic equation actually appear as functions of β vs ω, where ω is related to the source wavelength λ_0 by $\omega\lambda_0 = 2\pi c$, with c being the speed of light in free space. The solutions are, however, plotted in Figure 4 in the normalized form of b versus V where b is the normalized propagation constant given by

$$b = \frac{(\beta/k_0)^2 - n_2^2}{n_1^2 - n_2^2} . \tag{2.2.9}$$

The normalized frequency V is given in terms of the source wavelength and fiber parameters by

$$V = k_0 a\sqrt{n_1^2 - n_2^2} = k_0 a(NA) \simeq k_0 a n_1\sqrt{2\Delta} . \tag{2.2.10}$$

Note also that there are multiple solutions to the characteristic equation for each value of ℓ. Therefore, specific LP modes are typically labeled $LP_{\ell m}$, where the propagation constant for the $LP_{\ell m}$ mode is the mth solution for β, at a given frequency (or source wavelength), when the principal mode number ℓ takes a particular value. For example, the LP_{23} mode is the mode whose propagation

constant β is found from the third solution to the characteristic equation when $\ell = 2$ [8].

Guided mode cutoff occurs when $b = 0$ and as can be seen in Figure 4, a fiber is operated in a single-mode regime when $V \leq 2.405$. As V increases (by decreasing the source wavelength λ_0 or by increasing the core radius a) more and more modes are allowed to propagate in a fiber until the fiber enters the multimode operating regime. Strictly speaking a fiber is a multimode fiber if more than one mode is allowed to propagate. Practically, though, multimode fibers are taken as those fibers with extremely high V values, typically in excess of $V = 50$. To achieve these high V values the core radii are usually made very large in multimode fibers, thus making the fiber multimode for a wide range of source wavelengths. By comparison, single-mode fibers typically have very small core radii. For example, a fiber intended for single mode operation at a nominal source wavelength of 1300 nm will have a core radius of approximately 4.5 μm (see again Figure 1). Using these values in equation (2.2.10), with $n_1 = 1.458$, we can solve for Δ to find $\Delta \simeq 0.003$. It is therefore obvious that, as mentioned earlier, Δ must be much less than unity for single-mode fibers to have manageable core sizes.

Of interest in the study of modal domain sensing techniques are those fibers which allow the propagation of only a few modes. Such fibers will often be

called *few-mode fibers*. typically with $V < 5$, and are of interest since it is much simpler to study and characterize the interference of a few modes than it is the many modes in a true multimode optical fiber. Recall that modal domain sensors are essentially self-referenced interferometers which exploit modal interference as the basis for a sensor mechanism. Few-mode fibers are also attractive for use in modal domain sensors since, as in all fiber optic sensors, the sensor data will be collected by monitoring the modulated intensity distribution at the fiber/sensor output. These intensity distributions (or patterns) at the output of modal domain sensors are created due to the interference of the guided modes in the fiber and are modulated as a function of the environmental disturbances being detected. For modal domain sensors using few-mode fibers these output intensity patterns are often qualitatively simple and well behaved as a function of disturbance and therefore give rise to simple sensor systems.

One can cause a fiber to be few-moded by simply injecting into a single-mode fiber light of a shorter wavelength than that typically injected for single mode operation. For example, it will later be shown that a 4 5 μm core radius fiber, usually intended for single-mode operation at $\lambda_0 = 1300$ nm, will have $V = 4.616$ when the source wavelength is reduced to $\lambda_0 = 633$ nm, as with He-Ne gas laser injection. We can thus see from Figure 4 that only the LP_{01}, LP_{11}, LP_{21} and LP_{02} modes and their degeneracies will be allowed to

propagate. Such a fiber is easily seen to be few-moded. Plots of the intensity distributions of the LP_{01}, LP_{11}, LP_{21} and LP_{02} modes can be found in Figures 5-8, respectively. These and other similar plots to be addressed later were created using the numerical expansions for $J_0(x)$ and $J_1(x)$ given in Appendix C and the FORTRAN programs given in Appendix D. It should be mentioned that the x and y values of Figures 5-8 are given in microns and that these figures are valid only for $r = \sqrt{x^2 + y^2} \leq 4.5\,um$, as these plots were created considering only the modal solutions in the core for the case of 633 nm light injection into a 4.5 μm radius fiber, as discussed above. The intensity beyond $r = 4.5\,\mu m$ decays approximately exponentially. Finally, it should also be mentioned that in Figures 5-8 no interference has been considered and that the amplitudes of the modal intensity distributions are quite arbitrary with only the general pattern shape being of any importance at present.

2.3 Photodetectors

Data is collected from a fiber optic sensor by monitoring the modulated intensity distribution at the sensor output. Typically this monitoring is achieved through the use of a photodetection circuit. Such a photodetection circuit is shown in Figure 9 with its equivalent circuit. It is seen that the

photodiode is modeled by a series bulk resistance R_s and a total capacitance C_d consisting of junction and packaging capacitances. A bias (or load) resistance is given by R_L and the amplifier following the photodiode has an input capacitance C_a and a shunt resistance R_a. In a practical circuit, however, R_s is much smaller than R_L and can be neglected. Also, C_d is usually small and only affects the high frequency response (rise time) of the photodetection circuit Thus, for low frequency input signals, such as those created at the output of the modal domain sensors to be discussed later, the capacitance C_d is seen essentially as an open circuit. Furthermore, for the present discussion it will be assumed that the amplifier is used as a high impedence buffer with unity gain, as would be the case at the input to an oscilloscope, for instance. For low frequency or DC signals the photodetection circuit is therefore seen to reduce quite simply to a photodiode in parallel with a load resistance [9].

Optical power incident on the photodiode is converted into a photocurrent when the excess electron-hole pairs created by the incident light are swept out of the photodiode depletion region by the fields created by the high reverse bias voltage ($\sim$ 10 V for *pin* photodiodes). The photocurrent is related to the incident optical power P_0 by the relation

$$I_p = \mathscr{R} P_0 \ . \tag{2.3.1}$$

where $\mathcal{R}$ is called the *responsivity* of the photodiode and has the units of amps per watt. $\mathcal{R}$ is given in turn by the expression

$$\mathcal{R} = \frac{\eta q}{h\nu} \quad , \qquad (2.3.2)$$

where $h\nu$ is the energy of the incident photon, q is the electronic charge and η is the photodiode quantum efficiency which relates the number of electron-hole pairs created to the number of incident photons. For silicon photodiodes a nominal value of responsivity is $\mathcal{R} = 0.5$ A/W for common detection wavelengths [9] The photocurrent thus created causes a voltage across the load resistor given by

$$V_0 = \mathcal{R} P_0 R_L \quad . \qquad (2.3.3)$$

This is the quantity typically recorded when using simple photodetection circuits and the measured quantity V_0 is easily converted to a measure of incident optical power if the load resistance R_L and the responsivity $\mathcal{R}$ at the detection wavelength are known If we now consider that the incident optical power P_0 consists of an average or quadrature point component P_Q and a signal component ΔP such that $P_0 = P_Q + \Delta P$ we see that the electrical signal power created by the signal component of the incident optical power is given by

$$P_{ES} = (\mathscr{R} \, \Delta P)^2 \, R_L \; . \tag{2.3.4}$$

The principal noises associated with photodetectors are quantum or shot noise, dark-current noise generated in the bulk material of the photodiode, and the surface leakage current noise. For small and well packaged photodiodes, however, the surface leakage current noise is small and can be neglected. The shot noise arises from the statistical nature of the production and collection of photoelectrons when an optical signal is incident on a photodetector and sets a fundamental lower limit on receiver sensitivity when all other conditions are optimum. The RMS shot noise power is given as

$$P_{SN} = 2qI_Q B R_L \; . \tag{2.3.5}$$

where B is the detection bandwidth and I_Q is the average photocurrent given as $I_Q = \mathscr{R} P_Q$ where P_Q can be measured with no signal applied.

The photodiode dark current is the current that continues to flow when no light is incident on the photodiode. This is in general a combination of bulk and surface currents. However, the bulk dark current is usually dominant and arises from the electron-hole pairs which are thermally generated in the pn junction of the photodiode. The RMS bulk dark current noise is given as

$$P_{DB} = 2qI_D B R_L \tag{2.3.6}$$

where I_D is the primary detector bulk dark current and can be found for specific photodiodes in various vendor catalogs [9].

In addition to the detector noise factors just discussed the photodetector load resistor contributes an RMS thermal (Johnson) noise power given as

$$P_T = 4k_B TB \quad . \tag{2.3.7}$$

where k_B is Boltzman's constant and T is the absolute temperature. This noise can be reduced by cooling the detection circuit [9].

The power signal-to-noise ratio S/N at the output of an optical receiver is now easily seen to be

$$S/N = \frac{P_{ES}}{P_{SN} + P_{DB} + P_T} \quad . \tag{2.3.8}$$

or

$$S/N = \frac{(\mathcal{R}\Delta P)^2}{2qB(\mathcal{R}P_Q + I_D) + \dfrac{4k_B TB}{R_L}} \quad . \tag{2.3.9}$$

Of special interest is the case when S/N goes to unity. At this point the signal power just equals the noise power and enables one to determine the minimum

detectable optical signal ΔP_{min}. When only photodetector and load resistor noise factors are accounted for, we find that

$$\Delta P_{min} = \frac{1}{\mathcal{R}}\left(4qB(\mathcal{R}P_Q + I_D) + \frac{8k_B TB}{R_L}\right)^{\frac{1}{2}} \tag{2.3.10}$$

and in the shot noise limited case we find that

$$\Delta P_{min(S/N)} = \frac{1}{\mathcal{R}}(4qB(\mathcal{R}P_Q + I_D))^{1/2} . \tag{2.3.11}$$

where a factor of 2 has been included in the noise power terms of equations (2 3.10) and (2 3 11) due to the fact that at the operating point the incident optical power is uncertain to within $\pm$(shot noise and/or thermal noise).

Note that this analysis has been for *pin* photodiodes only and that the shot noise limit of detection is practically unrealizable. In addition, if one must operate a photodetection circuit at elevated temperatures or if it is impractical to use a large load resistor, which would reduce the thermal noise component of equation (2.3.10), one may have to resort to the use of an avalanche photodiode (or APD). An APD will also give a sharper system rise time for detection of high frequency signals but should not be used unless thermal noise is excessive This is due to the generation of excess shot noise during the avalanche process in APD's. At reasonable temperatures and for reasonable values of R_L the signal-to-noise ratio will be reduced by using an

APD. Finally, it should be mentioned that it has been assumed in the previous discussions that noise factors arising from sources other than the photodiode or its load resistor are negligible. This is reasonable only in a laboratory or other situation where environmental factors can be controlled We now turn our attention to a discussion of the photoelastic effect in optical fibers under strain

2.4 The Photoelastic Effect

Recall that the phase of a mode is given by $\phi = \beta z - \psi$ where ψ is a random phase term. Since the modal domain sensors to be discussed in the next chapter will derive their output from a differential modal phase modulation (i e., modal interference) as a function of strain, it is important to discuss how the phase of a mode changes as a function of fiber strain.

As a fiber is strained three principal factors act to change the modal phase. First, the fiber length changes. Second, the index of refraction changes due to the photoelastic effect and finally, the fiber diameter reduces. The change in phase due to these effects is thus

$$\Delta\varphi = \frac{\partial\varphi}{\partial z}\Delta z + \frac{\partial\varphi}{\partial n_1}\Delta n_1 + \frac{\partial\phi}{\partial D}\Delta D$$

$$\Delta\phi \simeq \beta\Delta z + z\frac{\beta}{n_1}\Delta n_1 \ , \tag{2.4.1}$$

where the effect of the change in fiber diameter is considered negligible and where $\partial\beta/\partial n_1 = \beta/n_1$ [1] Also from [1], for low order modes, we have

$$\Delta n_1 = \left\{ -\frac{1}{2} n_1^3 [\varepsilon_z(1-v)p_{12} - v\varepsilon_z p_{11}] \right\} \ , \tag{2.4.2}$$

where ε_z is the axial strain v is Poisson s ratio. n_1 is the index of the core and p_{11} and p_{12} are the photoelastic constants. Reasonable values of these unitless constants are given for silica as follows [4]

$$v = 0\ 17$$
$$p_{11} = 0.12$$
$$p_{12} = 0.27$$
$$n_1 = 1.458$$

By substituting equation (2 4 2) into equation (2.4 1) and rearranging terms we find that

$$\Delta\phi = \beta\Delta z \left\{ 1 - \frac{1}{2} n_1^2 [(1-v)p_{12} - vp_{11}] \right\}$$

$$\Delta \varphi = \beta \, \Delta z \, \{ z \} \,. \qquad\qquad (2.4\ 3)$$

where the relation $z \times \varepsilon_z = \Delta z$ has been used. Using the constants given above we see that $\alpha = 0.78$. Although this is a reasonable value of α, the true value may change from fiber to fiber. Experimentally determined values have been found as large as $z = 0.92$, as will be seen later. In any case, though, it is clear that due to the photoelastic effect a fiber under strain will see a significant reduction of the core index of refraction and therefore a significant reduction in the effective optical pathlength of the modes in the fiber. This results in a change in modal phase in a fiber under strain which is less than that expected if the fiber simply undergoes pure elongation

When a fiber supports more than one mode it is also important to investigate how the differential phase of the modes is influenced by strain. Consider two modes with phases $\phi_1 = \beta_1 z - \psi_1$ and $\varphi_2 = \beta_2 z - \psi_2$, respectively. The differential phase is given as

$$\phi_{12} = (\beta_1 - \beta_2)z - (\psi_1 - \psi_2) = \Delta \beta z - \Delta \psi \,. \qquad\qquad (2.4.4)$$

We may now consider that $\phi_{12} = \phi_0 + \Delta\phi_{12}$, where ϕ_0 is the initial differential phase of the modes in a no strain situation and where $\Delta\phi_{12}$ is the differential phase change induced as the fiber is strained. In an exactly analogous manner that was used to prove the result of equation (2.4.3) we can show that

$$\Delta \dot{\phi}_{12} = \Delta \beta \, \dot{\Delta z} \, \{x\} \quad . \tag{2 4 5}$$

so that

$$\phi_{12} = \Delta \beta \varepsilon_z L_f(x) + \phi_0 \quad . \tag{2 4 6}$$

where $\varepsilon_z L_f = \Delta z$ and L_f is the gage length of, say, a fiber optic sensor. Note also that $\varphi_0 = -\Delta \psi$. As will be evident in the next chapter the relationship given in equation (2 4 6) is extremely important in the study of fiber optic strain sensors.

One last comment should be made before concluding this discussion. That is, note that in the previous analyses it has been assumed that the amplitudes of the modes in a fiber under strain remain constant and that only the modal phase is influenced as strain is varied. This is not exactly the case since the amplitude of a mode is a function of $U = k_0 a \sqrt{n_1^2 - \bar{\beta}^2}$, in the core region, and both n_1 and $\bar{\beta}$ are functions of strain. However, only very large amounts of strain vary n_1 or $\bar{\beta}$ appreciably so that U will essentially remain constant with strain. For instance,

$$n_1 = n_1(\varepsilon_z) \simeq 1.458 + \Delta n(\varepsilon_z) = 1.458 - (0.32)\varepsilon_z \tag{2.4.7}$$

using the previous calculation for Δn in equation (2.3 2) It is thus seen that for strains even on the order of one percent (which is near the breaking point of

most fibers) n_1 remains nearly constant. A similar result can be obtained for $\bar{\beta}$ as a function of strain, making the assumption of constant field amplitudes quite valid.

2b   2a

2a = 100μ
2b = 140μ

MULTIMODE STEP INDEX

2b   2a

2a = 50μ (62.5μ)
2b = 125μ

MULTIMODE GRADED INDEX

2b   2a

2a = 9μ (1300nm)
2b = 125μ

SINGLE MODE STEP INDEX
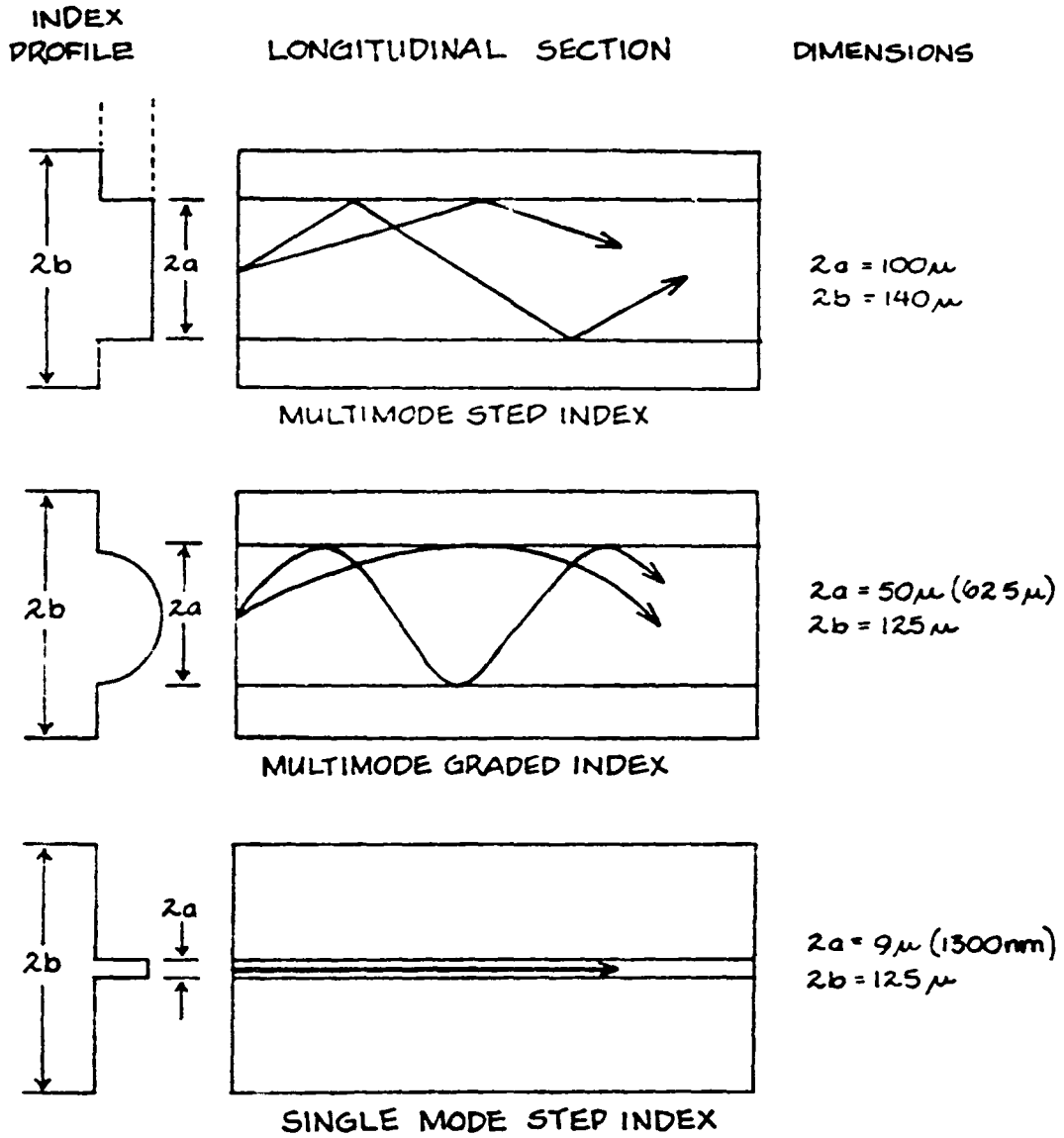
Figure 1. Optical fiber geometry summary

2.0 REVIEW OF BASIC FIBER OPTICS

LIGHT RAYS

$NA = SIN \theta$

ACCEPTANCE
CONE

θ
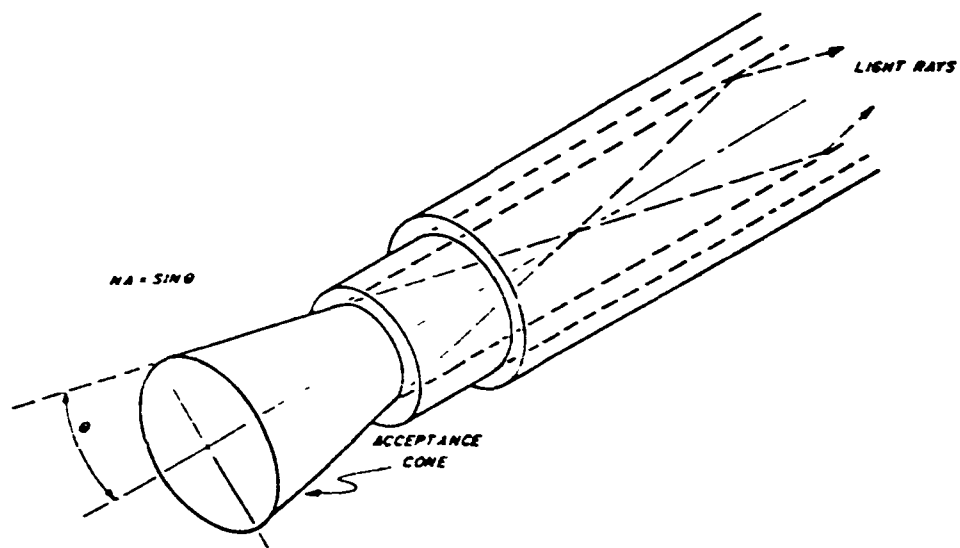
Figure 2. Numerical aperture (NA) of an optical fiber [16]
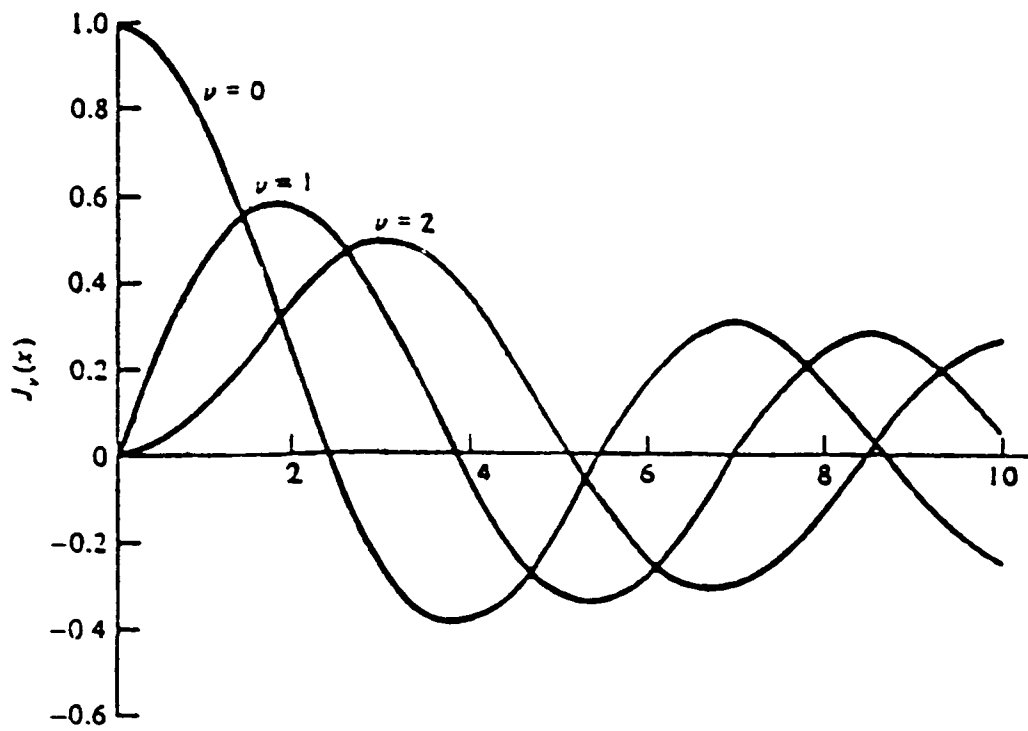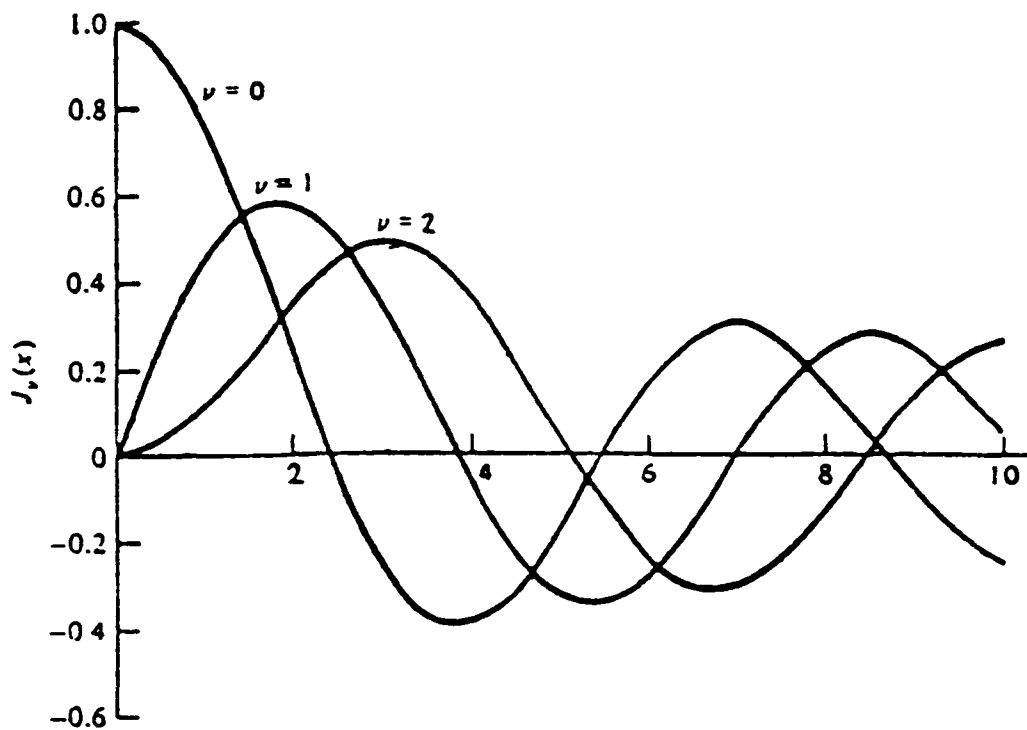
Figure 3. Bessel's function of the first kind for the first three orders [9]

Figure 3. Bessel's function of the first kind for the first three orders [9]

2.0 REVIEW OF BASIC FIBER OPTICS
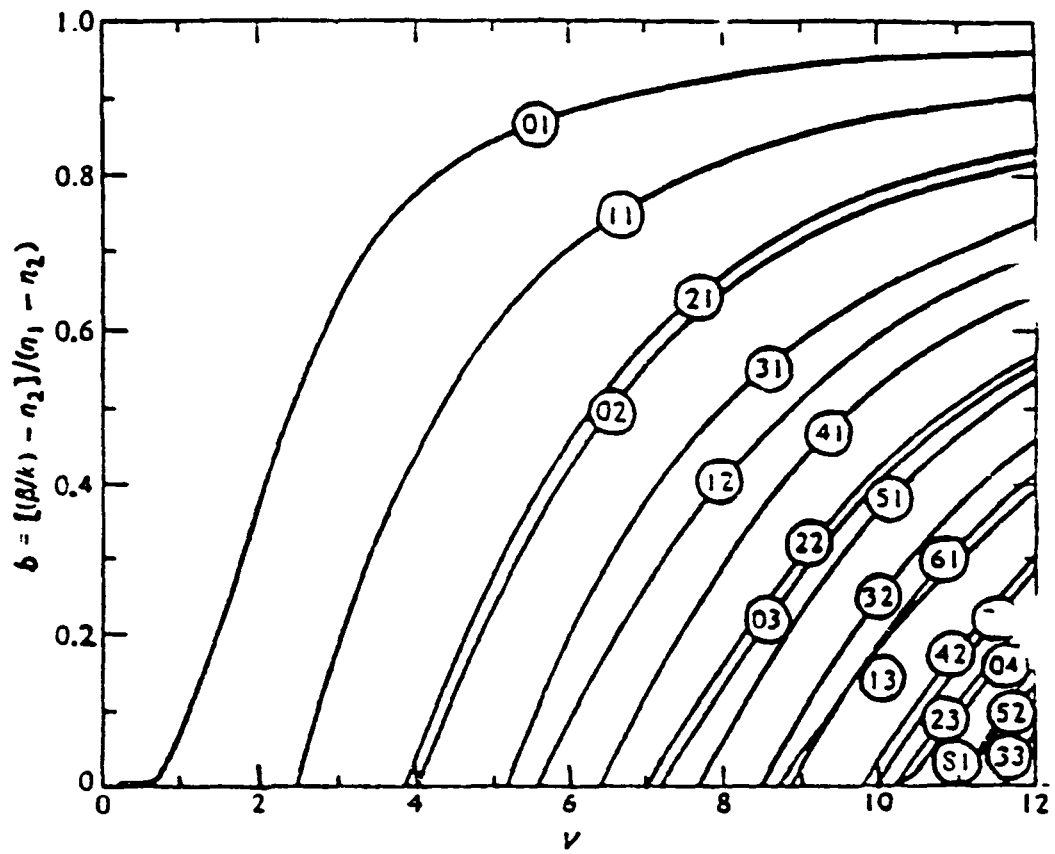
Figure 4. The normalized b versus V curves [9]
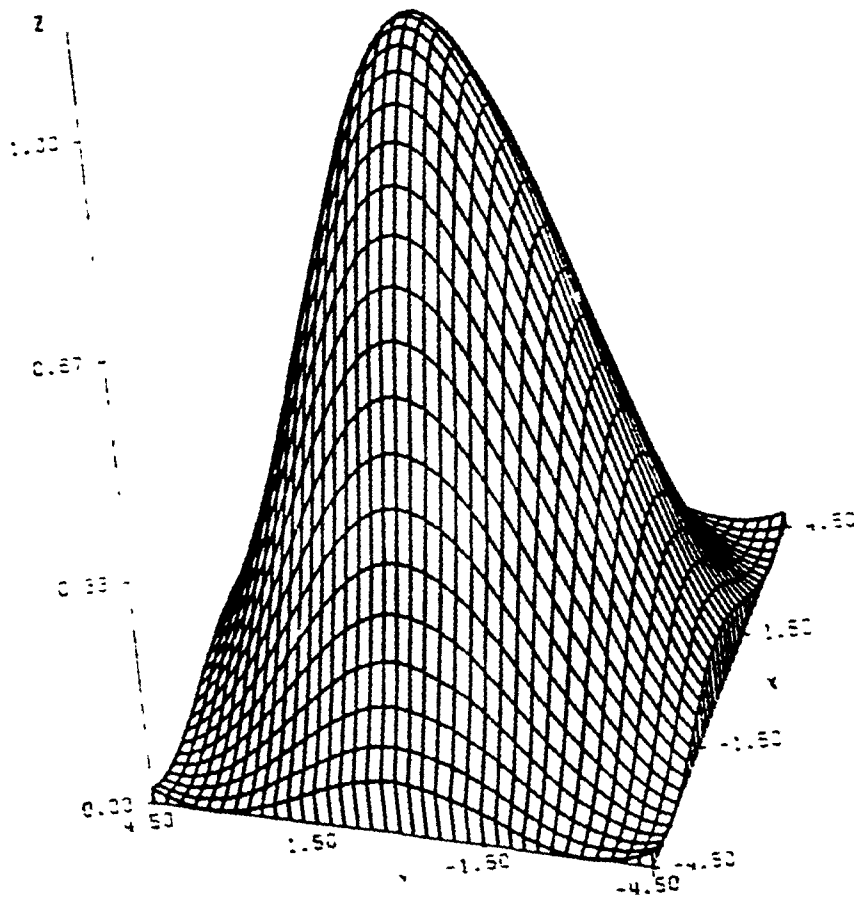
Figure 5.   Intensity distribution of the LP_{01} mode

29

2.0 REVIEW OF BASIC FIBER OPTICS
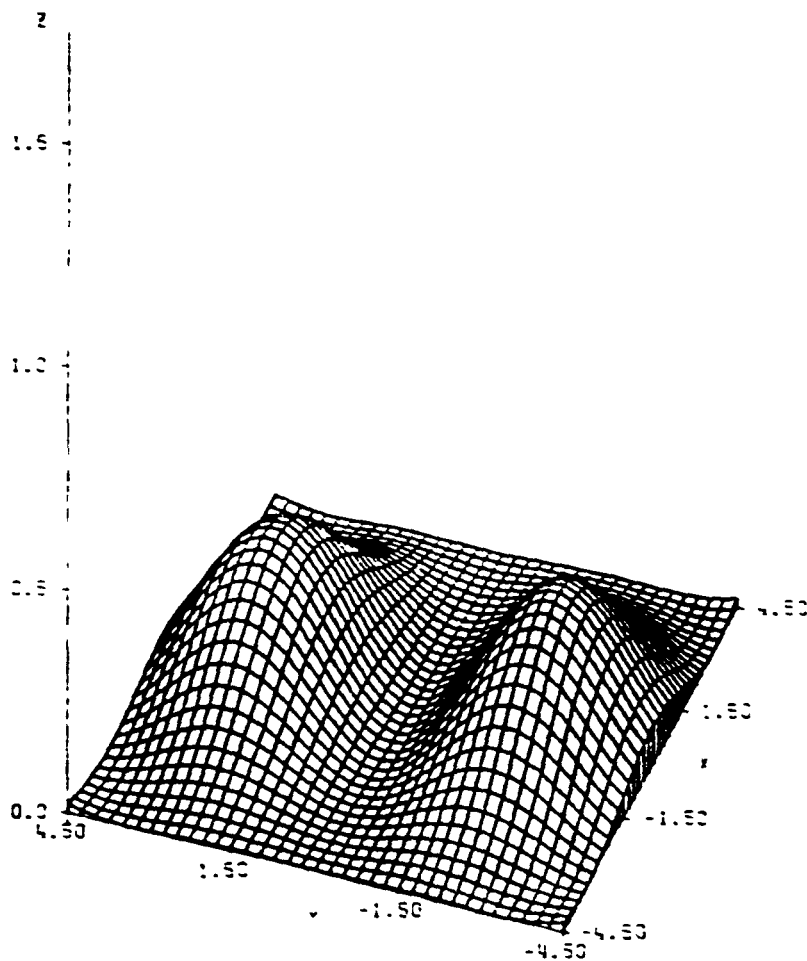
Figure 6. Intensity distribution of the LP_{11} mode
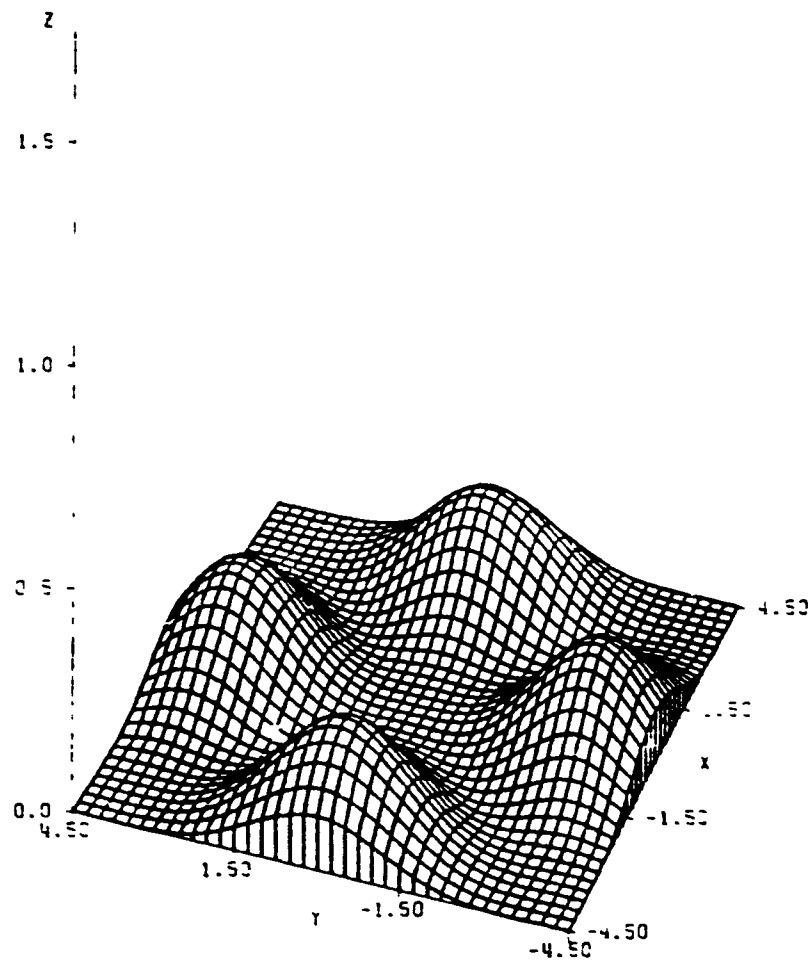
Figure 7. Intensity distribution of the LP_{21} mode
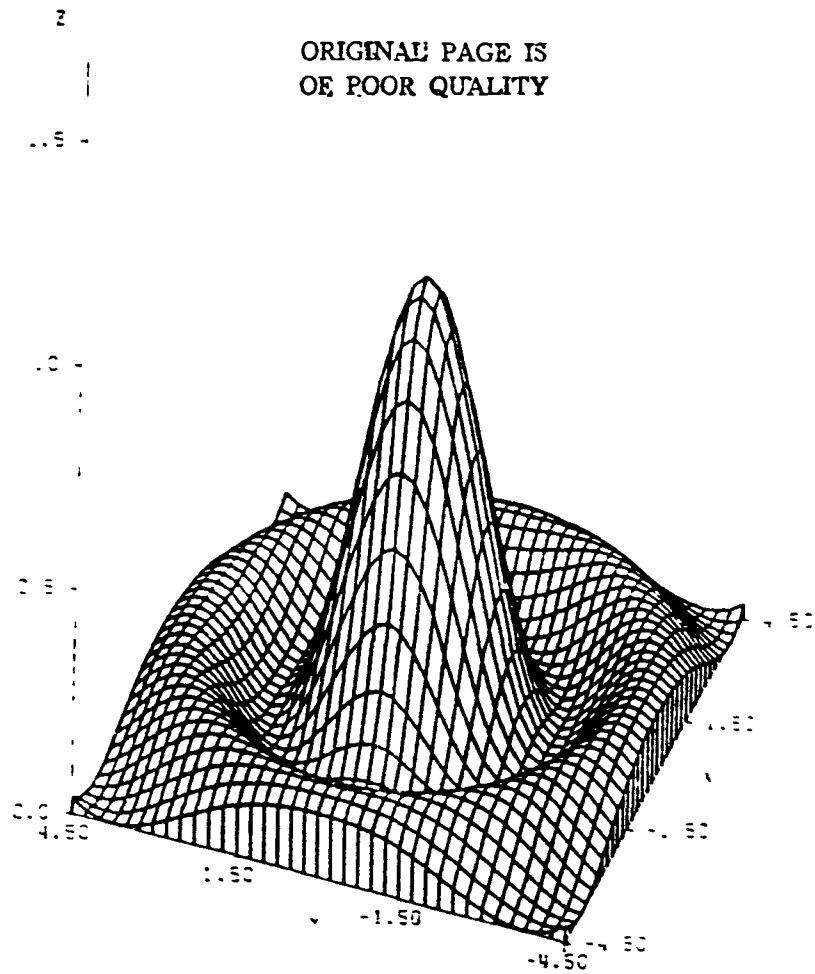
Figure 8. Intensity distribution of the LP_{02} mode

BIAS VOLTAGE

$h\nu$ PHOTODIODE

R_L

AMP OUTPUT

(a)

R_s

PHOTO-DIODE

$h\nu$

C_d R_L R_a C_a AMP

(b)
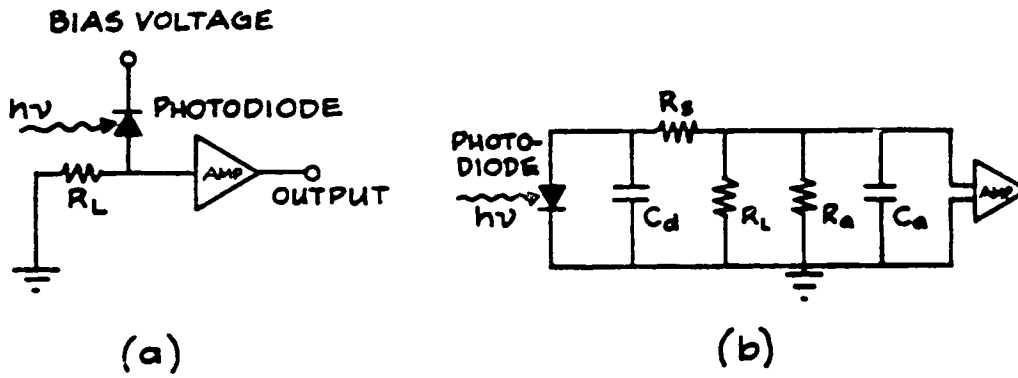
Figure 9. A simple photodetector and its equivalent circuit [9]

3.0 MODAL DOMAIN SENSING

Modal domain sensing is a fiber optic sensing technique based on the differential phase modulation occuring as a function of disturbance between the interfering guided modes of an optical fiber As we know, specific mode groups will propagate in a fiber and interfere to cause characteristic intensity distributions. or patterns. at the fiber output. as is shown in a very simple fashion in Figure 10. When the fiber is subjected to a disturbance. these intensity patterns are modulated as a direct function of the external disturbance and by monitoring this pattern modulation, often by using simple spatial filters. one can obtain information about the disturbance.

Strictly speaking, any sensor based on the interference of modes in an optical fiber can be called a "modal domain sensor." However, of special interest are those sensors based on modal interference in few-mode optical fibers with

V < 5 0. Such sensors are qualitatively simple in that since only a few modes are allowed to propagate it is possible to obtain simple, closed form solutions for the modulated output patterns which may manifest themselves. This is obviously an advantage when one wishes to design a *predictable* sensor. As a result, only modal domain sensors utilizing few-mode fibers will be discussed in the remainder of this chapter

Specifically, this chapter will be dedicated to describing the electromagnetic basis of the observed intensity pattern modulation, as a function of axial strain, of modal domain sensors using $9\mu m$ core diameter fiber at source wavelengths of 633 nm and 850 nm For simplicity we will use the notation MDS/9-633 and MDS/9-850 to describe these modal domain sensors at the source wavelengths of 633 nm and 850 nm, respectively. Also, note that although only axial strain considerations will be described here, modal domain sensors are not limited to measuring only axial strain. Axial strain is simply one of the most fundamental disturbances to which a fiber can be subjected and a detailed analysis of how axial strain affects an optical fiber sensor will provide the basis for designing sensors to measure other disturbances. For instance, if a sensing length of fiber is embedded in a material with known thermal expansion characteristics, a thermal sensor based on modal interference could be designed since the thermal expansion of the material can be related to induced axial strain in the embedded fiber

sensor   Sensors designed to detect many other environmental influences are also possible   We now proceed to a detailed discussion of the MDS/9-633 sensor.

3.1 The MDS/9-633 Sensor

It has been observed that when 633 nm light from a He-Ne gas laser is injected into a 9 μm core diameter fiber a symmetric three lobe pattern can be created at the output which exhibits pure rotation when the fiber is subjected to axial strain   Using a Photon Kinetics FOA-2000 fiber optic analyzer, the second mode cutoff for the above mentioned fiber, which is designed for single-mode operation at 1300 nm, has been determined to be 1215 nm (i.e., V = 2.405 at λ_0 = 1215 nm). Also. this fiber has a measured numerical aperture of NA = 0.1 (refer to Figure 11 for plots of the data generated by the FOA-2000 unit)   At a source wavelength of 633 nm this fiber is easily seen to have a normalized frequency of

$$V = 2.405 \, \frac{1215 \, nm}{633 \, nm} = 4.616 \quad .$$

This allows the propagation of the LP_{01}, LP_{11}, LP_{21} and LP_{02} modes and their degeneracies, as discussed in section 2.2. However. as the three lobe pattern

under discussion exhibits a central null, it is evident from Figures 5 and 8 that the LP_{01} and LP_{02} must not be excited in the fiber for the three lobe pattern to be created. If we further require that our source emits polarized light, say x-polarized, we are left with only four modes which may interfere to cause the rotating three lobe pattern of interest. Specifically, these modes are the x-polarized odd LP_{11}, even LP_{11}, odd LP_{21} and even LP_{21} modes and it can be shown that with a proper choice of amplitude coefficients, determined in reality by the launch conditions of the fiber, that these modes do interfere to cause the observed three lobe pattern and its well defined rotational behavior [11]. From equation (2 2 4) we see that the electric fields in the core of the above mentioned modes are given as

$$
\begin{aligned}
\vec{E}_{11}^e &= A_1^e \, J_1(U_{11}r/a) \cos\phi \, e^{-j(\beta_{11}z - v_{11}^e)} \, \hat{a}_x \\
\vec{E}_{11}^o &= A_1^o \, J_1(U_{11}r/a) \sin\phi \, e^{-j(\beta_{11}z - v_{11}^o)} \, \hat{a}_x \\
\vec{E}_{21}^e &= A_2^e \, J_2(U_{21}r/a) \cos2\phi \, e^{-j(\beta_{21}z - v_{21}^e)} \, \hat{a}_x \\
\vec{E}_{21}^o &= A_2^o \, J_2(U_{21}r/a) \sin2\phi \, e^{-j(\beta_{21}z - v_{21}^o)} \, \hat{a}_x
\end{aligned}
\qquad (3\ 1\ 1)
$$

Since the sensor behavior can be completely described by investigating only the interference of the mode solutions in the core, no further consideration will be given to the modal solutions for $r \geq a$.

The intensity pattern present at the fiber output is found from

$$I = \frac{1}{2} Re\left\{ (E_x \hat{a}_x \times Y_1 E_x \hat{a}_y) \cdot \hat{a}_z \right\} = \frac{1}{2} Y_1 |\bar{E}_x|^2 \ , \qquad (3.1.2)$$

where

$$E_x = (E_{11}^e - E_{11}^o) - (E_{21}^e - E_{21}^c) \qquad (3.1.3)$$

and Y_1 is the characteristic admittance of the core region

We now assume that the amplitude coefficients are real and that $A_1^e = A_1^o = A_1$ and $A_2^e = A_2^o = A_2$ with the further assumption that the odd terms of equation (3 1 1) are 90° out of phase with relation to their respective even terms, so that

$$\dot{\psi}_{11}^o = \dot{\psi}_{11}^e + 90^\circ = \dot{\psi}_{11} + 90^\circ$$

and

$$\psi_{21}^o = \psi_{21}^e - 90^\circ = \upsilon_{21} - 90^\circ$$

Adding the even and odd terms of the LP_{11} mode. it is easy to see that

$$(E_{11}^e + E_{11}^o) = A_1 J_1\left(\frac{U_{11}r}{a}\right)(\cos\phi + j\sin\phi)\, e^{-j(\beta_{11}z - \dot{\psi}_{11})}$$

or

$$(E_{11}^e + E_{11}^c) = A_1 J_1\left(\frac{U_{11}r}{a}\right) \epsilon^{-j\beta_{11}z - \psi_{11} - \phi)} \quad . \tag{3 1 4}$$

Similarly, adding the even and odd terms of the LP_{21} mode it is seen that

$$(E_{21}^e + E_{21}^o) = \cdots_2 J_2\left(\frac{U_{21}r}{a}\right) e^{-j\beta_{21} - \psi_{21} + 2\phi)} \tag{3 1 5}$$

With these last two results in mind we now find the output intensity distribution using equations (3.1.2) and (3 1 3). The result is

$$I = I_0\left(A_1^2 J_1^2\left(\frac{U_{11}r}{a}\right) - A_2^2 J_2^2\left(\frac{U_{21}r}{a}\right) \right. \\ \left. + 2A_1 A_2 J_1\left(\frac{U_{11}r}{a}\right) J_2\left(\frac{U_{21}r}{a}\right) \cos(\Delta\beta z - \Delta\psi - 3\phi)\right), \tag{3.1.6}$$

where $\Delta\beta = \beta_{11} - \beta_{21}$, $\Delta\psi = \psi_{11} - \psi_{21}$ and $I_o = Y./2$.

It should be evident that the intensity distribution of equation (3.1.6) results in a pattern consisting of three equal lobes displaced azimuthally by 120°. It should also be evident that this pattern rotates as the modes propagate through the fiber. The first two terms of equation (3.1 6) are simply background intensity terms and are constant. The sum of these two terms is plotted in Figure 12, where it is assuméd that $A_1 = A_2 = 1.0$ and where the x and y values are r'ven in microns The third term of equation (3.1.6) is the

term which gives rise to the pattern shape and rotational behavior as the modes advance in the z-direction and is plotted in Figure 13. The entire intensity distribution of equation (3 1.6) is plotted in Figure 14. As with Figure 12, Figures 13 and 14 are plotted assuming $A_1 = A_2 = 1.0$, with the x and y values being given in microns. The choice of A_1 and A_2 was made after evaluating several plots of equation (3 1 6), with the amplitude coefficients taken as parameters For $A_1 \simeq A_2$ it was seen that there were approximate radial intensity nulls in the calculated intensity distrubution, displaced by 120°, which agree very closely with experimental observations. In addition, the plots in Figures 12-14 are valid only for the core region of the fiber (i.e., the plots are valid only for $r = \sqrt{x^2 + y^2} \leq 4 5 \mu m$) and were plotted using the Bessel function mumerical expansions given in Appendix C and the FORTRAN programs of Appendix D. Notice also that for $A_1 = A_2$, the amplitudes of ι plots of Figures 13 and 14 are approximately equal in the radial region where the plotted functions are maximum, indicating that for this region in equation (3.1.6)

$$J_1^2\left(\frac{U_{11}r}{a}\right) + J_2^2\left(\frac{U_{21}r}{a}\right) \cong 2J_1\left(\frac{U_{11}r}{a}\right)J_2\left(\frac{U_{21}r}{a}\right) \quad . \qquad (3.1.7)$$

Using this result we can simplify equation (3.1.6) at the radial position where the function goes through a maximum to find

$$I = I'_0[1 + \cos(\Delta\beta z - \Delta\upsilon - 3\varphi)]$$

$$I = I_p \cos^2\left(\frac{\Delta\beta z - \Delta\psi - 3\varphi}{2}\right) , \qquad (3.1.8)$$

where I'_0 has incorporated into it the terms of equation (3 1.7) after they are factored from equation (3.1 6) In addition to obtain the result of equation (3 1 8), the trigonometric identity $1 + \cos(2x) = 2\cos^2(x)$ has been used, with the peak lobe intensity I_p taken as $I_p = 2I'_0$ Now let us discuss how this rotating three lobe pattern can be used to detect axial strain.

If we observe the three lobe pattern as it emerges from the end face of the fiber. we will see an intensity distribution similar to that shown in Figure 15(a). If we then increase the optical pathlength of the fiber by inducing an axial · strain, we will observe a pattern rotation. Due to the cosine squared nature of this pattern along the circular path which contains the lobe peaks, as given in equation (3 1.8) and as shown in Figures 15(a) and 15(b), it is seen that the most sensitive and linear position for monitoring the pattern rotation for the detection of axial strain is along this path at a position where the intensity is half that of the intensity of a lobe peak, as shown in Figure 15(b). In other words, if in a no strain situation we choose a fixed quadrature point in space to monitor on the three lobe pattern that both has an intensity of exactly half that of the peak intensity and is located on the circular path that contains the

lobe peaks, then for small increases in strain the intensity at this point will increase or decrease, as the patterns rotates, in direct proportion to the increase in strain.

If we define the azimuthal coordinate ϕ to take on the value $\phi = 0$ at our quadrature point, then equation (3 1 8) becomes

$$ I = I_\rho \cos^2\left(\frac{\Delta\beta z - \Delta\psi}{2} \right) \tag{3 1 9} $$

By now noticing that the $\Delta\beta z - \Delta\psi$ term in equation (3 1 9) represents an ensemble differential phase of the modes contributing to the rotating three lobe pattern, we can use arguments analogous to those used to prove the result of equation (2.4 6) so that the photoelastic effects may be included in equation (3.1 9), as the fiber is strained, to give

$$ I = I_\rho \cos^2\left(\frac{\Delta\beta\, \varepsilon_z L_f \chi - \phi_0}{2} \right) . \tag{3 1 10} $$

where ε_z is the axial strain, L_f is the gage length of the fiber sensor, χ is a constant less than unity that arises due to photoelastic effects and ϕ_0 is the ensemble differential phase of the modes in a no strain situation. If we now choose the quadrature point, or Q-point, such that the intensity at this point

increases with strain from an unstrained value of $I = I_p/2$. we must require that $\phi_o = -\pi/2$ so that at the Q-point

$$I = I_p \cos^2\left(\frac{\Delta\beta\, \varepsilon_z L_f\, x}{2} - \frac{\pi}{4}\right) \; . \tag{3 1.11}$$

In practice however. once the quadrature point has been set it will often be of more use to measure the change in intensity from the Q-point as a function of strain. This is found simply to be

$$\Delta I(\Delta\varepsilon_z) = \frac{\partial I}{\partial \varepsilon_z}\Delta\varepsilon_z = I_Q(\Delta\beta\, L_f\, x)\Delta\varepsilon_z \; . \tag{3 1 12}$$

where $I_Q = I_p/2$. Note that this result was obtained from an assumed no strain initial condition; however, it is still valid if the quadrature point is set with the fiber initially under strain. This is useful in a practical situation so that $\pm \Delta\varepsilon_z$ can be detected. Also note that this result is valid only for small changes in axial strain and that for small $|\Delta\varepsilon_z|$, the function $\Delta I(\Delta\varepsilon_z)$ is linear

Some other observations should be made at this point. First of all, since the response $\Delta I(\Delta\varepsilon_z)$ is linear, we can use the same sensor arrangement to measure static strain or small amplitude sinusoidal strain, where

$$\Delta I(\Delta\varepsilon_{peak}.t) = I_Q (\Delta\beta\, L_f\, x) \Delta\varepsilon_{peak} \cos(\omega t) \; , \tag{3.1 13}$$

If $\Delta \varepsilon_{peak}$ is the amplitude of the sinusoidal axial strain. This result will also hold for small amplitude vibrational strain such as would be caused if a fiber was bonded to a vibrating structure. "Small amplitude vibrational strain" is meant to indicate that the peak deflection of the vibrating structure is such that the fiber is tensioned without being appreciably bent. Second, since for small amplitude sinusoidal perturbations in the fiber the resulting change in intensity is also sinusoidal at the same frequency, the sensor has obvious uses as a vibration sensor. And finally, it should be noted that in an actual sensor arrangement, a detection circuit will be used to convert intensity to voltage. If a small spatially filtering pinhole is placed between the fiber end face and the photodetector to monitor the intensity pattern at the Q-point this voltage will be directly related to the area of the spatial filter, the responsivity of the photodetector and the load resistance of the detection circuit such that

$$\Delta V(\Delta \varepsilon_z) = V_Q (\Delta \beta \, L_f \, x) \, \Delta \bar{\varepsilon}_z$$

or

$$\Delta \bar{\varepsilon}_f = \frac{\Delta V}{V_Q (\Delta \beta \, L_f x)} \quad , \tag{3 1.14}$$

for the case of static strain in the fiber and

$$\Delta V(\Delta \varepsilon_{peak}.t) = V_Q (\Delta \beta \, L_f \, x) \, \Delta \bar{\varepsilon}_{peak} \, \cos(\omega t)$$

or

$$\Delta\bar{\varepsilon}_f(t) = \frac{\Delta V_{peak} \cos(\omega t)}{V_Q (\Delta\beta L_f \alpha)} \quad , \qquad (3\ 1.15)$$

for the case of small amplitude time harmonic strain and small peak displacement vibrational strain. Note that in equations (3.1.14) and (3.1.15) the notation $\Delta\bar{\varepsilon}_f$ has been used to indicate the average measured axial strain in the fiber This has been done since strain is a localized quantity and fiber optic strain sensors are only able to detect strain as averaged along their gage length. See Appendix A for further details of strain averaging In addition, the results of equations (3.1.14) and (3.1 15) will likely be of most use in an actual system with V_Q measured at quadrature and ΔV_{peak} and ω measured, say, using a spectrum analyzer.

Before discussing sensitivity let us discuss some of the practical aspects of the MDS/9-633 sensor. First, it should be noted that the interest in studying the rotating three lobe pattern of the MDS/9-633 sensor arose due to its ability to be created using simple optical components. Also, once created, this pattern is easy to work with due to its well defined rotational behavior and due to the fact that 633 nm light is visible and requires no special viewing equipment. Creating the rotating three lobe pattern, however, is not at all an easy task. Indeed, it often seems that obtaining this pattern requires a fair amount of luck

Once created, though the modal content of the pattern is unique and can be studied, as has been done in the past few pages, leading to the simple strain measurement results of equations (3 1.14) and (3.1.15). These equations state very simply how small changes in strain can be measured in the optical fiber of a MDS/9-633 sensor once the quadrature point has been properly set.

Setting the Q-point of the MDS/9-633 sensor. however. is another difficult task to accomplish Typically. in order to position a *small* spatial filter at the proper quadrature point, one must apply a small signal sinusoidal disturbance to the sensor via a piezoelectric device and use linear positioners to move the spatial filter until one locates the position of the pattern that gives the largest amplitude and least distorted sinusoidal signal at the output of the photodetection circuit, as displayed on, say, an oscilloscope. Note that the spatial filter *must* be placed between the output end of the fiber sensor and the photodetector and *must* be small so that any intensity variation, which is a point function. can be accurately simulated and monitored. One may also set the quadrature point by aligning the spatial filter at the peak of a lobe and by then causing a static strain in the fiber, via some static strain control device, so that the pattern rotates until the quadrature point is properly aligned with the spatial filter The use of both of these techniques for setting the Q-point will be discussed in chapter 4.

It should be obvious now that the MDS/9-633 sensor has practical limitations. In addition, due to the expected ease of use of the MDS/9-850 sensor to be discussed in the next section, no analysis has been given for the injection conditions necessary for the rotating three lobe pattern to exist in a MDS/9-633 sensor Therefore, from this point on it will be assumed that if one wishes to use a MDS/9-633 sensor that a rotating three lobe pattern can be obtained and that there is available equipment which allows the quadrature point to be set. The results of equations (3.1 14) and (3.1.15) can then be used With this in mind the sensitivity of the MDS/9-633 sensor can now be addressed

Although in a typical measurement situation one would measure $\Delta \bar{\varepsilon}_f$ as a function of the change in voltage at the output of a photodetection circuit with respect to its Q-point value, we may still relate $\Delta \bar{\varepsilon}_f$ to the change in optical power through the spatial filter with respect to *its* Q-point value This is done simply by dividing the numerator and denominator of equation (3 1.14), say, by $\mathscr{R}R_L$, where $\mathscr{R}$ is the responsivity of the photodiode and R_L is the load resistance of the detection circuit This yields

$$\Delta \bar{\varepsilon}_f = \frac{\Delta P}{P_Q \, \Delta \beta \, L_f \, \alpha} \qquad \text{(3.1.16)}$$

By refering to Figure 4 we can see that $b_{11} = 0\,55$ and $b_{21} = 0\,22$. Using equations (2 2.9) and (2.2.10) and Figure 4 we can therefore find that $\Delta \beta$ for the

MDS/9-633 sensor is $\Delta \beta = 1.2 \times 10^3 \, m^{-1}$ when $V = 4.616$, $n_1 = 1.458$, $a = 4.5 \, \mu m$ and $\lambda_o = 633 \, nm$. In addition we will reasonably assume for our detection circuit that for *pin* diode detection the fiber gage length L_f is $0.5 \, m$, the bulk dark current I_d of the photodiode is approximately 1 nA, the detection bandwidth B is 1 Hz. the responsivity $\mathcal{R}$ of the photodiode is approximately 0.5 A/W at 633 nm, the operating temperature T is 300°K and the load resistance is $R_L = 10 \, k\Omega$. We further assume that the optical power through the spatial filter at quadrature is $P_Q = 1 \, \mu W$. Using these values we may calculate the minimum detectable change in optical power through the spatial filter using equation (2 3.10). We thus find

$$\Delta P_{min} = 3.8 \times 10^{-12} \, W$$

If we now substitute this value into equation (3 1.14) and assume $\alpha = 0.78$ as discussed in section 2 4 we find that a reasonable minimum detectable strain expected for a typical MDS/9-633 sensor is

$$\Delta \bar{\varepsilon}_{min} \cong 10^{-9} \, m/m$$

The MDS/9-633 sensor is thus seen to be a highly sensitive strain detector. It is not, however, as sensitive as say a Mach-Zehnder interferometer since modal domain sensors are based on differential modal phase modulation, whereas the interferometer is based on absolute phase modulation [2]. By sacrificing some sensitivity, though the modal domain sensor will likely gain

increased stability and immunity to environmental noise over the interferometer, making modal domain sensors, in general, a more practical approach to strain detection in many real world situations.

3.2 The MDS/9-850 Sensor

Similar to the MDS/9-633 sensor, it has been observed that when 850 nm light from a semiconductor laser diode is injected into a 9 μm core diameter fiber a symmetric two lobe pattern can be created at the fiber output which oscillates as a function of axial strain Considering the same fiber as discussed in section (3.1) we see that the normalized frequency at $\lambda_3 = 850\ nm$ is

$$V = 2\,405\,\frac{1215\ nm}{850\ nm} = 3\,44\quad.$$

From Figure 4 we find that this allows for the propagation of only the LP_{01} and LP_{11} modes, including all degeneracies   We will now show for the case of x-polarized injection that the oscillatory two lobe pattern is caused by the interference of the LP_{01} and even LP_{11} modes

From equation (2.2.4) we see that the electric fields in the fiber core of the x-polarized LP_{01} and even LP_{11} are, respectively

$$\bar{E}_{01} = A_1 J_0(U_{01}r/a) e^{-j(\beta_{01}z - \psi_{01})} \hat{a}_x \qquad (3\ 2\ 1)$$

and

$$\bar{E}_{11} = A_2 J_1(U_{11}r/a) \cos \phi\, e^{-j(\beta_{11}z - \psi_{11})} \hat{a}_x \qquad (3\ 2\ 2)$$

Using equation (3.1.2) we can find the intensity distribution created by the interference of these modes to be

$$I = I_0 \left(A_1^2 J_0^2\left(\frac{U_{01}r}{a} \right) + A_2^2 J_1^2\left(\frac{U_{11}r}{a} \right) \cos^2\varphi \right.$$
$$\left. + 2A_1 A_2 J_0\left(\frac{U_{01}r}{a} \right) J_1\left(\frac{U_{11}r}{a} \right) \cos(\Delta\beta z - \Delta\psi) \cos\varphi \right). \qquad (3\ 2\ 3)$$

In equation (3 2 3) $\Delta\beta = \beta_{01} - \beta_{11}$, $\Delta\psi = \psi_{01} - \psi_{11}$ and $I_0 = Y_1/2$. In addition, from Figure 4 we can find that $b_{01} = 0.730$ and $b_{11} = 0\ 325$, so that if equations (2 2.9) and (2 2 10) and Figure 4 are used with $V = 3.44$, $n_1 = 1.458$, $a = 4\ 5\ \mu m$ and $\lambda_c = 850\ nm$ we calculate $\Delta\beta$ to be $\Delta\beta = 1.1 \times 10^3\ m^{-1}$.

Note that in equation (3 2.2) the first term is the intensity of the LP_{01} mode alone and the second term is the intensity of the LP_{11} mode alone while the third term arises due to the interference of the LP_{01} and LP_{11} modes. For discussion purposes let us rewrite equation (3.2.3) as

$$I = I_0\{I_1(r) + I_2(r,\phi) + I_3(r,\phi,z)\} \quad . \tag{3 2 4}$$

Notice that $I_1(r)$ is azimuthally symmetric while $I_2(r,\phi)$ has a maximum at $\phi = 0$ and $\phi = \pi$. The third term $I_3(r,\phi,z)$ also has a maximum at $\phi = 0$ but has a minimum at $\phi = \pi$. In addition $I_3(r,\phi,z)$ is modified by the $\cos(\Delta\beta z - \Delta\psi)$ term which varies between -1 and +1 as z is varied. Thus we can see that for proper choices of A_1 and A_2 we should expect to see an output intensity pattern consisting of two lobes, one of which gets brighter as z varies, while the other gets dimmer. Figures 16-22 help visualize this behavior. Figures 16 and 17 show the intensity distributions of $I_1(r)$ and $I_2(r,\phi)$, respectively, while Figure 18 shows a sketch of the LP_{11} mode, which is similar in the coordinate ϕ to the output of the MDS/9-850 sensor at quadrature. Figure 19 shows $I_1(r) + I_2(r,\phi)$ when $I_3(r,\phi,z) = 0$, while Figure 20 shows $I_3(r,\phi,z)$ at a maximum. Finally, Figure 21 shows the entire intensity distribution of equation (3 2.4) when $I_3(r,\phi,z)$ is a maximum, with Figure 22 being a three dimensional plot of $I_1(r) + I_2(r,\phi)$ when $I_3(r,\phi,z) = 0$. In these figures it is assumed that $A_1 = 2A_2$, with all but Figure 18 showing plots normalized to $I_1(r)$ having a maximum intensity of unity. The choices of A_1 and A_2 are somewhat arbitrary and give indications as to the ratio of the input power existing in each mode. Here the choice of $A_2 = 2A_1$ was done to enhance the visualization of the behavior of the two lobes as a function of strain, which has been observed. This choice was made after evaluating

several plots of equation (3 2 3), with the amplitude coefficients taken as parameters   With $A_2 \cong 2A_1$, it was seen that the calculated output intensity distribution of the MDS/9-850 sensor most closely agrees with experimental observation   One must realize, however, that the ratio A_2/A_1 will be determined by source input conditions and must be some moderate value greater than one   If A_2/A_1 is less than unity the LP_{21} mode will dominate and only a single lobe will present at the output. If A_2/A_1 is much greater than unity only negligible power will exist in the LP_{01} mode and thus no interference will take place   For convenience we will proceed under the assumption that $A_2 \cong 2A_1$

Some further comments concerning Figures 16-22 should be made. First, it should be noted that all line graphs are plotted in the plane where $I_1(r)$, $I_2(r, \phi)$ and $I_3(r, \phi, z)$ have maxima. Second, all the units of the spa' dimensions in Figures 16-22 are in microns. Third, the 3-D plot in Figure 22 is only valid in the region where $r = \sqrt{x^2 + y^2} \leq 4.5\,\mu m$ And finally, the sketches of Figure 18 are included to give a better visualization as to how the pattern caused by LP_{01} and LP_{11} modal interference will appear as seen looking toward the fiber end face   As with similar plots in earlier sections, these plots, with the exception of Figure 18, were generated with aid of the material in both Append.x C and Appendix D.

At this point it should be easily seen how this modal interference phenomena can be used as a sensor mechanism. If one adjusts the input conditions in such a way that $I_3(r, \phi, z)$ is zero at the fiber output end face, a maximum sensitivity quadrature point will have been created. If one then monitors one of the peaks at this quadrature point by spatially filtering out all but a small portion of the output pattern at this peak, a change in optical power through the aperture of the spatial filter will be directly related to any perturbations in the fiber.

Notice now that in Figure 21 if we monitor the peak of a lobe, then a maximum intensity at some amount of strain will occur at $r \cong 2.38\ um$ in the maximum intensity plane. If we choose the lobe at say $\phi = 0$ and if it can be shown that

$$J_0^2\left(\frac{U_{01}r}{a}\right) + 4J_1^2\left(\frac{U_{11}r}{a}\right) \cong 4J_0\left(\frac{U_{01}r}{a}\right)J_1\left(\frac{U_{11}r}{a}\right) \qquad (3.2.5)$$

at $r \cong 2.38\ \mu m$, for $A_2 \cong 2A_1$, then we can obtain the reduced form for the core field intensity, equation (3.2.3), as

$$I = I'_0\{1 + \cos(\Delta\beta z - \Delta\psi)\}$$

or

$$I = I_p \cos^2\left(\frac{\Delta\beta z - \Delta\psi}{2}\right) , \qquad (3.2.6)$$

where I'_0 has incorporated into it the terms of equation (3 2 5) after being factored from equation (3 2.3) and where $I_p = 2I'_3$ represents the peak intensity of a lobe. Indeed, by recalling the fiber parameters and using Figure 3 we can show for $r \cong 2.38\ um$ that the quantities of equation (3 2 5) are the same to within 4 8 percent. with $A_2 \cong 2A_1$, so that the above simplification of the core intensity function is valid in the region of a lobe peak at either $\varphi = 0$ or $o = \pi$ The only difference. recall. in these two lobes is that one will increase in intensity while the other decreases for small amounts of strain. Also, since the peaks of $I_2(r, o)$, $I_3(r, \phi, z)$ and $I_1(r) + I_2(r, \varphi, z)$ don't precisely align with one another. with the peak radius of $I_2(r, o)$ being the largest, it is expected that the above simplification of the core intensity function should be valid for reasonable ratios of $A_2/A_1 > 2$ in the regions of the lobe peaks at $\varphi = 0$ and $\phi = \pi$. Therefore from now on it will be assumed that we are discussing a sensor system in which the input has been adjusted so that two lobes of equal intensity are observed at the output under a no strain situation Further, it will be assumed that the ratio A_2/A_1 is some reasonable value so that the interference takes place and that in the region about the peaks of the lobes the intensity can be approximated by equation (3.2.6).

We recall that by using equation (2.4.6), we can include in equation (3.2.6) the photoelastic effects of the fiber under strain, at the radial coordinate of a lobe peak, to give

$$I = I_p \cos^2\left(\frac{\Delta\beta\, \varepsilon_z L_f x + \phi_o}{2} \right) , \qquad (3\,2.7)$$

where $\phi_o = -\pi/2$ if we consider that we are monitoring the lobe which increases with strain from $I = I_{\cdot}/2$ under a no strain situation. We recall that at quadrature $I_3(r, \varphi\ z) = 0$ and we have two lobes of equal intensity, one of which increases while the other decreases as a function fo strain. Using the same arguments as were used to arrive at the results of equations (3 1 14) and (3.1.15), we can show for small changes of strain, as averaged over the gage length of the sensing fiber, that $\Delta\bar{\varepsilon}_f$ can be measured from quadrature with the MDS/9-850 sensor as

$$\Delta\bar{\varepsilon}_f = \frac{\Delta V}{V_Q(\Delta\beta\, L_f x)} , \qquad (3\,2\,8)$$

for the case of static strain and

$$\Delta\bar{\varepsilon}_f = \frac{\Delta V_{peak}\cos(\omega t)}{V_Q\, (\Delta\beta\, L_f x)} , \qquad (3.2.9)$$

for the case of small amplitude time harmonic strain and small peak displacement vibrational strain. Note the similarity of these results (only $\Delta\beta$ takes on a different value) and those of equations (3.1.14) a:jd (3.1.15) even though the sensing techniques are rather different   The sensitivities of the

MDS/9-850 and MDS/9-633 sensors are also comparable and equations (3.2 8) and (3.2 9) may be used to detect $\pm \Delta\varepsilon_r$ from quadrature if there is an initial strain in the fiber

As expected, using a laser diode in a modal domain sensor provides several advantages. First, due to the fundamental mode (LP_{01}) not needing to be extinguished for proper sensor operation, it is much easier to align the input. Also, since information will be taken from the sensor by monitoring the intensity variations of a lobe peak, alignment of the Q-point of the sensor is expected to be relatively simple. In addition, laser diodes are light weight, physically small and it is possible to find highly linearly polarized laser diodes operating at $\lambda_o = 780$ nm that are relatively inexpensive

Although the preceding analysis has been for $\lambda = 850$ nm, it is still valid for any source wavelength such that $V < 3.8$ so that the LP_{21} mode is still cutoff. For $\lambda_o = 780$ nm, $V = 3\,75$ In addition, for $\lambda_o = 780$ nm, $\Delta\beta \cong 1\,1 \times 10^4\,m^{-1}$ as with 850 nm injection so that sensitivity is preserved.

The only apparent drawback to using laser diodes as sources is that they require special viewing equipment to observe the infrared radiation. This problem may, however, be overcome through the use of small, light weight in-line detection techniques presently under investigation. And finally, as laser diodes may be operated in a pulsed fashion, it may be possible to

simulate the use of a beam chopper in a detection system so that signal-to-noise ratio may be preserved for low frequency noise as would be present if there was, say, excess thermal drift.
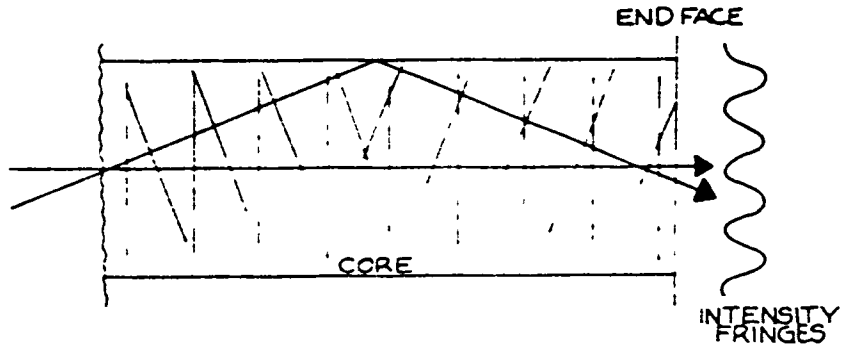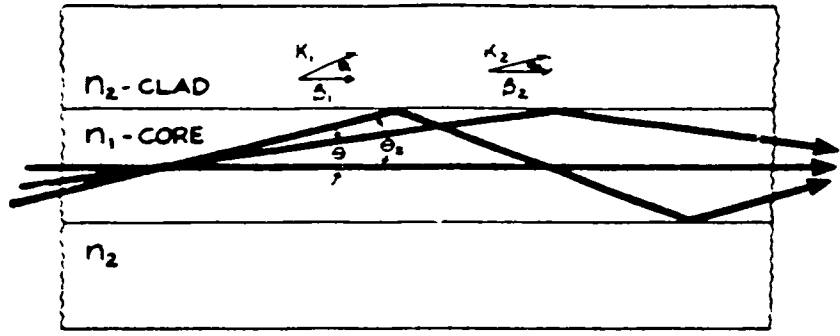
Figure 10   A simplistic look at modal interference

CUTOFF PLOT   TYPE. BEND
ID:VPI TEST 2 TRICK FIBER 28-JAN-87 13:58:53

Cutoff Wavelength=1215.1
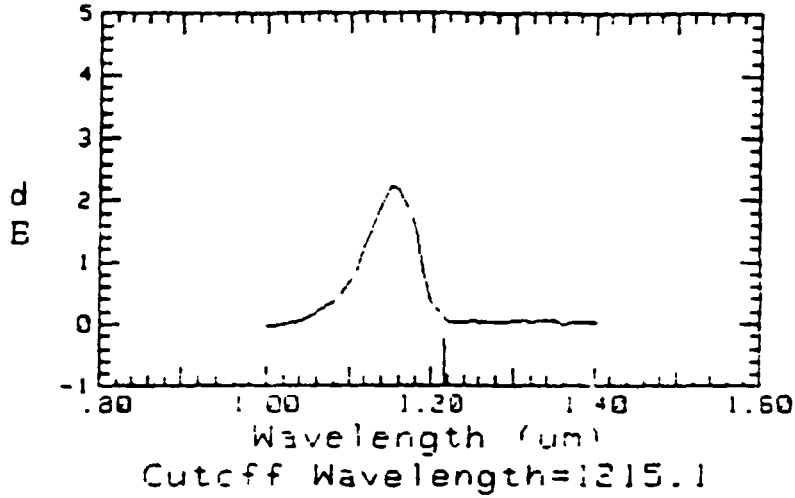
VARIABLE APERTURE PATTERN AT 1300 nm
ID: VPI TRICK FIBER 28-JAN-87 11:55:15

Mode Field Diameter=11.1472
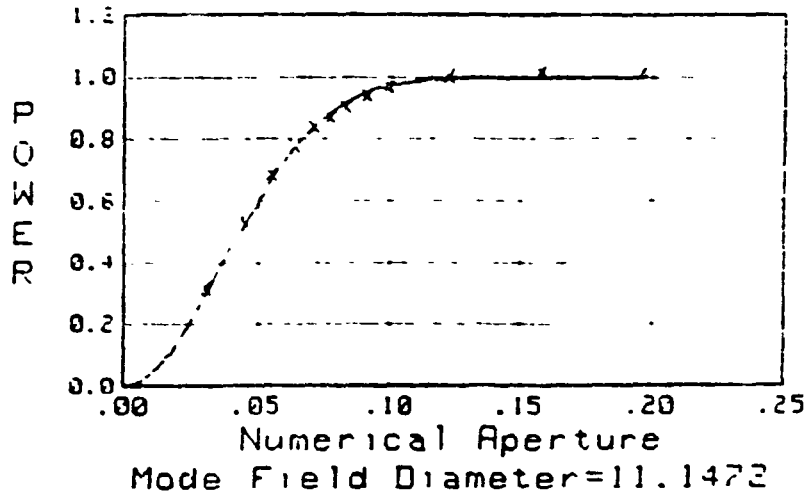
Figure 11.   FOA-2000 fiber optic analyzer data

3.0 MODAL DOMAIN SENSING
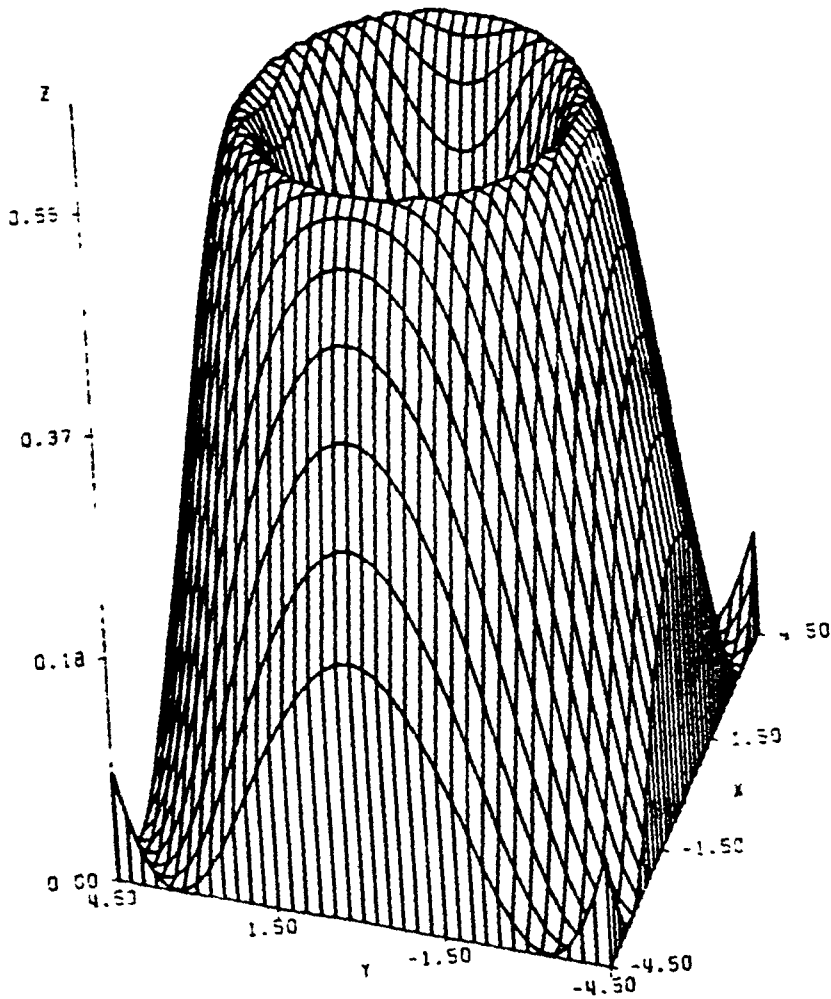
Figure 12. The MDS/9-633 background intensity term

3 0 MODAL DOMAIN SENSING
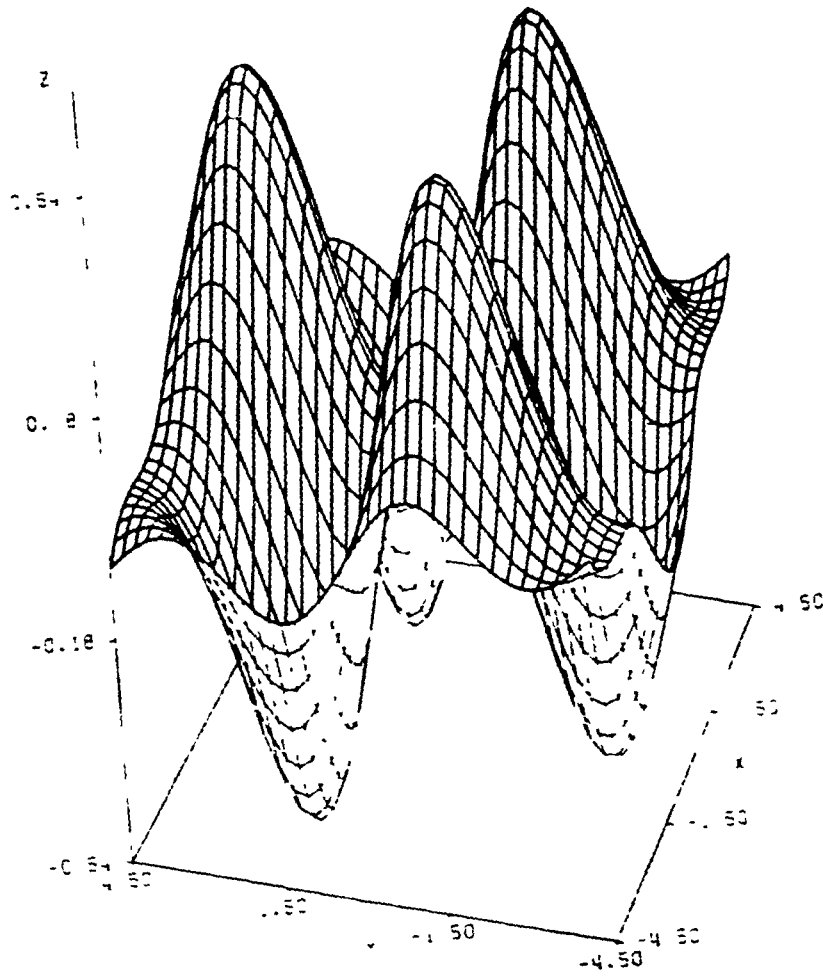
Figure 13. The MDS/9-633 strain modulated intensity term

3 0 MODAL DOMAIN SENSING
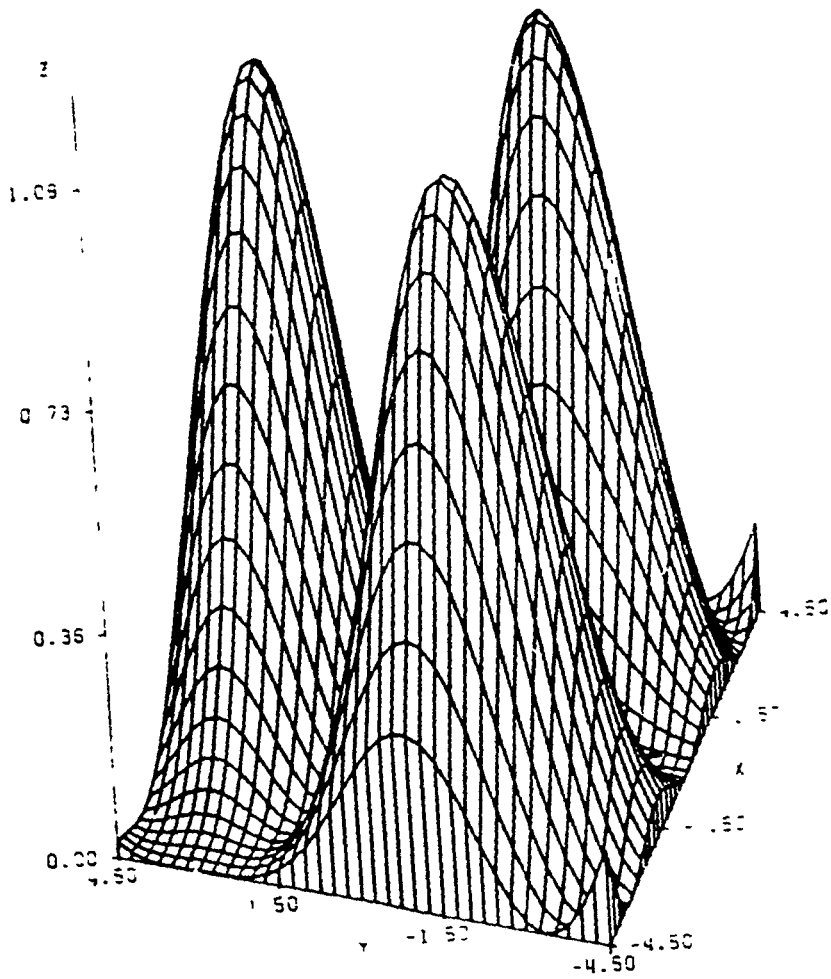
Figure 14. The total MDS/9-633 output intensity distribution

3 0 MODAL DOMAIN SENSING

(a)

ROTATION

INTENSITY NULL

SPATIALLY FILTERED REGION AT Q POINT

HALF INTENSITY

(b)
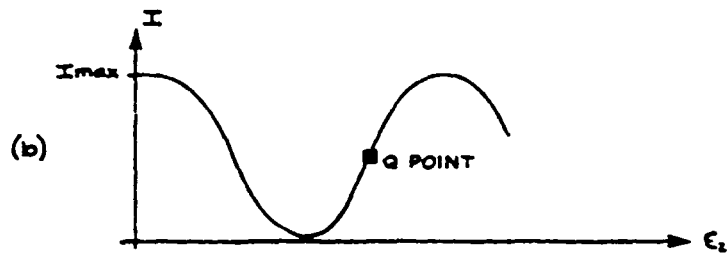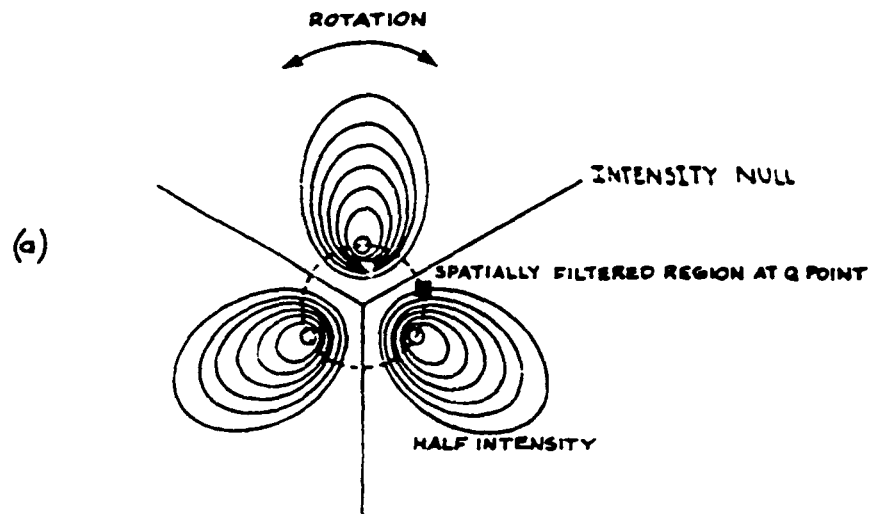
Figure 15. Axial view of the MDS/9-633 Intensity distribution
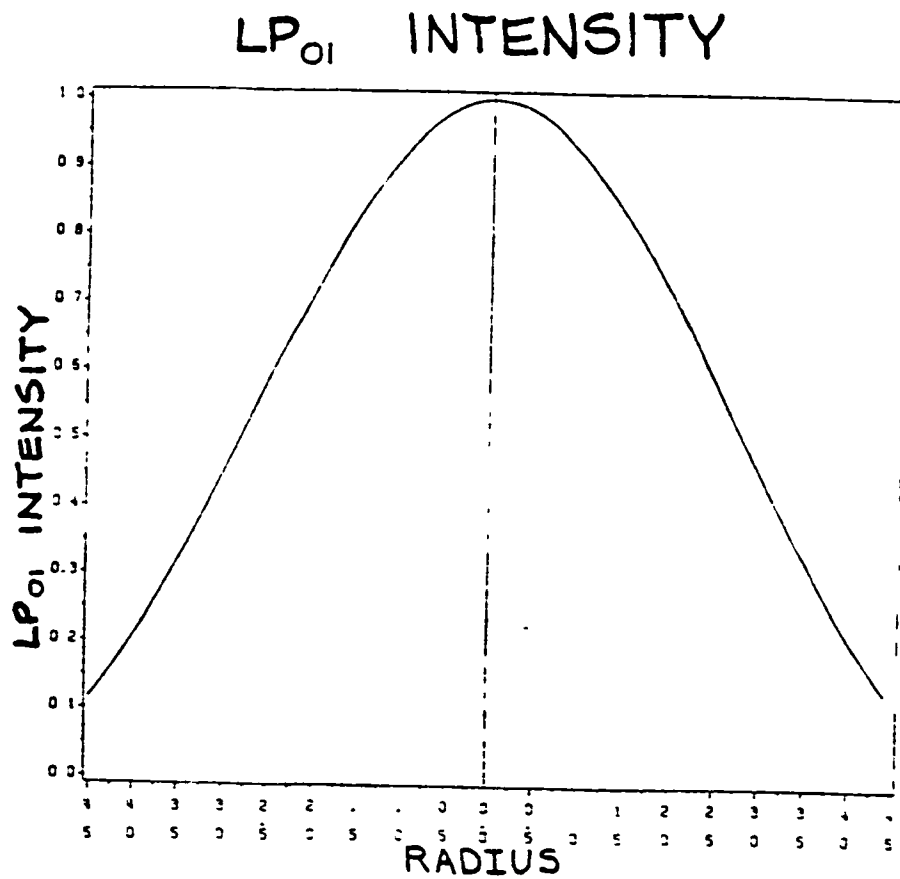
Figure 16. The LP_{01} mode intensity distribution of the MDS/9-850 sensor

3 0 MODAL DOMAIN SENSING

64
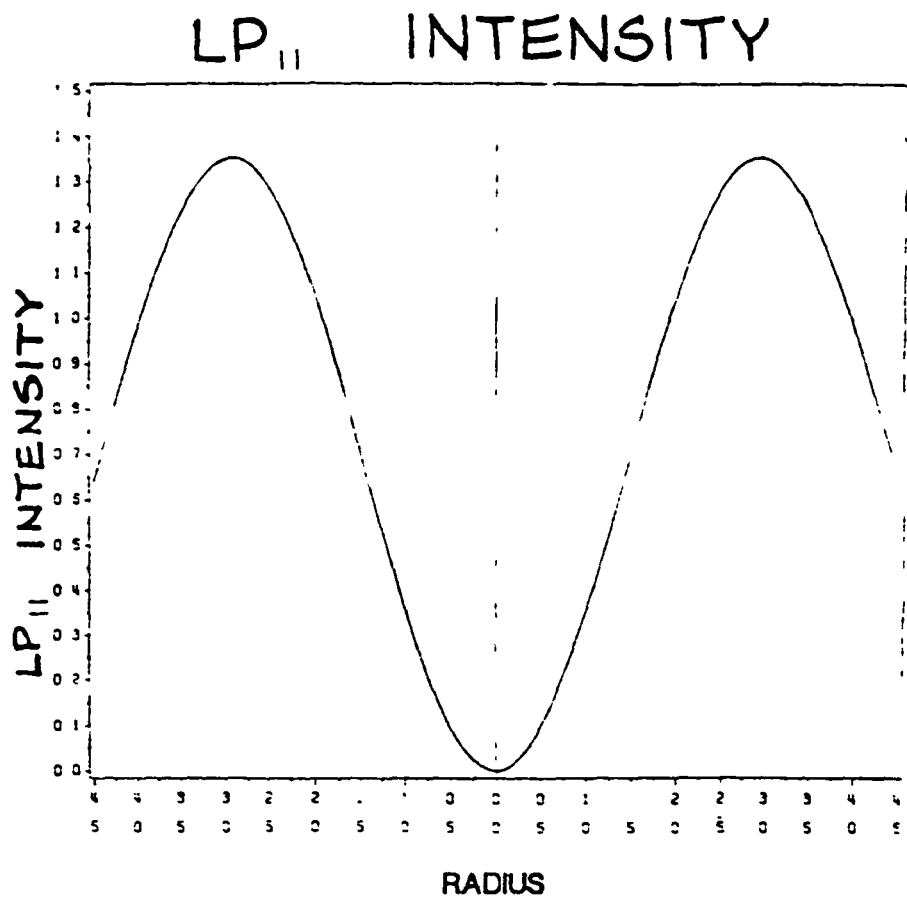
Figure 17. The LP_{11} mode intensity distribution of the MDS/9-850 sensor

3 0 MODAL DOMAIN SENSING

LP$_{11}$ MODE INTENSITY PATTERN

V = 3.4377
9/125 μm FIBER
n_1 = 1.458
b = 325
NA = 1

$I_2 = A_2^2 \, J_1^2 (vr/a) \cos^2 \phi \quad r < a$

$r_p \cdot -3$ μm

a = 4.5 μm

NOTE

$\dfrac{I_{max}}{2}$ at ~ r = a
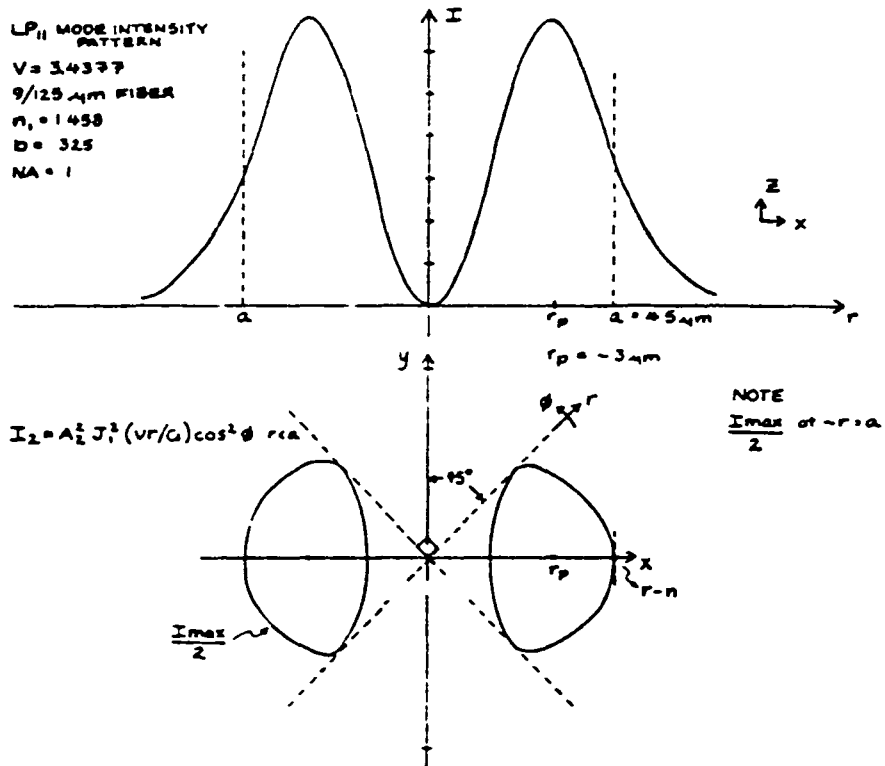
Figure 18. The LP$_{11}$ mode intensity pattern

LP$_{01}$ +LP$_{11}$ INTENSITY
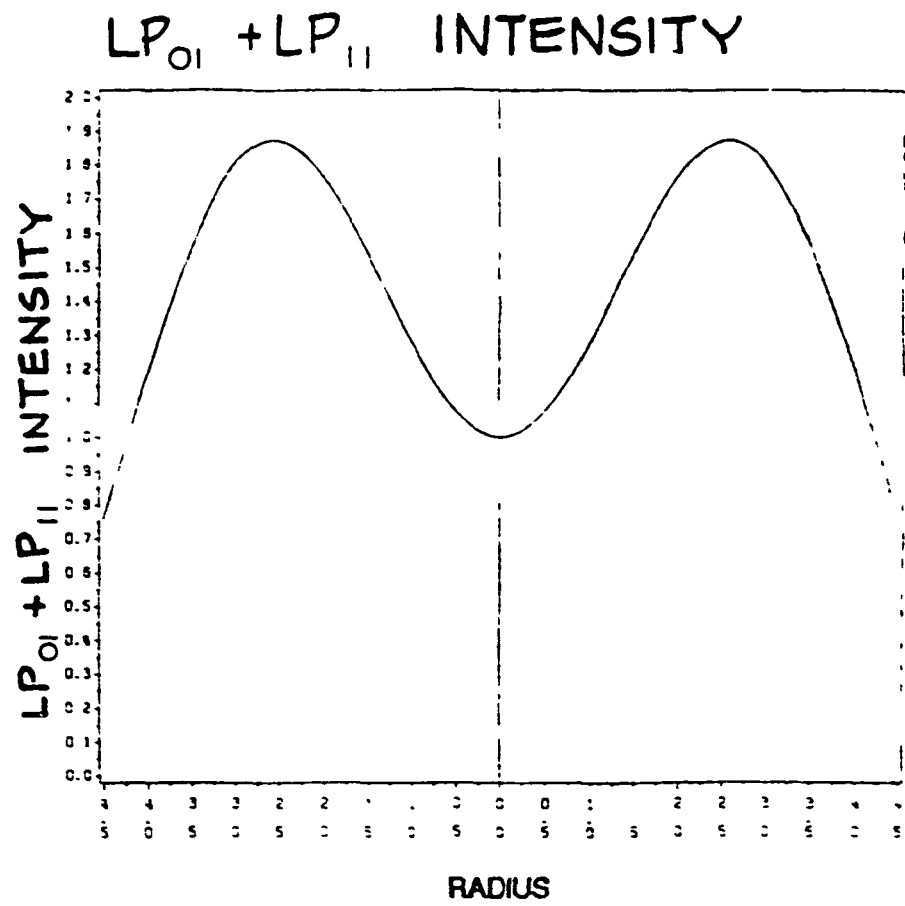
Figure 19.   MDS/9-850 intensity variation of $I_1(r) + I_2(r, \phi)$, at quadrature
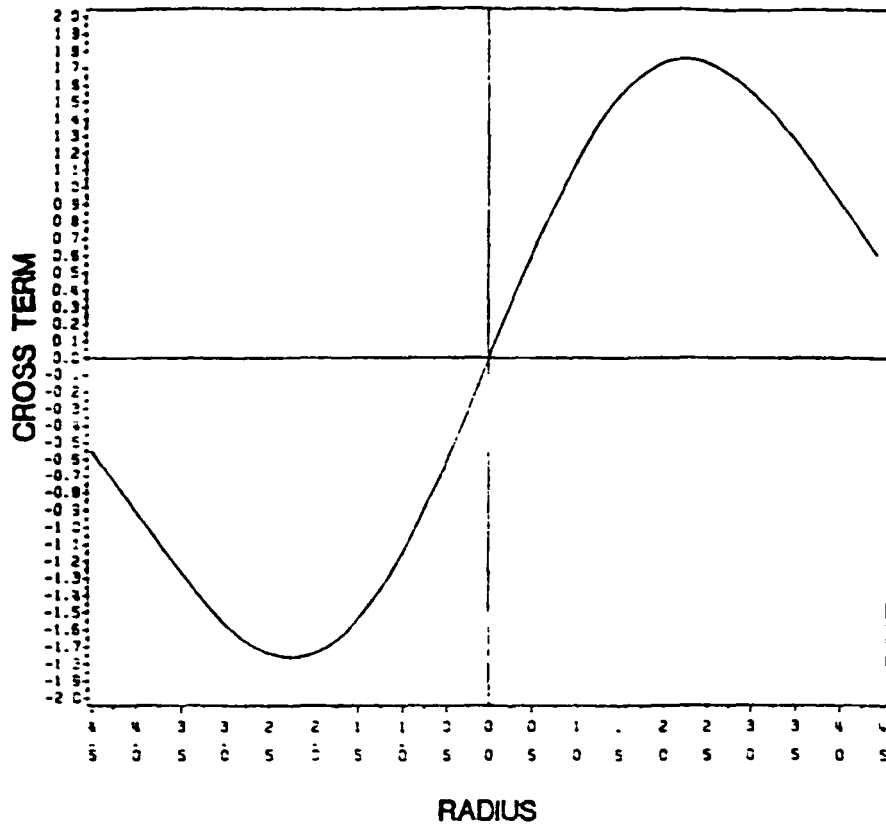
CROSS TERM

Figure 20. Intensity variation of the MDS/9-850 cross term $I_x(r,\phi,z)$, at a maximum

TOTAL INTENSITY
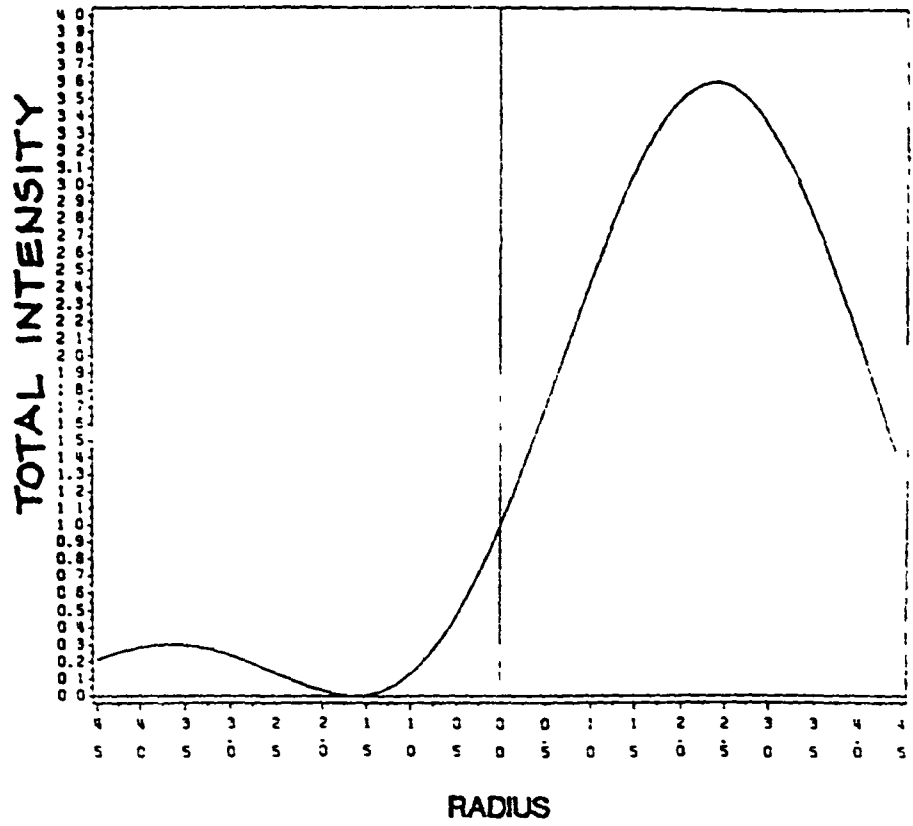
Figure 21. Total intensity pattern of the MDS/9-850 output when $I_s(r,\phi,z)$ is maximum
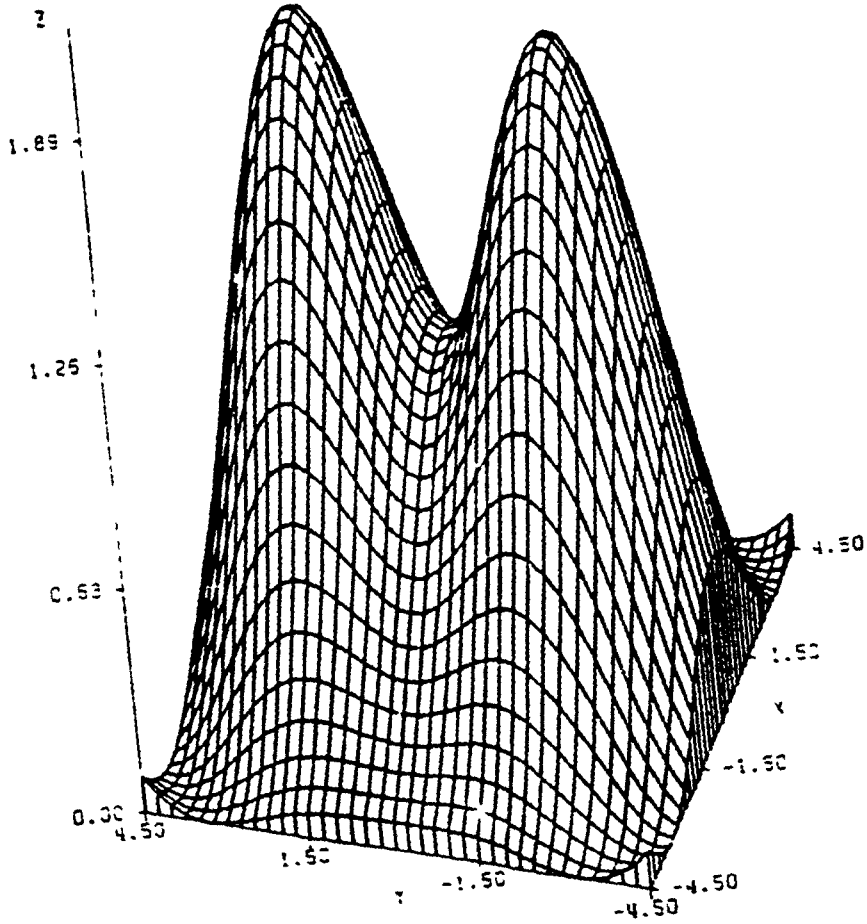
Figure 22. The MDS/9-850 intensity distribution at quadrature (3-D)

70

3 0 MODAL DOMAIN SENSING

4.0 MDS/9-633 SENSOR EVALUATION

Although an MDS/9-633 sensor system will have practical limitations, it is easy to construct a working sensor system based of the MDS/9-633 technique using readily available optical laboratory equipment. In addition, by evaluating the MDS/9-633 sensor one can obtain insight about the practical aspects and performance characteristics of modal domain sensors in general. We begin with a description of the experimental system used to evaluate the MDS/9-633 sensor technique.

The experimental setup is shown diagrammatically in Figure 23. As seen, the emission from a He-Ne gas laser is focused through a microscope objective onto the end face of a $9\mu m$ core diameter fiber held in a fiber positioner. This fiber is of the same characteristics as the fiber discussed in section 3.1 and is attached in sequence to a static strain control device, a piezoelectric PZT

cylinder, a cantilever beam and a holding post at the output. The static strain control device simply consists of two plastic disks on which the fiber is wound, one of which has an attached push rod and is mounted on a rotateable base. As seen in Figure 24, tension is applied to the fiber between the two disks as force is placed on the push rod via a micrometer screw. In addition, so as to avoid appreciable bend loss in the fiber, the radius of the disks was approximately three inches

The PZT cylinder following the static strain control device had wound upon it several turns of the 9 μm core diameter fiber and obtained its excitation from an external signal generator. As with the static strain control device, the purpose of the PZT cylinder was to aid in aligning the system quadrature point. For reasons to be discussed later, however, only the PZT cylinder was able to help achieve this goal.

After the PZT cylinder, the fiber was attached, along with a resistive strain gage, to a cantilever beam. Appendix A presents a detailed analysis of the strain characteristics of a loaded cantilever beam, as well as a discussion of the geometry of the fiber path on the beam necessary so that the strain induced in the optical fiber is identical to that induced in a resistive strain gage placed at the geometric center of the beam surface. The reader is encouraged

to review Appendix A before proceeding. Referring to Appendix A, the dimensions of the cantilever beam and the optical fiber path were chosen as

$$L = 0\,288\,m$$
$$L_1 = 0\,0254\,m$$
$$b = 0\,071\,m$$
$$h = 0\,0022\,m$$
$$r = 0\,0159\,m$$

where L is the beam length, $L-L_1$ is the length of the straight fiber segment and r is the radius of the curved portion of the fiber, with b and h being the beam width and thickness, respectively. With this geometry the change in average strain induced in both the optical fiber and the resistive strain gage is given as a function of load by

$$\Delta\bar{\varepsilon} = \frac{3mgL}{Ebh^2} \quad , \tag{4.0 1}$$

as shown in Appendix A, where m is the change in initial load mass and g is the acceleration due to gravity. Young's modulus E for the beam depends on the beam material and as our beam was constructed of alumin $E = 6\,9\times10^{10}\,Pa$. In addition, for this beam the Poisson's ratio is $v = 0.33$, while the gage length of the fiber on the beam is

$$L_f = 2(L - L_1) + \pi r = 0.575\,m \quad .$$

Further, the optical fiber was mounted to the beam unstripped to prevent breaking and both the fiber and resistive strain gage were bonded to the beam using thermal-set epoxy

The output end of the fiber sensor was attached to a holding post positioned a few centimeters from the photodetection circuit. The detection circuit consisted simply of a photodiode, reverse biased at nine volts, mounted on an x-y-z positioning stage. Load resistance was provided via a decade box. In addition, epoxied to the front of the photodiode (UDT model PIN-10D) was an iris which served as a spatial filtering device. Fully open the iris was 1 2 cm in diameter and when closed a 1.0 mm aperture remained. Typically, spatial filtering was done with the iris closed; however. the actual size of the spatial filter aperture is mostly irrelevant as long as it is small with. respect to th_ output intensity distribution being monitored.

Not shown is the Wheatstone bridge and amplifier circuit used to detect small changes in resistance of the resistive strain gage. The output of this circuit and the photodetector were both connected in parallel to a digital voltmeter an oscilloscope and a spectrum analyzer for data collection purposes. addition, the entire system, except for measurement equipment, was mounted. to a floating (pneumatically supported) optical table.

Finally, throughout the discussions to follow no account will be given to any system noise arising from sources other than the photodetection circuit and its associated load resistor In addition, it will be assumed that the bonding of both the optical fiber and the resistive strain gage to the cantilever beam is perfect with no shearing of the fiber jacket occuring as strain is applied These assumptions will not likely be valid outside of a laboratory environment

4.1 Resistive Strain Gage Evaluation

As the resistive strain gage is a commonly used and well accepted instrument for measuring strain it was decided that a resistive strain gage would be used as a standard with which to compare the performance of the MDS/9-633 sensor. It was therefore important to evaluate the performance of the resistive strain gage used in our sensor system prior to all other measurements. As mentioned previously, the resistive strain gage was placed at the geometric center of the cantilever beam surface, so that as a function of load, the inc. strain characteristics of the gage follow equation (4 0.1). In addition, as shown in Appendix B, the change in average strain in the beam as *measured* by the resistive strain gage is given by

$$\Delta\bar{\varepsilon} = \frac{-V_{out}}{V_{in}} \frac{4R_5}{S_g R_6} \left[\frac{1 - k_t v_0}{1 - k_t v} \right] . \qquad (4\ 1\ 1)$$

where V_{out} is the negative voltage measured (for positive strain) at the output of the inverting amplifier following the Wheatstone bridge circuit. The bridge, recall is used to allow small changes in strain to be detected. In addition the input V_{in} to the bridge circuit, as supplied by a regulated power supply, was measured to be 10 0 V, while the gain of the amplifier was measured to be $|R_6/R_5| = 179.78$. Individual values of R_5 and R_6 were measured to be 102 834 MΩ and 572 0 kΩ, respectively. These measurements and other similar ones to be presented later were made on a Solartron model 7061 digital voltmeter that was capable of displaying seven significant digits.

The specific resistive strain gage used was manufactured by Micro-measurements Corporation and had a nominal resistance R_0 of 120.0 $\pm$ 0 18 Ω. In addition, the gage factor S_g was given as 2 095 $\pm$ 05 at 300°K while the transverse sensitivity factor k_t was given as $k_t = 0.006$. Finally u Poisson's ratios in equation (4.1.1) are given as $v_0 = 0.285$ and $v = 0.33$ and represent the Poisson's ratios of the factory gage calibration beam and the aluminum experimental test beam, respectively Refer to Appendix B for further details.

In order to evaluate our resistive strain gage, the beam was initally loaded with a 200 gram mass using the loading technique depicted in Figure 25(b). This was done to take any "slack" out of the system. The gage resistance was then measured and the other resistances of the bridge circuit adjusted (trimpots were used) so as to null the output. Additional load mass was then added to the beam with readings of V_{out} being taken as the excess load mass reached the values of 5, 10, 20, 30, 40, 50 and 100 grams. This procedure was repeated several times and a representative plot of data depicting the measured versus induced change in average beam strain is given in Figure 26. In particular, note the regression polynomial calculated for this data. As is seen, the calculated slope of the line deviates only slightly from the case of unity slope. In addition, the y-axis crossing value can be shown to very closely correspond to the measurement uncertainty of the resistive strain gage.

If we now conservatively assume that our Solartron volt/ohm meter is uncertain to within plus or minus one digit in the fourth decimal place (for a given scale factor) we may calculate our minimum change in ε measurable with the resistive strain gage using the procedure outlined in Appendix B. With $dV_{out} = \pm 10^{-4}\,V$, $V_{in} = 10.0 \pm 10^{-4}\,V$, $R_s = 572.0 \pm 10^{-4}\,k\Omega$ and $R_g = 102.834 \pm 10^{-4}\,M\Omega$ we find that our minimum detectable change in average beam strain is $\Delta\bar{\varepsilon}_{min} = 0.21\,\mu m/m$, as measured with the resistive

strain gage. As this value also represents twice the absolute measurement uncertainty of the resistive strain gage (even with no applied load) it is seen that the y-axis crossing of the regression polynomial of Figure 26 very closely matches with the predicted value. We therefore see that our resistive strain gage provides a justifiable strain measurement standard.

4.2 Dynamic Strain Measurements

With confidence now gained in the performance of the resistive strain gage, the next task was to investigate the performance of the MDS/9-633 sensor. A discussion will be given in this section relating to the modal domain sensor's abilities to serve as a dynamic strain measurement device. Sections 4.4 ar 4 5 will discuss static strain measurements.

Dynamic strain was induced in the cantilever beam using a setup as shown in Figure 25(a). As is seen, the action of the vibration exciter (Brüel & Kjær type 4809) was transmitted to the beam via a push rod. The ball and socket joint was used so that the deflecting force on the beam remained normal to the surface and so that the shaft of the vibration exciter was not subjected to any off axis stress. Notice, however, that this setup does not provide a way by which the force on the beam or the beam tip deflection can be measured as it

vibrates. All is known is that the beam can be caused to vibrate at the frequency of the signal input to the vibration exciter and that the amplitude of this vibration may be varied (in an uncalibrated way) by adjusting the input signal amplitude. For this reason it was important that the resistive strain gage behave properly so that the MDS/9-633 sensor readings could be compared to a reliable standard.

It was decided that as the beam vibrated the amplitude of the sinusoidally varying average beam strain, or peak average strain, would be the quantity to be measured. For the modal domain sensor, we have from section 3.1 that the measured peak average strain is given as

$$\bar{\varepsilon}_{f\,peak} = \frac{V_{peak}}{V_Q\,(\Delta\beta\,L_f\,\alpha)} \quad . \tag{4.2.1}$$

For the resistive strain gage we have from Appendix B that this same quantity is measured as

$$\bar{\varepsilon}_{RSG\,peak} = \frac{V_p}{V_{in}}\;\frac{4R_5}{S_g R_6}\left[\frac{1 - k_t v_0}{1 - k_t v}\right] \quad . \tag{4.2.2}$$

Note that in equations (4.2.1) and (4.2.2) we are considering that the beam is initially unloaded and that V_{peak} and V_p correspond to the amplitudes of the

sinusoidal signals generated at the output of the MDS/9-633 and resistive strain gage sensors, respectively

To avoid both resonance conditions and damping of the vibration induced into the cantilever beam it was decided that the beam would be excited at as far below its fundamental frequency of vibration as possible. This frequency was determined by plucking the beam and allowing it to vibrate freely (with the push rod removed) and by then monitoring the output of the resistive strain gage sensor on a spectrum analyzer. As seen in Figure 27 the fundamental frequency of vibration was measured to be 21.6 Hz. Since the vibration exciter could not be reliably operated below 10 Hz this was chosen as the excitation frequency for dynamic strain measurements

To conduct the experiment the fiber launch conditions were adjusted until a rotating three lobe pattern was observed. This was often facilitated ⌄, adjusting the tension in the length of fiber between the spools of the static strain control device, although no good explanation for this effect presently exists. The photodetector was then typically moved toward the fiber till the pattern just filled the open iris (a somewhat arbitrary act) and the Q-point was set using the PZT cylinder.

It was observed that when the PZT cylinder was excited at its resonance frequency of 38.5 kHz an appreciable small signal sinusoidal strain could be

imparted to the fiber, causing a small sinusoidal response at the photodetector output. The Q-point of the system was then set by using an x-y positioner to position the closed iris over the point of the pattern that gave the highest amplitude and least distorted sinusoidal response. This proved to be the most reliable way of setting the quadrature point and Figure 28 shows a highly aligned MDS/9-633 output signal observed during such an alignment. The top trace is the modal domain signal and has a peak-to-peak voltage of 80 mV. The bottom trace is the input to the PZT cylinder and has a peak-to-peak voltage of five volts. Both traces are at 38 5 kHz.

Conceivably, it should be possible to set the Q-point by locating the iris over the peak of a lobe and causing a static strain in the fiber so as to cause the pattern to rotate to the point where the iris is located half way between the maximum and minimum of a lobe. In practice this proved to be difficult, though, as it was often difficult to align the input in such a way that the three lobe pattern rotated properly through more than about twenty to thirty degrees. This was fine for small signal work but made alignment of the Q-point difficult using the "bulk effect" technique just described. Therefore only the "small signal" method of setting the Q-point, using the excited PZT cylinder, was used.

With the Q-point properly set. data was taken by recording the peak voltage out of each of the sensors on the cantilever beam, for varying amplitudes of the signal input to the vibration exciter, at the 10 Hz peak observed on a Spectrum analyzer. Recall that for all dynamic measurements the beam excitation is at 10 Hz. Plots of some of this data. converted to strain measurements using equations (4 2.1) and (4.2.2) are given in Figures 29, 30 and 35 with several polaroid photos corresponding to the data of Figure 30 being shown in Figures 31-34. These shall be discussed shortly.

For the data of Figures 29, 30, and 35, the load resistance was 50 kΩ and the input to the Wheatstone bridge V_n was taken from a nine volt battery. The value of α was taken to be $x = 0.78$ in equations (4.2.1) and (4.2.2). as per the discussion of section 2.4, although this value will be seen to change when static strain measurements are undertaken. Recall also that $\Delta\beta = 1.2\text{x}10^4 \, m^{-1}$ for the MDS/9-633 sensor. In addition, so as to make the data sets independant, the pattern and quadrature point were readjusted before eacn set of data was collected. For the data sets of Figure 29, 30 and 35 the Q-point voltages V_0 for the MDS/9-633 sensor were 1.2 V, 0.55 V and 0.35 V, respectively. Since the sensitivity of the MDS/9-633 sensor directly depends on the Q-point value of optical power through the spatial filter aperture, it is easy to see why the y-axis crossing is at a much higher value of strain in Figure 35 than it is in Figure 29, Note, however, the linearity and near unity

slope of all data in Figures 29 30 and 35. Especially note that the y-axis crossings of the extrapolated data in each of these figures agrees well with the minimum expected detectable average beam strain calculated in section 3.1

Figure 31 shows a spectrum analyzer trace for both the MDS/9-633 sensor (top trace) and the resistive strain gage (bottom trace) at a point where the beam excitation is small. Note the output of each sensor is precisely at 10Hz and that the MDS/9-633 sensor has a much higher signal to noise ratio than the resistive strain gage sensor, thus indicating that the modal domain sensor w' be able to provide strain measurement data long after the resistive strain gage has reached its minimum. Also. the spectrum analyzer gave the amplitude of each detected signal in *dBV RMS* so that peak voltage was calculated using the conversion

$$V_p = \sqrt{2}\ 10^{\left(\frac{V_{dBV\ RMS}}{20}\right)} \ .\qquad(4.2.3)$$

Furthermore, the data of Figure 31 corresponds to the first blackened data point in Figure 30 and is seen to be at the low end of the usable range of the resistive strain gage. Similarly, the polaroids of Figure 32 correspond to the second blackened data point of Figure 30 and are the result of a larger beam excitation. All data shown in these photographs were averaged eight times for visual purposes only. Finally, Figures 33 and 34 show the vibration exciter input signal and the noise floors of the strain sensors at quadrature with no

excitation, respectively   The bottom trace in Figure 34 corresponds, at 10 Hz, to the noise (-104 5 dBV RMS) of the MDS/9-633 sensor, while the top trace corresponds to the noise (-86.0 dBV RMS) of the resistive strain gage sensor. Using equations (4.2.1), (4 2.2) and (4.2 3) it is easily seen that these noise figures correspond to minimum detectable average beam strains of $\bar{\varepsilon} = 2\ 8 \times 10^{-9}\ m/m$ and $\bar{\varepsilon} \cong 0.1 \times 10^{-6}\ m/m$ for the MDS/9-633 and resistive strain gage sensors. respectively. This is in very good agreement with the predicted minimum detectable strains for each sensor and lends validity to the assumption of negligible excess environmental noise.

There are two final comments to make before moving to the next section. First, it should be mentioned that the maximum tip deflection never exceeded more than a few millimeters for all dynamic measurements. Second, although no values for beam displacement have been given, this can be calculated if the average strain in the beam is known using the relation

$$d = \bar{\varepsilon}\frac{4L^2}{3h} \ ,$$
(4.2.4)

where d is the beam tip displacement from its undisturbed position, L is length of the cantilever beam and h is the beam thickness [1]. For the modal domain sensor, this gives us

$$d = \frac{V_{peak}}{V_Q \, \Delta\beta \, L_f \, x} \left(\frac{4L^2}{3h} \right) \, . \qquad (4.2.5)$$

where the beam is assumed to be initially unloaded.

4.3 Extraneous Dynamic Modulation

At this point it is reasonable to wonder if there are any effects other than rotation of the three lobe intensity distribution which give rise to the signals discussed in the previous section. In order to investigate this, a properly rotating three lobe pattern was obtained and the detector positioned, with the iris fully open, so that the pattern filled the area of the detector face. The b was then caused to vibrate at 10 Hz using the vibration exciter, with data taken as peak voltage readings at the output of both the photodetector and the resistive strain gage sensor circuits. Figure 36 shows this data taken for a series of varying signal amplitudes into the vibration exciter. The data is plotted as millivolts of extraneous modulation out of the photodetector versus resistive strain gage detected strain.

Figure 37 shows polaroid photos of the spectrum analyzer traces for large (top photo) and moderate (bottom photo) beam excitations. These correspond to

their respective blackened data points in Figure 36. Similarly, Figure 38 shows a polaroid photo of the spectrum analyzer trace for small beam excitation and corresponds to the blackened data point nearest the origin in Figure 36. For all photos in Figures 37 and 38 the top trace shows the output of the resistive strain gage sensor while the bottom trace shows the extraneous modulation output of the photodetector. Figure 39 shows the noise floors, with no excitation, for the measurements of extraneous modulation. Again, the top trace corresponds to the noise of the resistive strain gage (-88 dBV RMS) while the bottom trace corresponds to the noise of the photodetector output (-99.5 dBV RMS)

In a typical measurement situation, recall, the iris will be closed, leaving ˰˰ a 1.0 mm aperture. This means that with the diameter of the iris open being 1.2 cm, only one 144th of the pattern is spatially filtered in a normal measurement situation. This spatial filtering also takes place at approximately the average intensity of the pattern, at quadrature, so that the extraneous modulation figures shown in Figure 36 will be divided by 144 for measurement situations such as those described in section 4.2. For the largest extraneous modulation reading of Figure 36 (-62.1 dBV RMS or 1.11 mV), the corresponding value after spatial filtering is 7.7μV (-105.26 dBV RMS). This is easily seen to be well within the noise of the optical sensor output, even as shown in Figure 34. We thus conclude that the results presented in section 4.2

are entirely due to three lobe rotation and that extraneous modulation effects are entirely negligible.

As a final comment for this section, it has been suggested that, though small, the extraneous modulation effects are due to bend loss. If this were true, however, a peak at 20 Hz would be found due to bend loss occuring when the fiber both goes into tension and compression as the beam vibrates, but no such peak was observed. A more likely reason for the extraneous 10 Hz modulation is that some 10 Hz excitation is being transmitted to the floating table as the cantilever beam is forced to vibrate. Because the 10 Hz extraneous modulation figures are small, though, it is evident that the flo table is properly performing its function of excess vibration suppression, as expected, even though a vibrating structure is attached rigidly to it

4.4 Static Strain Measurements (First Attempt)

It was also of interest to study the static strain measurement capabilities of the MDS/9-633 sensor. As with the resistive strain gage evaluation measurements, the cantilever beam was loaded as shown in Figure 25(b), with masses periodically added to the basket in excess of an initial load mass of 200 grams. Now, however, the change in average beam strain, as measured by the

MDS/9-633 sensor, was to be compared to the known *induced* change in average beam strain caused by varying the load mass. Recall that the induced change in average beam strain is given as

$$\Delta \bar{\varepsilon} = \frac{3mgL}{Ebh^2} ,$$ (4.4.1)

where m is the change in load mass. Further recall that this same quantity, as measured by the MDS/9-633 sensor is given by

$$\Delta \bar{\varepsilon}_f = \frac{\Delta V}{V_Q \, \Delta \beta \, L_f \, x} ,$$ (4.4.2)

as was shown is section 3.1 and where $\Delta \beta = 1 \, 2x10^s \, m^{-1}$.

As before, the input to the optical fiber was adjusted until a properly rotating three lobe pattern was observed and the Q-point was adjusted, with the initial load mass in place, u∙ ∙g the excited PZT cylinder. Mass was then added to the basket and ΔV measured (this time through use of a strip chart recorder) as the excess load mass reached 50, 100, 150, 200, 250 and 300 grams. It wa observed, however, during early static loading tests that there was appreciable pattern drift over a period of a minute or so. It is believed that this drift is attributable to the static strain control mechanism and due in part to jacket shear for large amounts of induced static strain (recall it was mentioned

earlier that obtaining a rotating three lobe pattern was often facilitated by tensioning the fiber using the static strain control device). As the need for loading, unloading and settling the basket make the procedure for taking static strain data much more lengthy (1-2 minutes) than the procedure for taking dynamic strain data (<30 seconds) it was necessary to fully release the tension of the fiber in the static strain control device when static strain measurements were to be attempted

In addition, preliminary plots of measured versus induced strain data gave regression lines whose slope was often noticeably different from unity. This was believed to be due to the physical parameters leading to the calculation of x, in equation (4.4 2), not being precisely known for the fiber being used.

In an attempt to directly measure y the launch conditions were adjusted until a three lobe pattern was obtained which exhibited proper rotation over greater than 300°. With the fiber between the spools of the static strain control device just taut, the tension in the fiber was increased by turning the micrometer screw until the pattern rotated 120° (lobe peak to lobe peak). The change in the micrometer setting was then recorded and the tension in the fiber quickly released. This procedure was repeated several times and it was determined that the micrometer was advanced an average of 691μm for 120° rotation. The

change in length ΔL_{120} of the fiber between the spools was therefore approximately

$$\Delta L_{120} = r_1 \sin^{-1}\left(\frac{691 um}{r_2} \right) = 564.75 \, \mu m \quad .$$

where $r_1 = 7\,62$ cm and $r_2 = 9\,32$ cm represent, respectively, the radius of the rotating spool and the length of the push rod. This indicates that a change in length of 141 19 μm is needed to cause a rotation from quadrature to the nearest lobe peak (a 30° rotation).

From equation (3 1 11) we can solve for the change in fiber length required to cause pattern rotation from quadrature to the nearest lobe peak as

$$\Delta L_{30} = \frac{2\pi}{4\,\Delta\beta\,x} \quad . \tag{4 4 ?}$$

where, recall, $\Delta\beta = 1\,2\times10^4\,m^{-1}$ for the MDS/9-633 sensor. With $\Delta L_{30} = 141.19\,\mu m$ we can thus solve for x to find $x = 0\,92$, on average, for our fiber.

New data was now taken for $x = 0.92$, with $R_L = 50\,k\Omega$. See Figures 40 and 41 for plots of this data and note the near unity slope for each of these figures. In addition, the quadrature point voltage V_Q was 25.8 mV and 23.1 mV for the data of Figures 40 and 41, respectively.

It is interesting to note that the highest point on the regression line of Figure 40 occurs at $\Delta\bar{\varepsilon}_r = 104\,5\,um/m$ or $\Delta L_r = \Delta\bar{\varepsilon}_r L_r = 60.1\,um$. This indicates that the response of the MDS/9-633 sensor stays linear for ΔV, in equation (4.4.2), approximately as large as $0\,66V_Q$ The dynamic range for this linear response region can thus be found, in decibels, as

$$DR = 10\log\left|\frac{\Delta P_{max}}{\Delta P_{min}}\right|$$

$$DR = 10\log\left|\frac{0\,66P_Q}{\frac{1}{\mathcal{R}}\left(4qB(\mathcal{R}P_Q - I_D) + \frac{8k_BTB}{R_L}\right)^{\frac{1}{2}}}\right| \quad . \tag{4 4.4}$$

where ΔP_{min} was given in equation (2 3.10) and where P_Q is the optical powe. through the spatial filter aperture at quadrature. Recall that the voltage at the output of the photodetection circuit is directly related to the optical power through the spatial filter by the photo diode responsivity $\mathcal{R}$ and the load resistance R_L. Using the system parameters used in section 3.1 to determine the minimum detectable strain of the MDS/9-633 sensor we thus find that the dynamic range of this sensor, in the linear region, is approximately 52 dB.

4.5 Static Strain Measurements (Second Attempt)

Due to the drift problems encountered using the static strain control device shown in Figure 24 it was decided that this device would be redesigned and additional static strain measurements attempted. Shown in Figure 42 is the resulting new static strain control device. As seen. a length of optical fiber is attached to two axially aligned mounts, one of which exhibits axial translation as the motor shaft turns The motor used was a 200 step per revolution stepping motor and connected between the motor shaft and the movab'- mount was a #2 threaded rod with fifty-six threads per inch As the gay length of fiber between the two mounts was measured to be $L_f = 0\,522\,m$, then for every step applied to the motor the change in induced average strain in the fiber was $\Delta \bar{\varepsilon} = 4\,345\,\mu m/m$

This new static strain control device provided several advantages. First, the induced strain in the fiber was purely axial, as opposed to the axial and possibly transverse strains induced in the fiber wound on the spools of the . static strain control device. Second, there was a very simple relation between the number of steps applied to the motor and the strain induced in the fiber, as discussed above. Most importantly, though, was that there was no jacket shear in the fiber between the stationary and movable mounts This effect was

eliminated by first stripping the fiber of its jacket at the points where it was clamped and by then bonding directly to the bare fiber a length of stainless steel tubing. Due to the more rigid nature of the stainless steel tubing and the epoxy used to bond it to the bare fiber the, induced strain was more faithfully transmitted to the optical fiber, with no relaxation of the tension occuring due to elastic stretching of the polymer jacket. Indeed, it was observed that negligible pattern drift occurred over a period of several days with the fiber under significant tension. The only disadvantage to using tne new static strain control device was that the fiber between the clamps had a tendency to break just at the point where the fiber exited the stainless steel tubing This is believed to be due to slight axial misalignments of the fiber mounts causing high stress concentrations in the regions of these breaks.

As before, the input to the fiber was aligned such that a three lobed intensity distribution was present at the output that exhibited pure rotation. Pains were taken to ensure that the alignment was such that this rotation would occur over most of a full revolution Then, using a linear x-y positioning stage the spatial filter aperture was positioned over the peak of a lobe, with steps then being applied to the motor to cause the pattern to rotate to the point where the spatial filter monitored the point located half way between the maximum and minimum intensity points of a lobe. Due to the discrete nature of the increases in applied strain, though, the proper quadrature point was often overshot.

requiring final alignment using the x-y positioning stage. With the operating

point thus properly set, strain was measured as additional steps were given to

the motor

As before, the strain measured by the MDS/9-633 sensor followed equation

(4.4 2). In addition, as before it was noticed that plots of preliminary measured

versus induced strain data gave a linear regression line with slope different

from unity when x was taken as $x = 0.78$. By fitting only the first point of a

preliminary data to a regression line of unity slope it was determined that

$x = 0.86$ was a more acceptable value. Assuming $\alpha = 0.86$ additional data was

taken and is shown in Figures 43 and 44

Two final comments are necessary. First, the method by which α

determined for the data plotted in Figures 43 and 44 is admittedly questionable

due to the preliminary data used to determine x possibly not being

independant from the data subsequently taken and presented. There simply

was no way in which a reliable and independant determination of α could be

determined with the setup used. Indeed, an independant determination of the

photoelastic coefficients used to calculate α is likely to be an involved task in

itself. It is believed, however, that photoelastic effects must be considered as

the fiber is subjected to strain and that the analysis leading to equation (4.4.2)

is correct   The value of x, however, and its constituent terms is very much open to question.

The other comment necessary is that this second round of static strain measurement data was taken using a UDT model 81 Optometer   This instrument directly displayed the optical power passing through the spatial filter aperture and incident on the face of the detector head.   As per th discussion in section 3 1 leading to the result of equation (3.1.14), however, ΔP and P_0 may be directly substituted for ΔV and V_0 in equation (4.4.2).   The value of P_0 was 0.13 uW and 0.16 uW for the data plotted in Figures 43 and 44, respectively.

OUTPUT TO OSCILLOSCOPE OR SPECTRUM ANALYZER

FIBER POSITIONER

LASER
HeNe @633nm

LENS

PHOTODETECTION CIRCUIT (ATTACHED TO EYE POSITIONER)

OPTICAL FIBER (9/125μm)

POST

STATIC STRAIN CONTROL DEVICE

PZT CYLINDER (EXCITATION VIA SIGNAL GENERATOR)

CLAMP

OPTICAL TABLE

CANTILEVER BEAM

RESISTIVE STRAIN GAGE (CONNECTED ELECTRICALLY TO ONE ARM OF A WHEATSTONE BRIDGE, AND PLACED PHYSICALLY IN THE GEOMETRIC CENTER OF THE CANTILEVER BEAM)

LOADING POINT

Figure 23.   Experimental MDS/9-633 system

4 0 MDS/9-633 SENSOR EVALUATION

96

OUTPUT

EFFECTIVE
SPOOL RADIUS

(1)   (1)   ⊢R→   INPUT

(2)

(8)   (4)
(7)   (3)
(5)   (6)
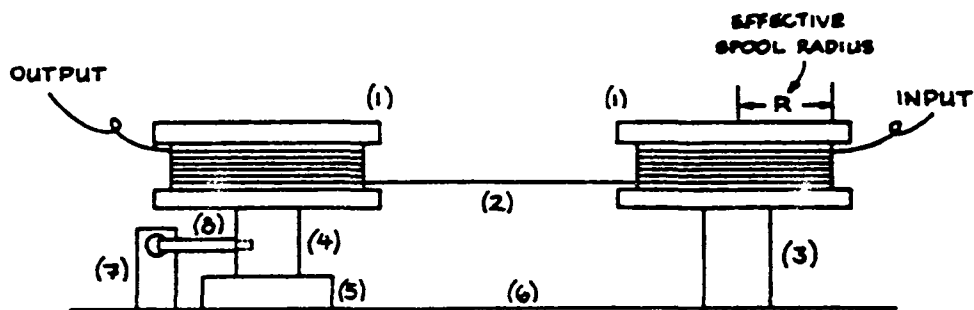
(1) SPOOL ON WHICH OPTICAL FIBER IS WOUND
(2) OPTICAL FIBER UNDER TENSION
(3) RIGID MOUNT BETWEEN SPOOL & OPTICAL TABLE
(4) RIGID MOUNT BETWEEN SPOOL & ROTATABLE BASE
(5) ROTATABLE BASE
(6) OPTICAL TABLE
(7) MICROMETER SCREW DEVICE TO PROVIDE FORCE
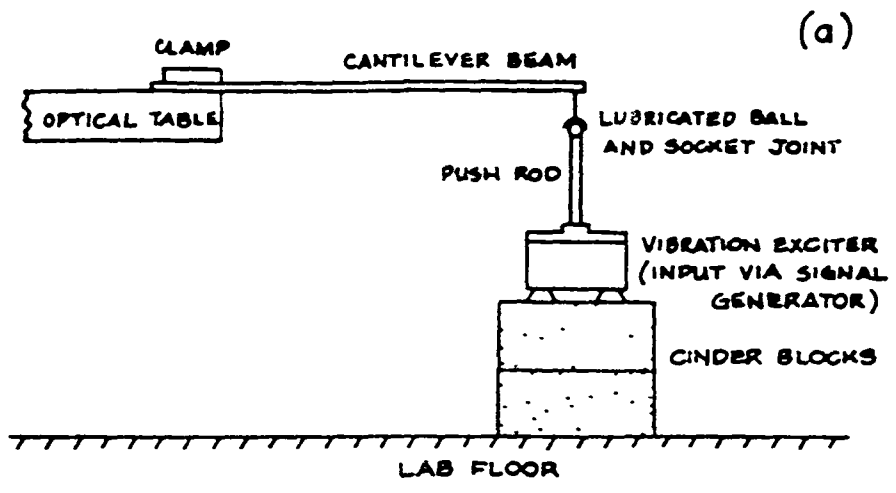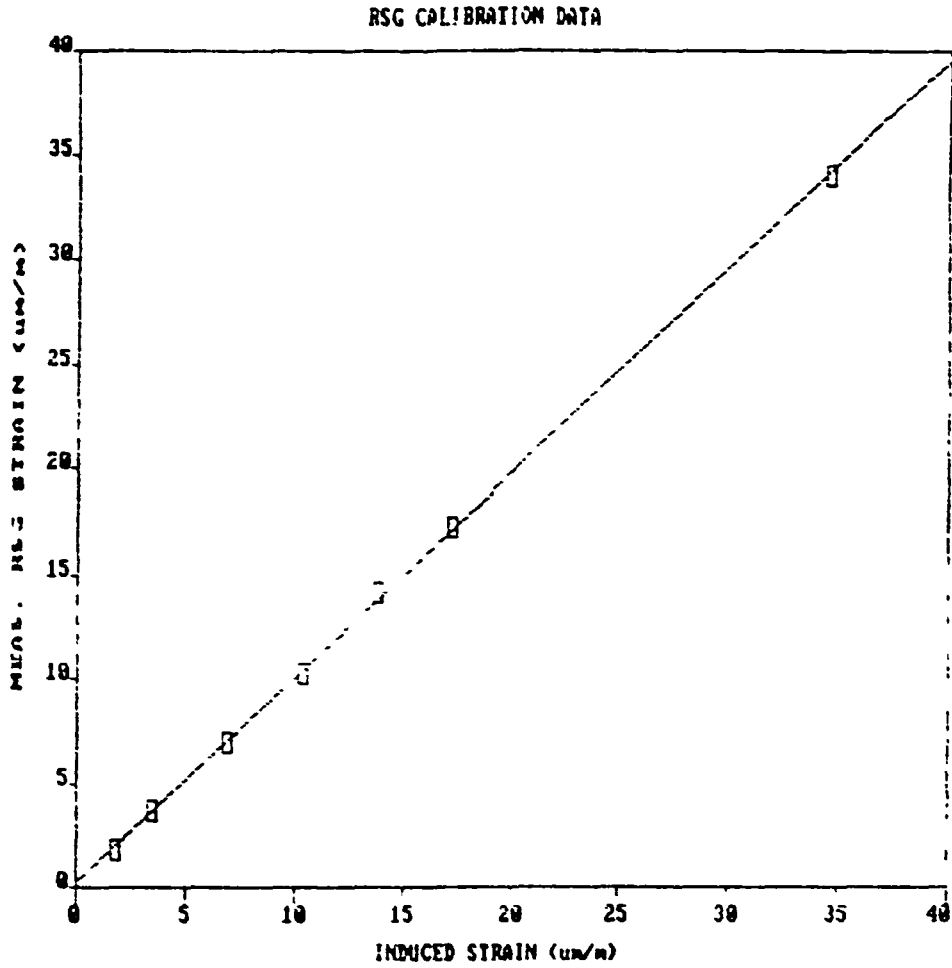   ON THE PUSH ROD
(8) PUSH ROD

Figure 24. First static strain control device

(a)

CLAMP   CANTILEVER BEAM

OPTICAL TABLE

LUBRICATED BALL
AND SOCKET JOINT

PUSH ROD

VIBRATION EXCITER
(INPUT VIA SIGNAL
GENERATOR)

CINDER BLOCKS

LAB FLOOR

(b)

CLAMP   CANTILEVER BEAM

OPTICAL TABLE

BASKET IN WHICH KNOWN
MASSES ARE PLACED FOR
STATIC LOADING PURPOSES

LAB FLOOR
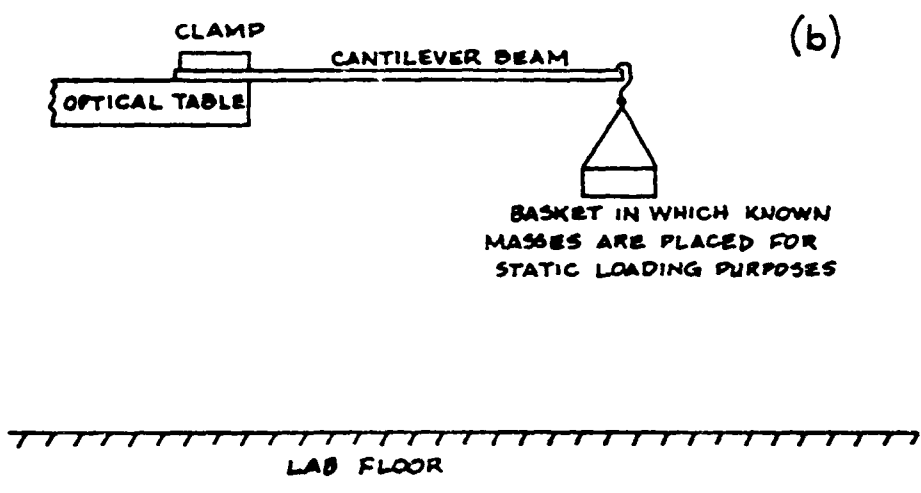
Figure 25. Loading schemes of the experimental MDS/9-633 sensor system

RSG CALIBRATION DATA

THE REGRESSION POLYNOMIAL OF LINE   1

(2.212E-01) + (9.822E-01)*x
THE VARIANCE -   2.704E-02

Figure 26.   Resistive strain gage calibration/evaluation data
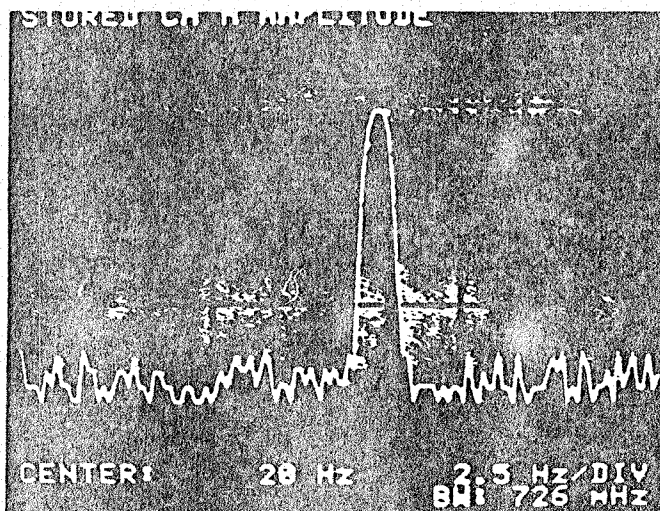
Figure 27. Cantilever beam natural frequency of vibration
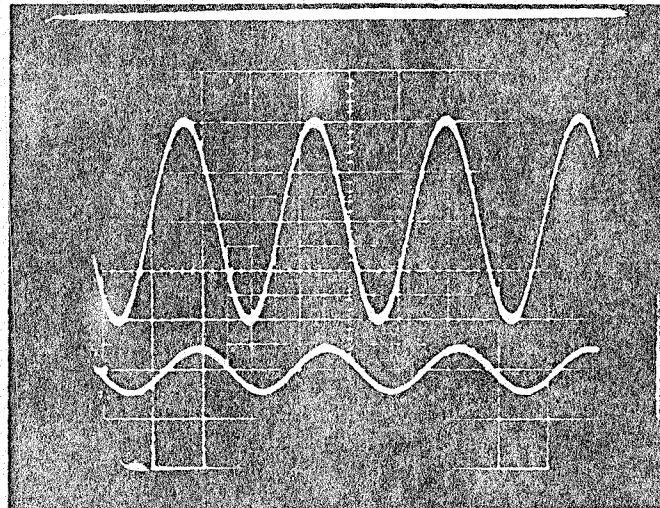
Figure 28. Highly aligned MDS/9-633 sensor output (see text for details)
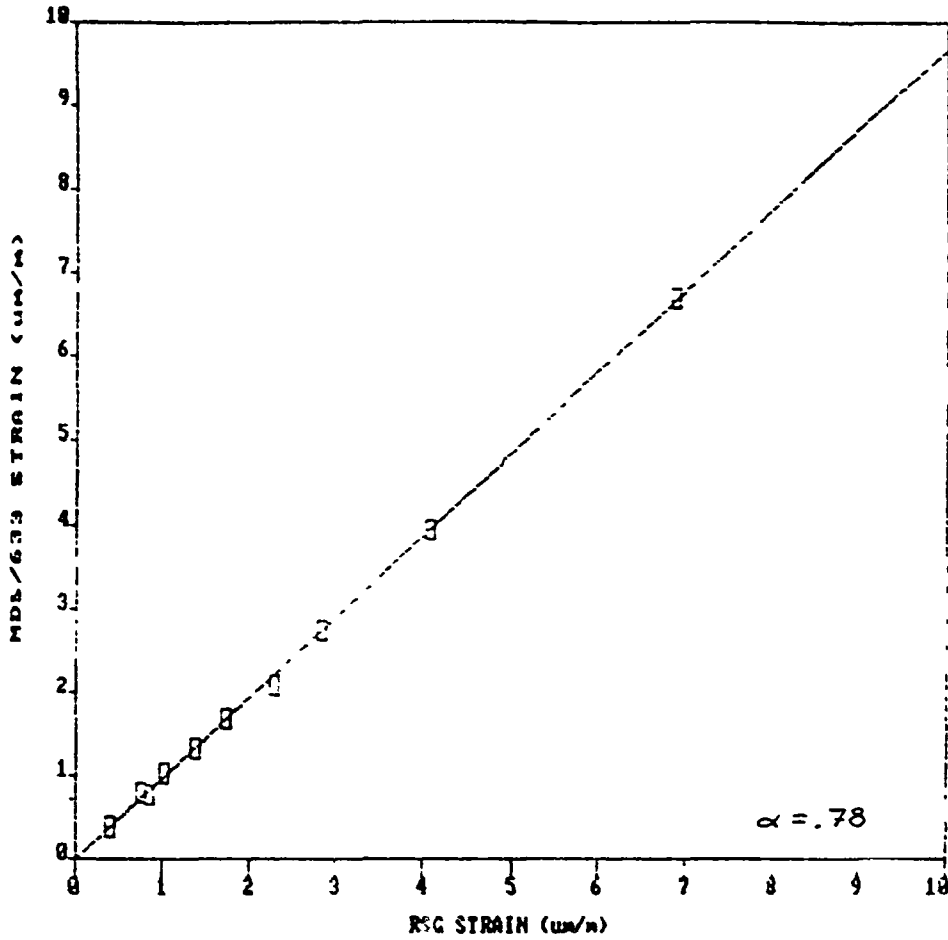
Figure 29   MDS/9-633 dynamic strain measurement data (trial 1)

AC MDS/633 vs. RSG STRAIN MEASUREMENTS (TRIAL 2)
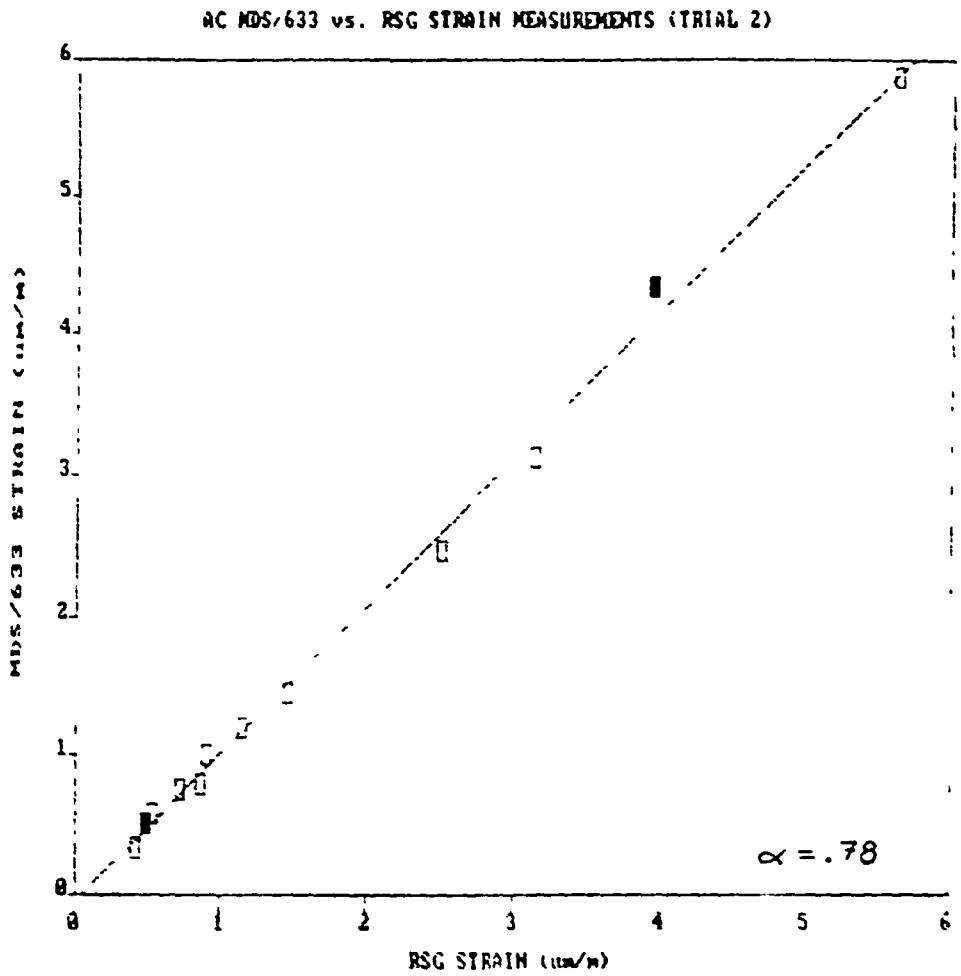
THE REGRESSION POLYNOMIAL OF LINE :

(-4.171E-02) + (1.055E-00)×x
THE VARIANCE = 9.740E-02

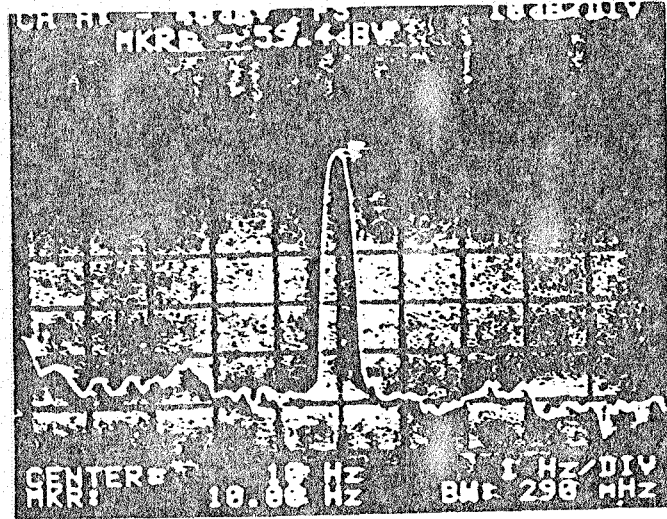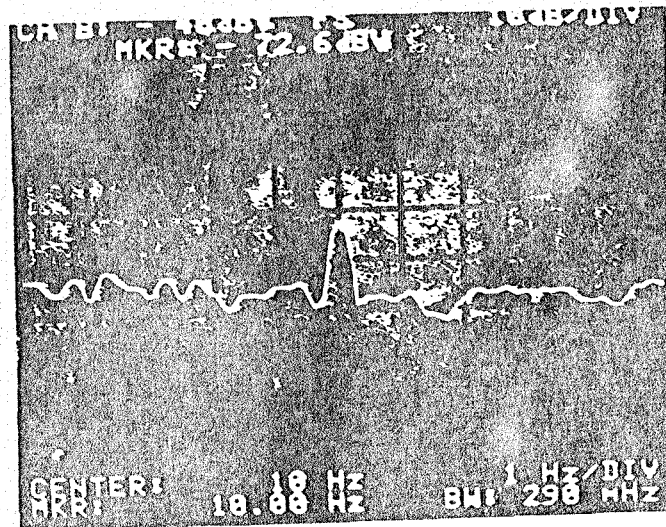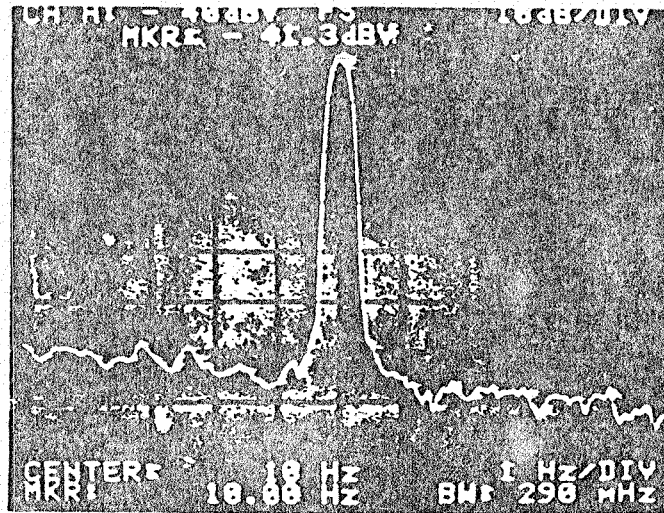Figure 30. MDS/9-633 dynamic strain measurement data (trial 2)

(a)

(b)

Figure 31. MDS/9-633 and resistive strain gage outputs for small excitation

4.0 MDS/9-633 SENSOR EVALUATION

(a)
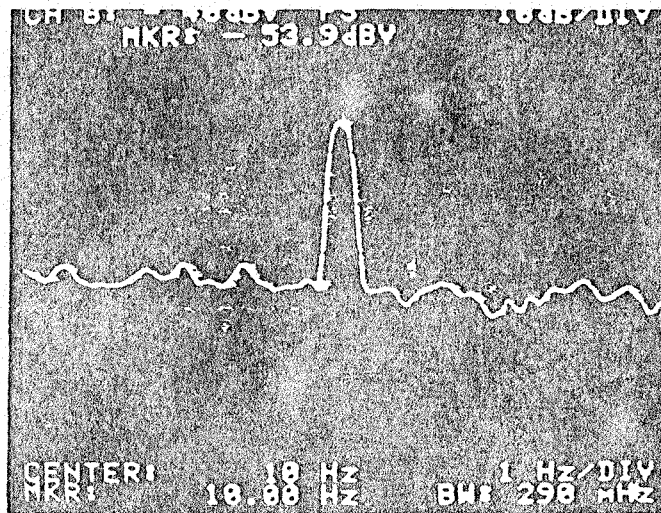
(b)

Figure 32. MDS/9-633 and resistive strain gage outputs for large excitation

4.0 MDS/9-633 SENSOR EVALUATION
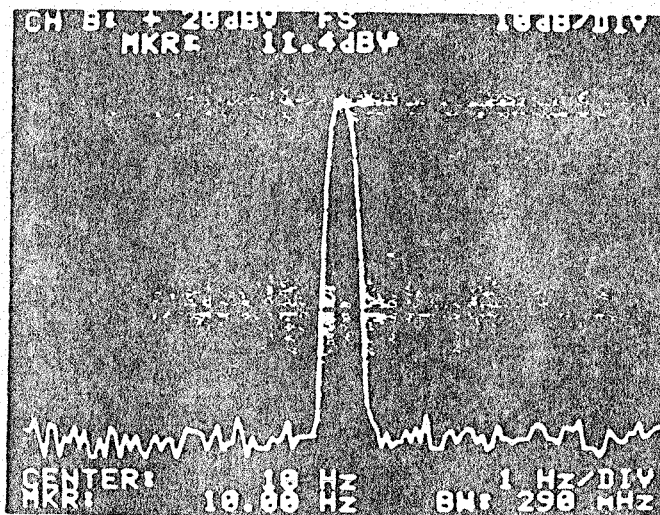
Figure 33. Input signal of the vibration exciter
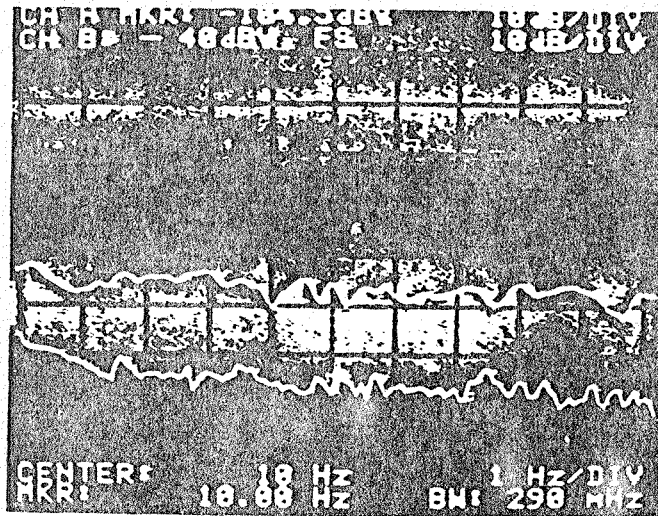
Figure 34. Noise floors of the MDS/9-633 and resistive strain gage sensors

AC MDS/633 vs. RSG STRAIN MEASUREMENTS (TRIAL 3)

RSG STRAIN (uм/m)
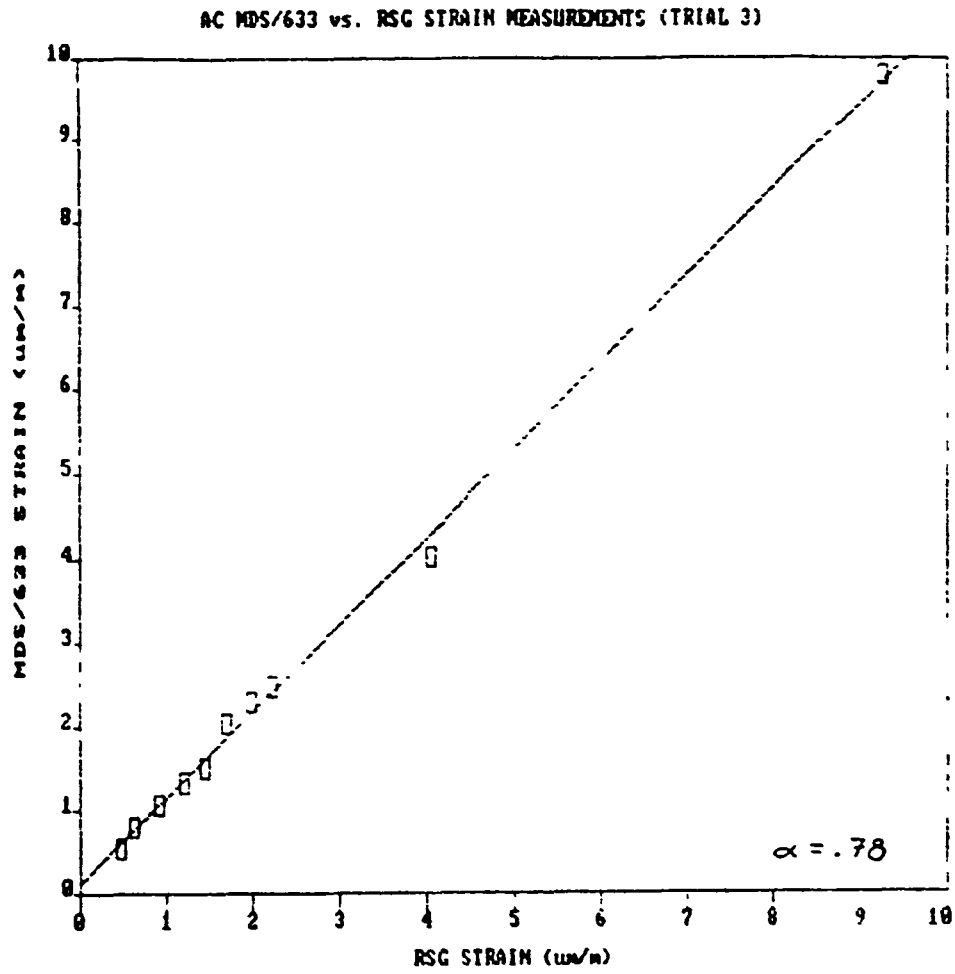
THE REGRESSION POLYNOMIAL OF LINE 1

(1.072E-01) + (1.076E+00)*X
THE VARIANCE - 1.408E-02

Figure 35.   MDS/9-633 dynamic strain measurement data (trial 3)

4.0 MDS/9-633 SENSOR EVALUATION

EXTRANEOUS AC MODULATION
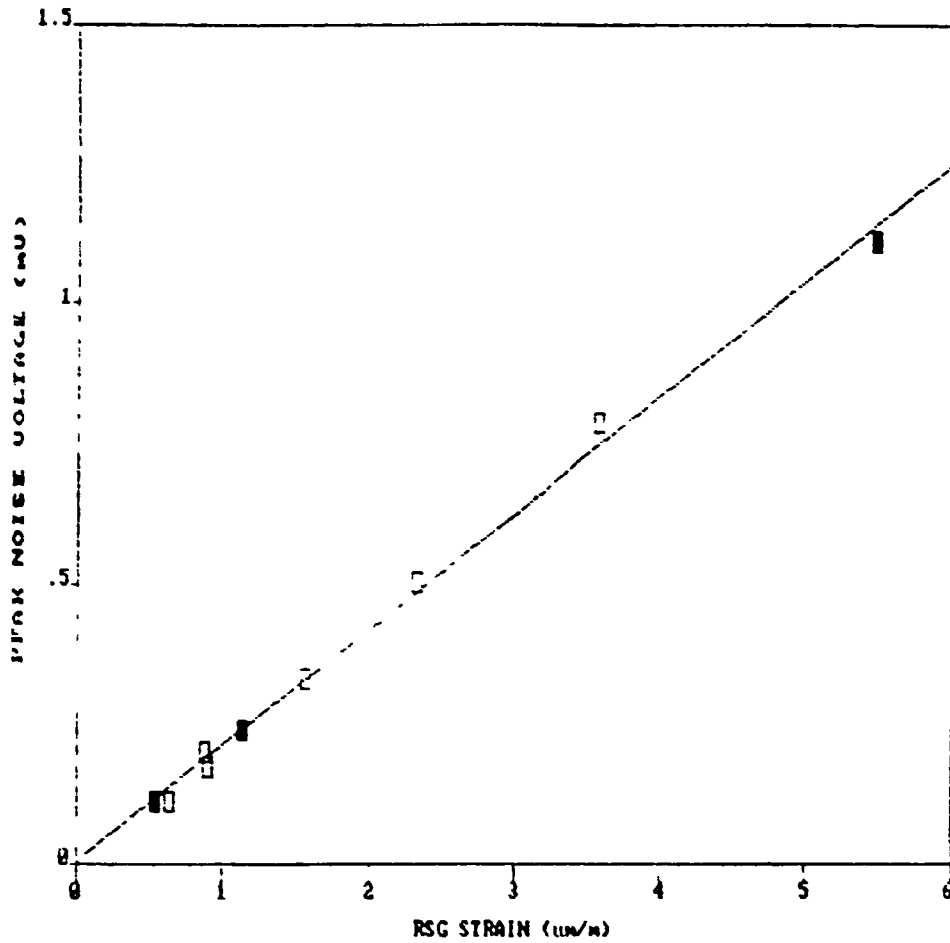
THE REGRESSION POLYNOMIAL OF LINE 1

(2.672E-02) + (2.072E-01)*x
THE VARIANCE - 4.095E-04

Figure 36. Extraneous dynamic modulation
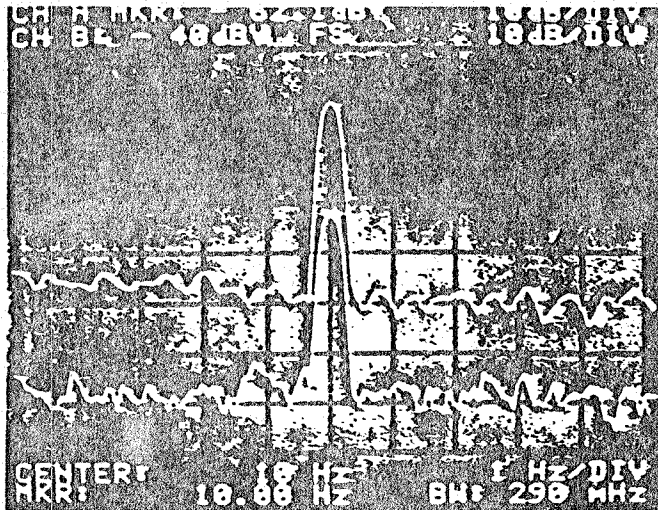
(a)
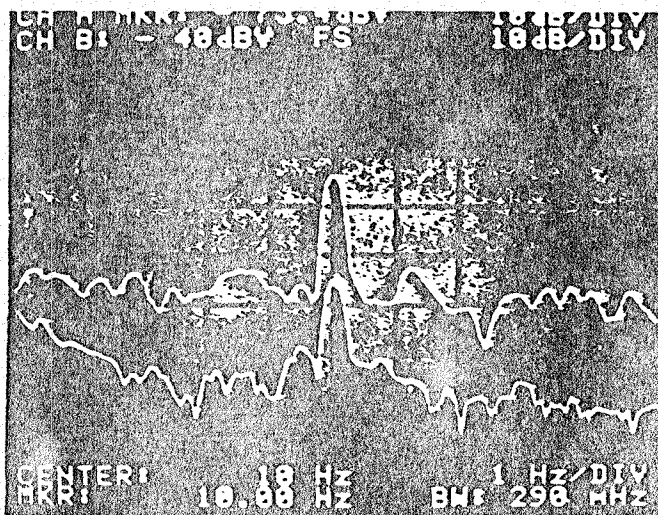
(b)

Figure 37. Extraneous modulation signals for large and moderate excitations

4.0 MDS/9-633 SENSOR EVALUATION
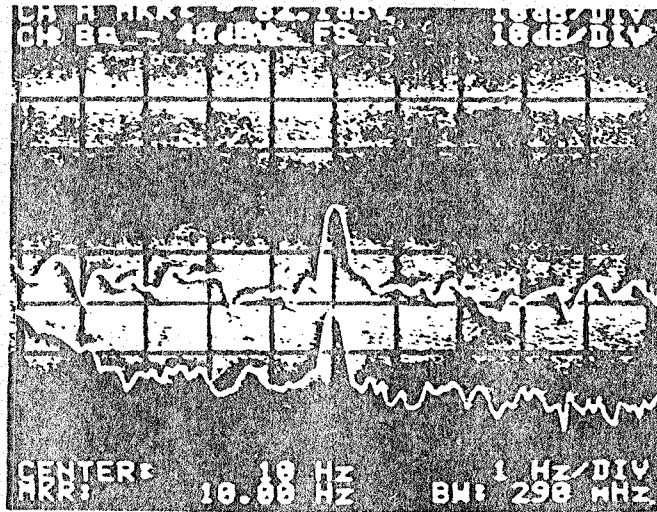
Figure 38. Extraneous dynamic modulation signals for small beam excitation

4.0 MDS/9-633 SENSOR EVALUATION
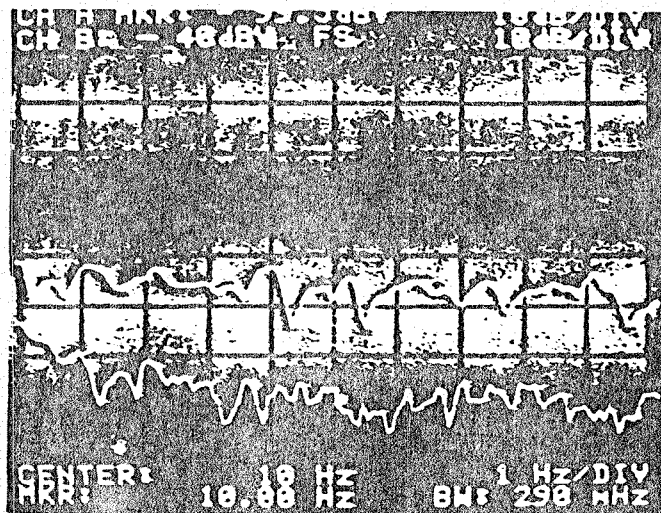
Figure 39.   Extraneous dynamic modulation noise floors

OLD STATIC STRAIN CONTROL DATA (TRIAL 1)
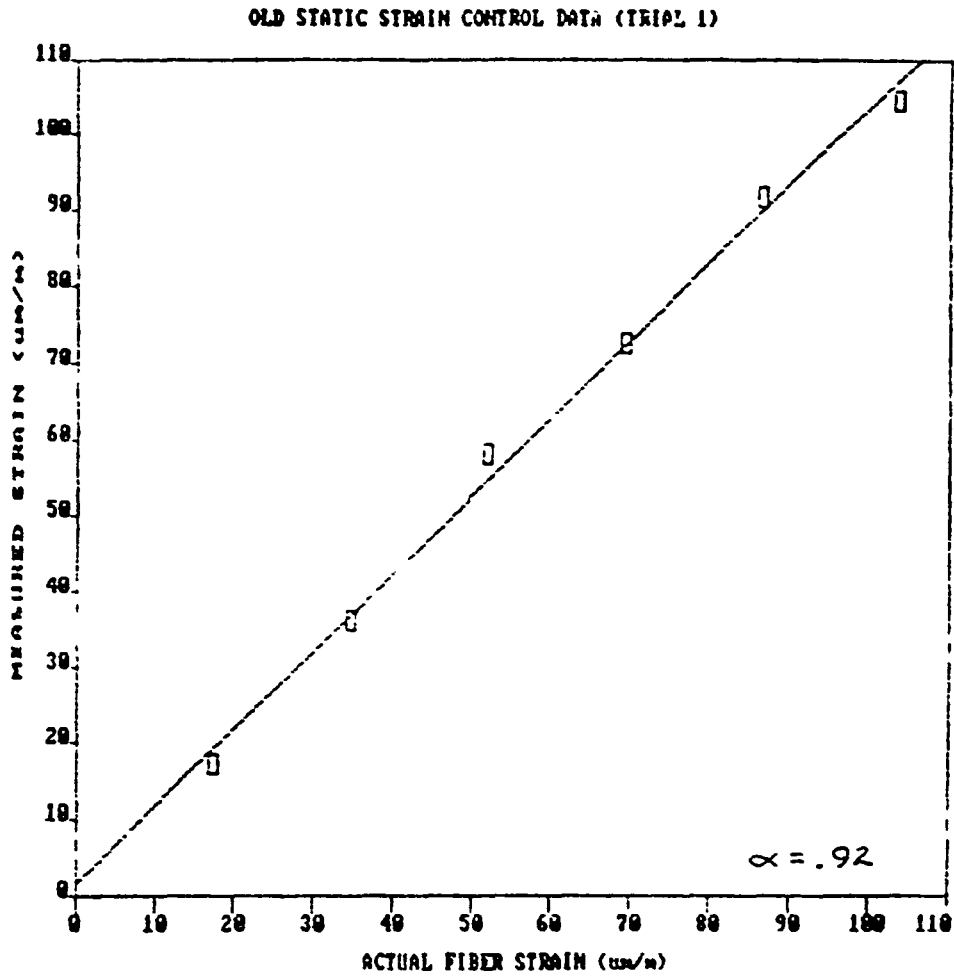
THE REGRESSION POLYNOMIAL OF LINE 1

(1.624E+00) + (1.019E+00)*X
THE VARIANCE — 4.704E+00

Figure 40. MDS/9-633 static strain measurements (first attempt trial 1)

OLD STATIC STRAIN CONTROL DATA (TRIAL 2)

$\alpha = .92$
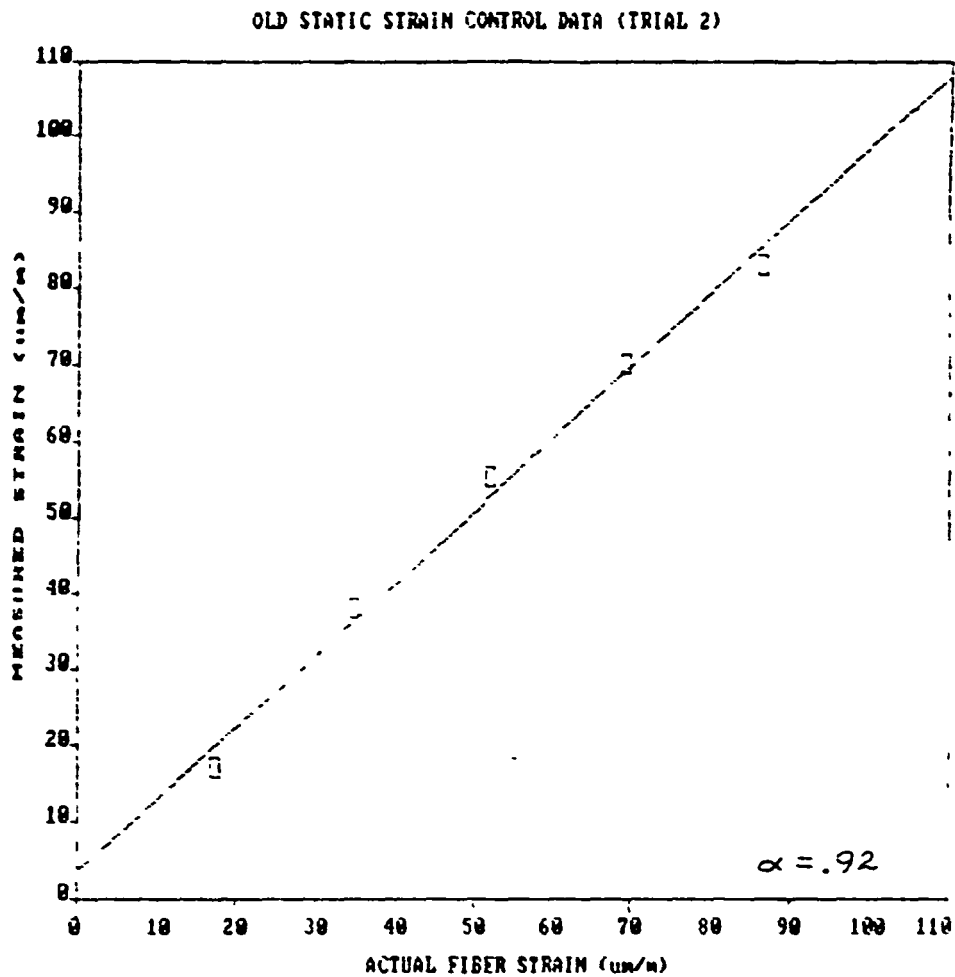
THE REGRESSION EQUATION OF LINE

THE VARIANCE =

Figure 41. MDS/9-633 static strain measurements (first attempt; trial 2)

SIDE VIEW

① MOTOR CONTROL ELECTRONICS
② DC MOTOR OR STEPPING MOTOR
③ FLEXIBLE SHAFT
④ THREADED ROD
⑤ MOVABLE MOUNT
⑥ OPTICAL FIBER TO BE STRAINED
⑦ STATIONARY MOUNT
⑧ STRAIN CONTROLLER BASE PLATE
⑨ CLAMPS
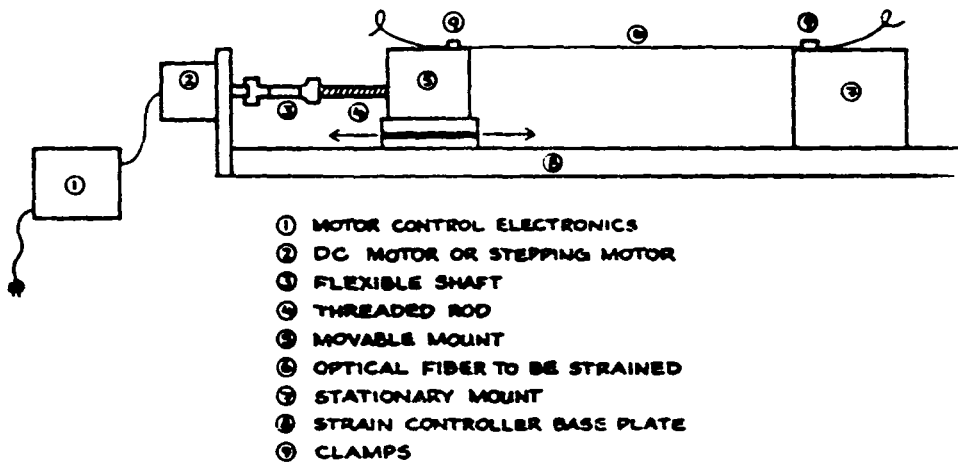
Figure 42. Redesigned static strain control device

NEW STATIC STRAIN CONTROL DATA (TRIAL 1)

$\alpha = .86$
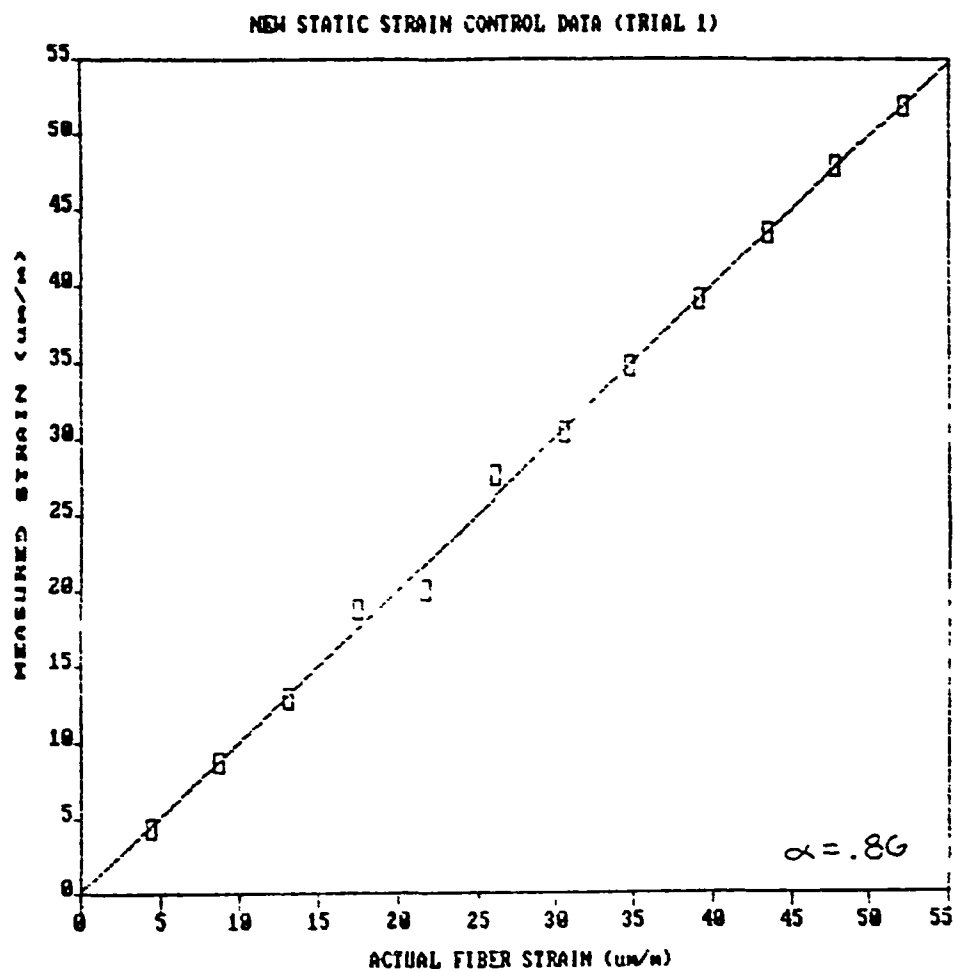
THE REGRESSION POLYNOMIAL OF LINE 1

$(1.785E-01) + (9.947E-01) * X$
THE VARIANCE - 5.671E-01

Figure 43.   MDS/9-633 static strain measurements (second attempt; trial 1)

NEW STATIC STRAIN CONTROL DATA (TRIAL 2)

$\alpha = .86$
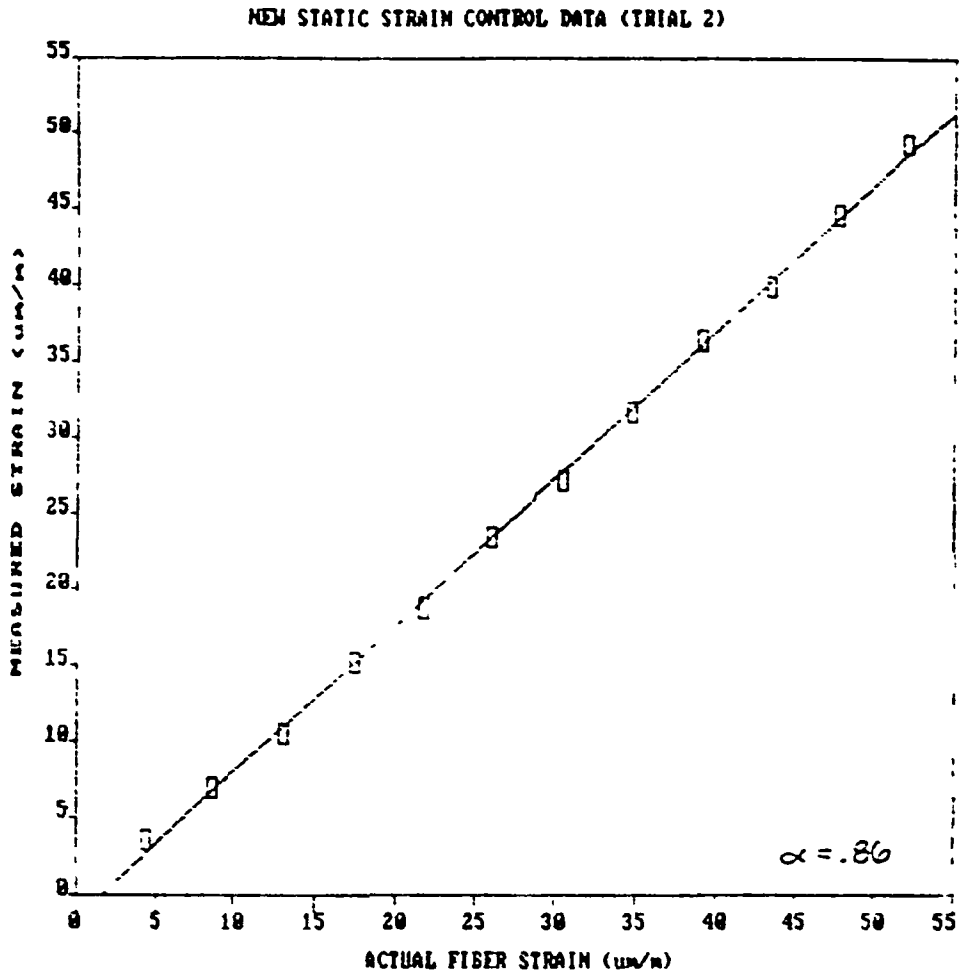
THE REGRESSION POLYNOMIAL OF LINE 1

$(-1.527E+00) + (9.597E-01)*X$
THE VARIANCE = 1.179E-01

Figure 44. MDS/9-633 static strain measurements (second attempt trial 2)

5.0 CONCLUSION

Modal domain sensors using 9 μm core diameter fiber at source wavelengths of 633 nm and 850 nm have been thoroughly described. The mode content of the most commonly observed intensity distributions at the fiber/sensor outputs, for each wavelength, have been discussed and the resulting str modulated behavior of these intensity distributions has been proven from first principles. In addition, it has been shown how this strain modulated behavior may be used as a strain detection mechanism and suggestions have been made concerning how micro-optical components can be used to construct a MDS/9-850 sensor.

The linear and highly sensitive nature of modal domain sensors has also been predicted and experimentally verified for small amounts of strain and the dynamic range of a typical modal domain sensor has been calculated.

Furthermore the many advantages and disadvantages of the various modal domain techniques have been addressed in great detail.

It is hoped that future work with modal domain sensors will involve a complete experimental evaluation of a MDS/9-850 sensor and that further investigations will result in the realization of additional in-line micro-optical injection/detection techniques for modal domain sensor use. In addition. an independant study into the values of the individual photoelastic coefficients of the optical fiber used in the previously described experiments should be undertaken with a parallel study undertaken to determine the radial changes of the core index of refraction as a function of strain and how this will affect the propagating modes.

Finally, it was assumed in section 4 2 that for quasi-static induced beam vibrations at frequencies well below the fundamental natural frequency of vibration, with small peak beam tip displacements, that the cantilever beam stress-strain relations held just as if the beam was statically loaded, with only a sinusoidal multiplicative factor appearing for the quasi-static strain case was also assumed that only the fundamental mode of vibration was excited. Although the corresponding nature of the experimental results and the theoretical predictions as to the behavior of the MDS/9-633 sensor lend

validity to these two assumptions. further investigation may be necessary to finally prove that these assumptions are valid.

5 0 CONCLUSION

APPENDIX A: Strain Characteristics of Loaded Cantilever Beams

One of the simplest and most fundamental ways in which a newly developed strain sensor may be evaluated is by attaching it to the surface of a cantilever beam which is placed under load. If the beam is constructed from some homogeneous material, such as aluminum or steel then the strain characteristics of the beam are quite easily described as a function of load, thus making the loaded cantilever beam a convenient strain standard. Consider for instance the cantilever beam of Figure 45. Assuming the is made of a homogeneous material, the stress at any location on or within a beam is given by

$$\sigma = \frac{M_g z}{I} \quad [Pa] \; .\tag{A.1}$$

where z is the distance above or below the neutral axis, $M_j = F \times \ell$ is the bending moment and I is the moment of inertia given as

$$I = \frac{h^3 b}{12} \qquad (A\,2)$$

If we now consider only the surface which is in tension when the beam is loaded we find that the surface stress σ_{sur} is

$$\sigma_{sur} = \frac{F\ell(h/2)}{hb^3/12} = \frac{6F\ell}{h^2 b} \qquad \cdot \qquad (A.3)$$

Recalling that strain ε is related to stress by the relation $\varepsilon = \sigma/E$, where E is the modulus of elasticity, we see that the strain along the tensed surface of the cantilever beam is

$$\varepsilon_x(\ell) = \frac{6F\ell}{Eh^2 b} \qquad \cdot \qquad (A.4)$$

Note that this result indicates that the strain along the surface of the beam increases linearly as a function of ℓ, being zero at the free end and be.. maximum at the clamped end. The average strain in the beam thus occurs at $\ell = L/2$. Also note that by changing the sign of the strain relation in equation (A.4) one can describe the strain induced in the beam surface being compressed. The negative sign simply indicates the compressional force.

Often, though, one is interested in the change in average strain in a situation where the loading force is changed by varying masses attached to the beam. We will call this change in average strain $\Delta\bar{\varepsilon}$ which is simply given by

$$\Delta\bar{\varepsilon} = \frac{3mgL}{Ebh^2} \quad , \tag{A.5}$$

where m is the change in mass, g is the acceleration due to gravity and the fact that average strain occurs at $\ell = L/2$ has been used. This quantity can easily be measured by a resistive strain gage placed at the geometric cente. of the beam surface [12]

A.1 Average Strain Induced in an Optical Fiber

In the evaluation of fiber optic strain sensors it is often desirable to loop a sensing length of fiber along a cantilever beam as indicated in Figure 46 Since the output of an optical fiber strain sensor is actually a measure of *average* strain in the fiber sensor length (more commonly called the gage length) we can calculate the average change in strain, $\Delta\bar{\varepsilon}_f$, to which the fiber is subjected along its path by evaluating

$$\Delta \bar{\varepsilon}_f = \frac{\Delta L}{L_f} = \frac{1}{L_f} \int_0^{L_f} \varepsilon_x \, d\ell \quad , \tag{A.6}$$

where ΔL is the total elongation of the fiber path and L_f is the gage length.

Using equation (A 4) we can evaluate ΔL as follows·

$$\Delta L = 2 \int_{AB} \varepsilon_x \, d\ell + \int_{BC} \varepsilon_x \, d\ell$$

$$\Delta L = 2 \int_{L_1}^{L} \frac{6F\ell}{Eh^2 b} \, d\ell - 2r \int_0^{\pi/2} \frac{6F(L_1 - r\cos\varphi)}{Eh^2 b} \sin\varphi \, d\varphi$$

$$\Delta L = \frac{6mg}{Eh^2 b}(L^2 - L_1^2) + \frac{12mgr}{Eh^2 b}\left(L_1 - \frac{r}{2}\right)$$

$$\Delta L = \frac{6mg}{Eh^2 b}(L^2 - L_1^2 + 2L_1 r - r^2) \quad . \tag{A.7}$$

Note that a simple transformation from rectangular to polar coordinates was necessary to integrate the strain effects in the curved portion of the fiber. Now, by dividing equation (A.7) by the fiber gage length and recalling that m is the change in load mass we find that $\Delta \bar{\varepsilon}_f$ is

$$\Delta \bar{\varepsilon}_f = \frac{6mg}{Eh^2 bL_f} (L^2 - L_1^2 + 2L_1 r - r^2) \ . \qquad (A\ 8)$$

where

$$L_f = 2(L - L_1) + \pi r \ . \qquad (A\ 9)$$

Notice in equation (A 8) that if $r = L_1$ so that the curved portion of fiber just touches the free end of the cantilever beam then

$$\Delta \bar{\varepsilon}_f = \frac{6mg}{Eh^2 b} \frac{L^2}{L_f} \ , \qquad (A\ 10)$$

which, if $L_f \simeq 2L$, is approximately the same result expressed in equation (A.5). More precisely, if we choose L_1, L and r properly, it is possible to make the results of equations (A.5) and (A.8) express the same quantity. Assuming L and L_1 to be fixed, we can solve for r as follows:

$$\frac{6mg}{Eh^2 bL_f} (L^2 - L_1^2 + 2rL_1 - r^2) = \frac{3mgL}{Ebh^2}$$

$$L^2 - L_1^2 + 2rL_1 - r^2 = \frac{L}{2} (2(L - L_1) + \pi r)$$

$$r^2 - r\left(2L_1 - \frac{\pi L}{2}\right) - (L_1 L - L_1^2) = 0$$

$$r = \left(L_1 - \frac{\pi L}{4}\right) + \left\{L_1 L\left(1 - \frac{\pi}{2}\right) + \left(\frac{\pi L}{4}\right)^2\right\}^{\frac{1}{2}} \qquad (A.11)$$

These last considerations are interesting in that they demonstrate that by using simply loaded cantilever beams an optical fiber strain sensor can be subjected to known strain effects while having its performance evaluated simultaneously against more commonly used strain sensors such as resistive strain gages. Finally, it should be mentioned that due to the relatively insensitive nature of both resistive strain gages and optical fibers to transverse strain, no considerations in the previous formulations have been given to transverse beam contractions [13].
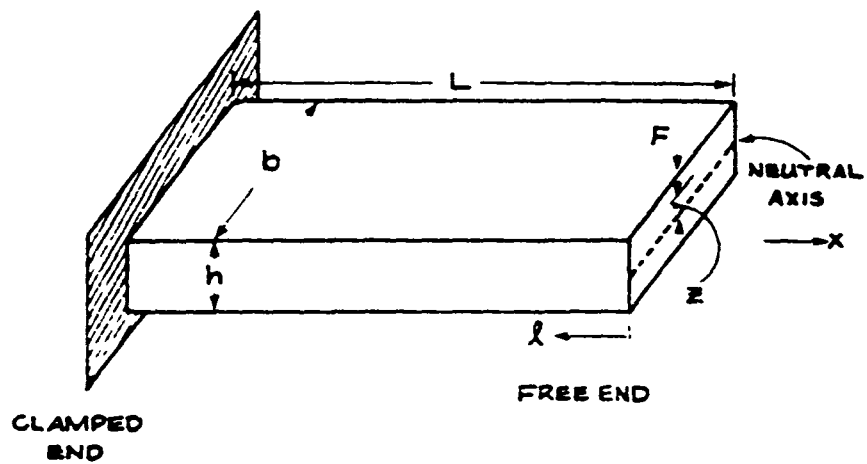
F = LOADING FORCE
L = BEAM LENGTH
b = BEAM WIDTH
h = BEAM THICKNESS
z = DISTANCE FROM NEUTRAL AXIS

Figure 45. Cantilever beam geometry

L = CANTILEVER BEAM LENGTH
L-L₁ = LENGTH OF FIBER WHICH IS STRAIGHT
b = BEAM WIDTH
r = RADIUS OF CURVED FIBER SECTION
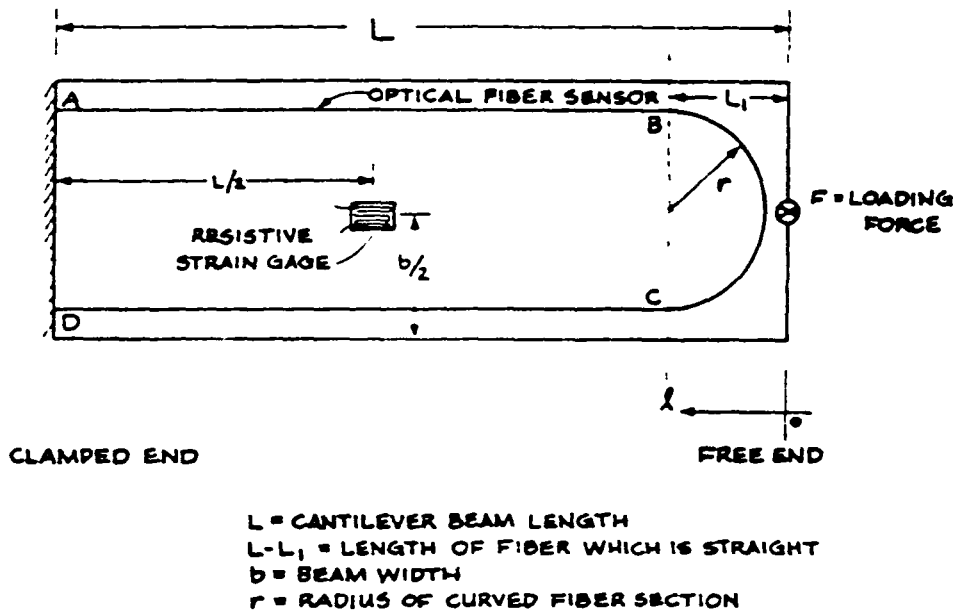
Figure 46. Optical fiber and resistive strain gage placement parameters

APPENDIX B: The Resistive Strain Gage

Lord Kelvin first observed that a change in strain imposed on a wire is accompanied by a change in resistance ΔR of the wire. The relationship between resistance change ΔR and strain ε can be derived by considering a uniform conductor of length L, cross-sectional area A, and resistivity ρ. The resistance R of such a conductor is given by

$$R = \frac{\rho L}{A} \quad . \tag{B 1}$$

Differentiating equation (B.1) and dividing by R gives

$$\frac{dR}{R} = \frac{d\rho}{\rho} + \frac{dL}{L} - \frac{dA}{A} \quad . \tag{B 2}$$

However,

$$\frac{dA}{A} = -2\,v\,\frac{dL}{L} + v^2\left(\frac{dL}{L}\right)^2 \qquad (B\ 3)$$

under elastic deformations where v is the Poisson's ratio of the conductor material   The strain sensitivity S_A of the conductor is defined as

$$S_A = \frac{dR/R}{dL/L} \qquad (B\ 4)$$

Substituting equations (B 2) and (B.3) into equation (B 4) gives us

$$S_A = \frac{d\rho\ \upsilon}{dL_i L} + 1 - 2\upsilon - \upsilon^2\left(\frac{dL}{L}\right) . \qquad (B.5)$$

The last three terms of equation (B.5) are due to dimensional changes in the conductor   The first term is due to changes of resistivity with strain. The last term is usually neglected for elastic strains since it is small ($<$ 0 1ε) compared to the other terms ($\sim$ 1.60). The derivation of (B 5) is modified slightly for large strains since the conductor undergoes plastic deformation [13].

B.1 Strain Gage Calibration

In practice equation (B 5) is not very useful since it is only valid for a single filament conductor and because the first factor which describes the change of resistivity with respect to strain is often unknown. Typically the conductor of a resistive strain gage is formed into a grid to reduce its size as shown in Figure 47 This causes the gage to exhibit sensitivity to both axial and transverse strain The response of a surface mounted gage that is subjected to a axial strain ε_a, a transverse strain ε_t and a shearing strain γ_{at} can be expressed by

$$\frac{dR}{R} = S_a\varepsilon_a + S_t\varepsilon_t + S_s\gamma_{at} \ . \tag{B.6}$$

where S_a, S_t and S_s are the sensitivities of the gage to axial transverse and shearing strains, respectively In general. the gage sensitivity to shearing strain is small and thus neglected so that

$$\frac{dR}{R} = S_a(\varepsilon_a + k_t\varepsilon_t) \ . \tag{B 7}$$

where $k_t = S_t S_a$ is defined as the transverse sensitivity factor for the gage.

Strain gage manufacturers provide the transverse sensitivity factor k_t and a calibration constant known as the gage factor for each gage. The gage factor S_g represents the calibration constant for a batch or lot of gages and is determined by testing sample gages drawn from a lot of gages in a given production run Resistance change dR experienced by a gage is related to the gage factor and the axial strain by

$$\frac{dR}{R} = S_g \varepsilon_a \qquad (B\ 8)$$

The stress field in the calibration beam used for the determination of S_g is always unaxial. therefore the gage is subjected to a biaxial strain of

$$\varepsilon_t = -v_0 \varepsilon_a \quad , \qquad (B.9)$$

where $v_0 = 0.285$ is Poisson's ratio for the calibration beam material. Substituting equation (B 9) into equation (B 7) and comparing with equation (B.8) yields

$$S_g = S_a (1 - k_t v_0) \quad ,$$

or

$$S_a = \frac{S_g}{1 - k_t v_0} \quad . \qquad (B.10)$$

Therefore when the strain gage is used to measure unaxial strain in a material other than the calibration beam we see that

$$\frac{dR}{R} = \frac{S_g}{1 - k_t v_0}(\varepsilon_a + k_t \varepsilon_t) = \frac{S_g \varepsilon_a}{1 - k_t v_0}(1 - k_t v)$$

or

$$\varepsilon_a = \frac{dR}{R}\left(\frac{1 - k_t v_0}{1 - k_t v}\right)\frac{1}{S_g} \quad , \tag{B 11}$$

where v is the Poisson s ratio of the structure to which the strain gage is attached. It should be evident from equation (B.11) that the calibration procedure used to determine k_t and S_g allows transverse strain effects to be "calibrated out" of the actual strain gage measurement [13] Also. it should be evident that the change in average strain in a loaded cantilever beam as described in Appendix A could be measured using a resistive strain gage placed in the geometric center of the beam by using the relation

$$\Delta \bar{\varepsilon} = \frac{\Delta R}{R}\left(\frac{1 - k_t v_0}{1 - k_t v}\right)\frac{1}{S_g} \quad , \tag{B.12}$$

where R is the initial gage resistance (often measured), v is Poisson's ratio of the test material and ΔR is the measured change in gage resistance

B.2 The Use of Wheatstone Bridges to Measure ΔR

In order to enable small changes in strain and therefore small changes in resistance to be measured in a resistive strain gage. a Wheatstone bridge circuit with an amplifier output stage is often used. A constant-voltage excitation Wheatstone bridge circuit is shown in Figure 48. For this bridge circuit, the error voltage E_0 is given by

$$E_0 = \frac{R_1 R_3 - R_2 R_4}{(R_1 - R_2)(R_3 + R_4)} V_{in} \tag{B.13}$$

Equation (B 13) indicates that the initial error voltage will vanish ($E_0 = 0$) if

$$R_1 R_3 = R_2 R_4 \quad . \tag{B.14}$$

When equation (B.14) is satisfied. the bridge is said to be balanced. This means that the small unbalanced voltage caused by a change in resistance of any arm of the bridge is measured from a zero or near-zero condition. This small signal can easily be amplified to significant levels for recording.

If a single resistive strain gage is placed in the bridge circuit a indicated in Figure 48, a voltage ΔE_0 developes at the input to the amplifier stage when the nominal resistance of the gage R is changed by an amount ΔR Such changes

in resistance are in general due to strain or temperature variations; however in the following analysis the change in ΔR due to temperature effects will be assumed negligible.

If the fixed resistors R_2 R_3 and R_4 are chosen to have the same resistance value as the nominal resistance R of the resistive strain gage, we have that

$$\Delta E_0 = \frac{1}{4} \frac{\Delta R}{R} (1 - \eta)V_{in} \ . \tag{B 15}$$

where

$$\eta = \frac{\Delta R/R}{\Delta R/R + 2} \tag{B 16}$$

Substituting equation (B 16) into equation (B.15) we find that

$$\Delta E_0 = \frac{1}{4} \frac{\Delta R}{R} \left(1 - \frac{\Delta R/R}{\Delta R/R + 2}\right)V_{in}$$

$$\Delta E_0 = \frac{1}{4} \frac{\Delta R}{R} \left(\frac{2}{\Delta R/R + 2}\right)V_{in}$$

$$\Delta E_0 \simeq \frac{1}{4} \frac{\Delta R}{R} \left(1 - \frac{\Delta R}{2R}\right)V_{in} \ .$$

where the binomial expansion $(1 + a)^{-1} \simeq (1 - a)$ has been used since typically $\Delta R << R$ Continuing,

$$\Delta E_0 = \frac{1}{4} \frac{\Delta R}{R} V_{in} - \frac{\Delta R^2}{8R^2} V_{in} \quad . \qquad (B.17)$$

Since the second term of equation (B 17) is very much smaller that the first. we have

$$\Delta E_0 = \frac{1}{4} \frac{\Delta R}{R} V_{in} \quad . \qquad (B.18)$$

The output of the inverting amplifier is then given by the relation

$$V_{out} = -\frac{R_5}{R_5} \Delta E_0 = -\frac{1}{4} \frac{R_5}{R_5} \frac{\Delta R}{R} V_{in} \quad , \qquad (B.19)$$

where R_5 is chosen large enough so as not to cause significant loading of the bridge network and where a near-zero initial condition is assumed for ΔE_0 (i.e., the bridge is assumed to be initially balanced) [14].

By substituting equation (B.12) into equation (B 19) and then rearranging terms we find that the change in average strain induced in a resistive strain gage is given by

$$\Delta \bar{\varepsilon} \;=\; -\; \frac{V_{out}}{V_{in}} \;\; \frac{4R_5}{S_g R_6} \left[\frac{1 - k_t \text{'}_0}{1 - k_t \text{'}} \right] \qquad (B.20)$$

Due to the linear nature of resistive strain gages. Wheatstone bridges and simple inverting amplifiers. the peak change in average strain as induced in a resistive strain gage by a sinusoidally varying strain field is given by

$$\Delta \bar{\varepsilon}_p \;=\; \frac{V_p}{V_{in}} \;\; \frac{4R_5}{S_g R_6} \left[\frac{1 - k_t \text{'}_0}{1 - k_t \text{'}} \right] \; . \qquad (B.21)$$

where the negative sign has been dropped in equation (B 21) since V_p, which represents the amplitude of the sinusoidally varying output voltage. is independant of phase Considering once again the case of measuring the change in average strain in a cantilever beam we see that equation (B.20) will be most useful when the beam is subjected to a static load and that equation (B 21) will be most useful when the beam is forced to vibrate under the influence of a sinusoidally varying load.

Finally, in order to investigate the minimum detectable strain for a resistive strain gage used in a detection network such as that of Figure 48, we differentiate equation (B.21) and divide by $\Delta \bar{\varepsilon}_p$ to obtain

$$\frac{d\Delta \bar{\varepsilon}_p}{\Delta \bar{\varepsilon}_p} \;=\; \frac{dV_p}{V_p} \;+\; \frac{dR_5}{R_5} \;-\; \frac{dV_{in}}{V_{in}} \;-\; \frac{dS_g}{S_g} \;-\; \frac{dR_6}{R_6} \; , \qquad (B.22)$$

where in equation (B 21) k \o and v are assumed to be constant and where dR_s, dR_6 and dS_g represent manufacturer stated tolerances on the values R_3, R_6 and S_g, respectively. Also, dV_p and dV_{in} represent the inaccuracies of measuring V_p and V_n on, say. digital voltmeters, oscilloscopes or spectrum analizers By then setting the ratio $d\Delta\bar{\varepsilon}_p/\Delta\bar{\varepsilon}_p$ equal to unity and solving for V_p we will have a minimum value of V_p needed for reliable measurements which when substituted into equation (B.21) will give the minimum reliable value of $\Delta\bar{\varepsilon}_p$ Minimum detectable strain values on the order of 10^{-6} are not uncommon for resistive strain gages used in typical measurement situations, with higher sensitivities expected in cortroled laboratory environments [13]

CONNECT TO
WHEATSTONE BRIDGE
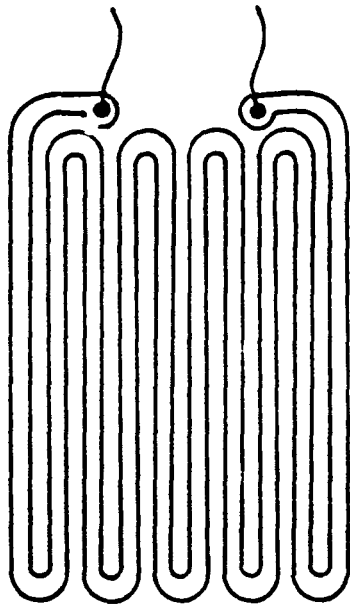
RESISTIVE STRAIN GAGE

Figure 47. A resistive strain gage

$R_i =$ RESISTIVE STRAIN GAGE

$-R_6/R_5 =$ AMPLIFIER GAIN A
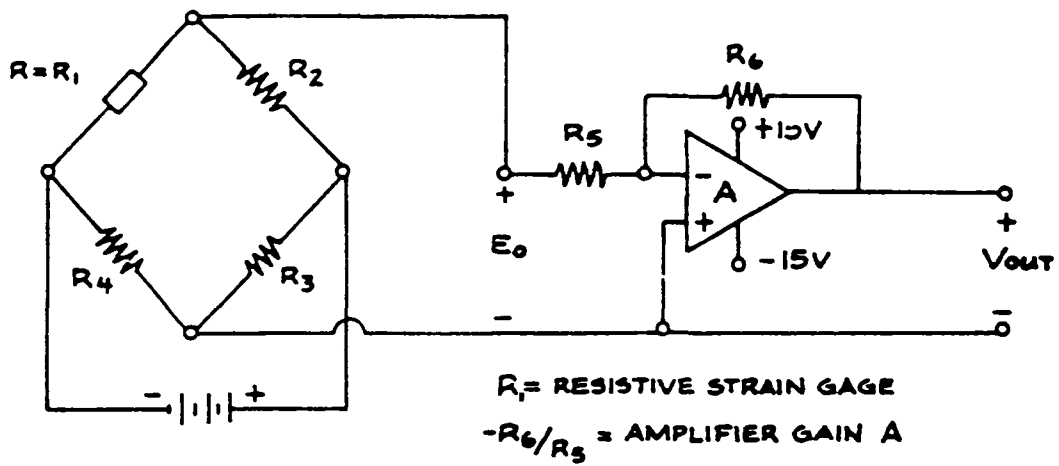
Figure 48.   A Wheatstone bridge circuit with amplifier

APPENDIX C: Bessel Function Numerical Expansions

The following numerical expansions for $J_0(x)$ and $J_1(x)$ can be used to aid in plotting modal intensity patterns [15].

$$J_0(x) = 1 - A\left(\frac{x}{3}\right)^2 + B\left(\frac{x}{3}\right)^4 - C\left(\frac{x}{3}\right)^6 + D\left(\frac{x}{3}\right)^8 - E\left(\frac{x}{3}\right)^{10} + F\left(\frac{x}{3}\right)^{12} \quad,$$

where

$$A = 2.2499997$$

$$B = 1.2656208$$

$$C = 0.3163866$$

$$D = 0.0444479$$

$$E = 0.0039444$$

$$F = 0.0002100$$

and

$$x^{-1}J_1(x) = 0.5 - G\left(\frac{x}{3}\right)^2 - H\left(\frac{x}{3}\right)^4 - I\left(\frac{x}{3}\right)^6 - J\left(\frac{x}{3}\right)^8 - K\left(\frac{x}{3}\right)^{10} + L\left(\frac{x}{3}\right)^{12}$$

where

$$G = 0.56249985$$

$$H = 0.21093573$$

$$I = 0.03954289$$

$$J = 0.00443319$$

$$K = 0.00031761$$

$$L = 0.00001109$$

These expansions give eight significant digits for $-3 \leq x \leq 3$. For reasonable departures of $|x| \geq 3$ these expansions also give very good results for plot purposes.

APPENDIX D: FORTRAN Programs

The following FORTRAN programs are useful for generating the data needed to create the line and surface plots of the various intensity distributions of interest in modal domain sensing.

```
CCCCCCCCCCCCCCCCCCCCCCCCCCCCCCCCCCCCCCCCCCCCCCCCCCCCCCCCCCCCCCCCCCC
C                                                                 C
C     THIS PROGRAM GENERATES THE VALUES WHICH WHEN PLOTTED RESULT  C
C     IN THE LINE PLOTS WHICH DESCRIBE THE TWO LOBE PATTERN OF     C
C     INTEREST IN MODAL DOMAIN SENSING                            C
C                                                                 C
CCCCCCCCCCCCCCCCCCCCCCCCCCCCCCCCCCCCCCCCCCCCCCCCCCCCCCCCCCCCCCCCCCC
C
      REAL J0(100),J1(100),XVAL(100),I,J,K,L
C
      A = 0.56249985
      B = 0.21093573
      C = 0.03954289
      D = 0.00443319
      E = 0.0003176l
      F = 0.00001109
      G = 2.2499997
      H = 1.2656208
      I = 0.3163866
      J = 0.0444479
      K = 0.0039444
      L = 0.0002100
C
      RBAR = -4.59
C
      DO 10 N = 1,100
C
           RBAR = RBAR + 0.09
           XVAL(N) = RBAR
           X1 =   625*RBAR/3.0
           X0 = .400*RBAR/3 0
C
           J0(N) = 1.0 - G*(X0**2) + H*(X0**4) - I*(X0**6)
     $                  + J*(X0**8) - K*(X0**10) + L*(X0**12)
C
           J1(N) = (0.5 - A*(X1**2) + B*(X1**4) - C*(X1**6)
     $                  + D*(X1**8) - E*(X1**10) - F*(X1**12))
     $                  *3.0*X1
C
 10   CONTINUE
C
      DO 20 N = 1,100
C
           OUT =    (J0(N)**2)
     $              + (J1(N)**2)
     $              + (2.0*J0(N)*J1(N))
C
           WRITE(08,*) XVAL(N`,OUT
C
 20   CONTINUE
C
      STOP
      END
```

```
CCCCCCCCCC CCCCCCCCCCCCCCCCCCCCCCCCCCCCCCCCCCCCCCCCCCCCCCCCCCCCCCCCCCCCCC
C                                                                        C
C                                                                        C
C       THIS PROGRAM CALCULATES THE VALUES WHICH WHEN PLOTED CREATE       C
C       THE THREE LOBE PATTERN OF INTEREST IN MODAL DOMAIN SENSING.       C
C       NOTE THAT THIS ROUTINE EXHIBITS HIGHEST ACCURACY WHEN THE         C
C       ARGUMENTS OF THE BESSEL FUNCTIONS ARE IN THE RANGE (-3,3).        C
C                                                                        C
C       (THIS ROUTINE USES THE LP11 AND LP21 EVEN AND ODD MODES!!!)       C
C                                                                        C
C          XXXXXXXXXXXXXXXXXXXXXXXXXXXXXXXXXXXXXXXXXXXXXXXXX              C
C           XX                                          XX               C
C          XXX   GO DOWN 38 LINES TO CHANGE PLOT PARAMETERS'''   XXX      C
C           XX                                          XX               C
C          XXXXXXXXXXXXXXXXXXXXXXXXXXXXXXXXXXXXXXXXXXXXXXXXXX              C
C                                                                        C
C                                                                        C
CCCCCCCCCCCCCCCCCCCCCCCCCCCCCCCCLCCCCCCCCCCCCCCCCCCCCCCCCCCCCCCCCCCCCCCCCCC
C
        IMPLICIT DOUBLE PRECISION (A-Z)
        INTEGER N,M
C
        A = 0.5624998500
        B = 0.2109357300
        C = 0.0395428900
        D = 0.0044331900
        E = 0.0003176100
        F = 0.0000110900
        G = 2.2499997000
        H = 1.2656208000
        I = 0.3163866000
        J = 0.0444479000
        K = 0.0039444000
        L = 0.0002100000
C
        PI = 3.141592654D0
C
CCCCCCCCCCCCCCCCCCCCCCCCCCCCCCCCCCCCCCCCCCCCCCCCCCCCCCCCCCCCCCCCCCCCCCCCCC
C                                                                        C
C                                                                        C
C                                                                        C
C       CHANGE THESE PARAMETERS TO MODIFY THE PLOTS COMPLETELY.          C
C       A1 AND A2 ARE THE AMPLITUDE TERMS.  DTHETA IS THE RELATIVE       C
C       PHASE TERM AND Z IS SOME DISTANCE ALONG THE FIBER.              C
C       (PHOTOELASTICITY IS NOT CONSIDERED IN THIS PROGRAM.)            C
C                                                                        C
C                                                                        C
                        A1    = 1.0D0
                        A2    = 1.0D0
                    DTHETA = 0.00D0
                        Z    = 0.00D-4
C
C                                                                        C
C                                                                        C
C                                                                        C
```

```fortran
CCCCCCCCCCCCCCCCCCCCCCCCCCCCCCCCCCCCCCCCCCCCCCCCCCCCCCCCCCCCCCCCCCCCCC
C
      B1 = 1.20D4
C
      X = -4.7501D0
      Y = -4.7501D0
C
      DO 10 N = 1,37
          X = X + 0.25D0
          DO 20 M = 1,37
              Y = Y + 0.25D0
C
              RSQR = (X**2) + (Y**2)
              RBAR = DSQRT(RSQR)
              PHI = DATAN2(X,Y)
C
              X1 = .688D0*RBAR/3.0D0
              X2 = .906D0*RBAR/3.0D0
C
              J02 = 1.0D0 - G*(X2**2) + H*(X2**4) - I*(X2**6)
     $                    + J*(X2**8) - K*(X2**10) + L*(X2**12)
C
              J12 = (0.5D0 - A*(X2**2) + B*(X2**4) - C*(X2**6)
     $                    + D*(X2**8) - E*(X2**10) + F*(X2**12))
     $                    *3.0D0*X2
C
              J2 = (J12*2.0D0/(X2*3.0D0)) - J02
C
              J1 = (0.5D0 - A*(X1**2) + B*(X1**4) - C*(X1**6)
     $                    + D*(X1**8) - E*(X1**10) + F*(X1**12))
     $                    *3.0D0*X1
C
              INTENS =
     $                 ((A1*J1)**2)
     $               + ((A2*J2)**2)
     $               + (2.0D0*A1*A2*J1*J2*DCOS(3.0D0*PHI
     $                                    - B1*Z + DTHET.
C
              WRITE(8,*) X,Y,INTENS
C
  20          CONTINUE
C
      Y = -4.7501D0
C
  10  CONTINUE
 C
      STOP
      END
```

References

1   Butter, C D and G B Hocher   *Fiber Optics Strain Gage*, Applied Optics Vol 17, No 18 15 September 1987

2   Culshaw, Brian; *Optical Fibre Sensing and Signal Processing*, Peter Peregrinus Ltd , London, 1984.

3.   Shankaranarayanan. N K., *Mode-Mode Interference In Optical Fibei*. *Analysis and Experiment*, M.S. Thesis, VPI, 12 March 1987.

4   Shankaranarayanan, N K., et al : *Mode-Mode Interference in Axially Strained Few-Mode Optical Fibers*, Proceedings, SPIE. San Diego, CA, August, 1987

5.   Ehrenfeuchter. P A ; *Modal Domain Detection of Vibration in Beams*, M.S Thesis, VPI, December 1986

6.   Shankaranarayanan, N K., et al , *Optical Fiber Modal Domain Detection of Stress Waves*, Proceedings, IEEE Ultrasonics Symposium, Williamsburg, VA, November 1986.

7.   Cherin, Allen H., *An Introduction to Optical Fibers*, McGraw-Hill Book Company, New York, 1983

8.   Safaai-Jazi, A.; *Optical Waveguide Theory (EE 5980 Class Notes)*, VPI Department of Electrical Engineering, Fall Quarter, 1987.

9   Keiser, Gerd. *Optical Fiber Communications.* McGraw-Hill Book Company, New York, 1983

10   Gloge, D. *Weakly Guiding Fibers.* Applied Optics, Vol. 10, No. 10, October 1971, p 2252

11   Safaai-Jazi, A.. *A Study of Interference Patterns in Few-Mode Optical Fibers.* Internal Report, VPI Department of Electrical Engineering, December 1987

12   Timoshenko, S. *Strength of Materials.* D Van Nostrand Company, Inc , New York, 1940

13.   Kobayashi, Albert S , ed . *Handbook on Experimental Mechanics.* Prentice-Hall, Inc . Englewood Clifts, NJ, 1987

14   Nilsson, James W . *Electric Circuits.* Addison-Wesley Publishing Co , London, 1983

15   Abramowitz, Milton and Irene Stegun, eds *Handbook Mathematical Functions.* Dover Publications Inc , New York, 1972.

16   *Designers Guide to Fiber Optics.* AMP Incorporated, Harrisburg, PA, 1982.

Vita

Bradley D. Duncan ████████████████████████ and
attended Abingdon High School in Abingdon, Virginia He received the B.S.
and M S. degrees in Electrical Engineering From Virginia Polytechnic Institute
and State University in June, 1986 and May, 1988, respectively. His research
interests include intrinsic fiber optic sensor techniques and optical ...
sensor system design.

Mr. Duncan is a member of the IEEE Lasers and Electro-Optics Society.

Bradley D. Duncan

S/5/88

APPENDIX E - Paper Abstracts from Smart Structures Workshop
(Blacksburg, VA) - April 1988

TABLE OF CONTENTS

Introduction to Smart Structures

Dr. Richard O. Claus
Director Fiber & Electro-Optics Research Center
Professor, Electrical Engineering

'Smart," "intelligent" or 'sense-able" structures are structures which contain their own sensors, actuators and computation and control hardware. Although smart structure concepts may be applied to the design and implementation of buildings, dams, bridges, pipelines and ships, recent research efforts have been concentrated on potential aerospace applications in advanced aircraft, launch vehicles, and large space-based platforms.

Virginia Tech has been involved in smart structures research since 1979 with sustained support from the NASA Langley Research Center, Simmonds Precision/Hercules and the Virginia Center for Innovative Technology. In 1979 and 1980, Virginia Tech participated in the first documented smart structure experiments, conducted at NASA Langley, which demonstrated the use of embedded optical fiber sensors for the measurement of strain in low temperature composite materials. Since then Virginia Tech has worked on the development of optical fiber interferometric, blackbody, evanescent, modal domain and time domain sensors for the evaluation of composite cure, in-service structural component monitoring, nondestructive materials evaluation, and damage detection and evaluation.

At the same time, Virginia Tech faculty, students and staff have cooperatively developed and demonstrated effective embedded actuators for structural shape modification, experimentally analyzed the micromechanical problems associated with embedded sensor and actuator elements in advanced composites, developed computational and control

system architecture concepts for smart structure applications, and considered the integration of these interdisciplinary problems in specific aerospace structure designs.

This Smart Structures Workshop reviews the major non-proprietary accomplishments in this area by Virginia Tech during the past several years and in particular highlights the recent results of the past several months. More than a dozen brief technical discussions are followed by a working panel discussion lunch period and afternoon laboratory demonstrations of implemented smart structure concepts.

Materials Issues for Smart Structures

Dr. Garth L. Wilkes
Professor
Chemistry

The term "smart structures" carr:s the implication that a given material or "structure" when provided a particular stimulus, will generate a specific response. What the specific stimuli are as well as the nature and magnitude of the response will depend upon the type of "smart structures" desired for a given application. This brief talk will focus on material parameter considerations with respect to generating smart structures and will illustrate a number of specific cases by example. While a somewhat higher emphasis will be given to those concerned with polymeric based materials, discussion will also consider those based on either metallic or ceramic systems as well. Finally, some new directions toward the development of new hybrid or complex material structures will also be outlined.

Experimental Analysis of Smart Structure Materials by Full-Field Optical Techniques

Dr Robert Czarnek
Assistant Professor
Engineering Science and Mechanics

The concept of integration of sensing and controlling devices with load carrying elements has been implemented in the form of so-called "smart structures". In a smart structure, sensors and actuators are embedded in the material that the elements of the structure are made of. The materials used to make these structures are mostly fiber-reinforced composites. Probably the most effective type of sensors used in smart structures are made of optical fibers embedded between the layers of the structural fibers. The optical fiber deforms together with the composite element and modulates light passing through the fiber. allowing the detection of dangerous strain levels in the structure as well as failure of the material

The presence of the optical fiber embedded in the material makes sense only if it does not diminish the performance of the material. Composite materials on the micromechanics level are extremely complex structures and their behavior is still not fully understood. The interaction between the fibers in a layer and the layers in the material causes strain levels much higher than those predicted analytically. Imperfections of the manufacturing process complicate the situation even further, introducing strong nonuniformity into the strain distribution in the material An optical fiber introduced as an element of such a complicated structure brings even more unknowns into the materials analytical model.

Some preliminary experiments have been performed on graphite epoxy coupons with optical fibers embedded in the direction perpendicular to the direction of the load. Two

layups. $[90_2/0_2/\text{fiber}/0_2/90_2]$ and $[0_2/90_2/\text{fiber}/90_2/0_2]$, were tested using high sensitivity moire interferometry with a sensitivity resolution on displacement measurements of 100 nanometers. The measurements were performed on the edges of the specimens. Strains as high as 2% were detected in the vicinity of the fibers at a load equal to 50% of the calculated failure load. Figure 1 illustrates fringe patterns representing:

(a) the horizontal displacement field and

(b) the vertical displacement field at this load level in the specimen with the optical fiber embedded between the fibers running in the 0 degree direction. The concentration of high strains near the optical fiber is clearly visible. Corresponding patterns were recorded for a specimen with the other layup.

The results of the performed experiments show strong strain concentration around the embedded sensors and a very strong dependence of the strain concentration factor on the layup of a composite member. The magnitude of the effect of the embedded components on the strain distribution in the structural elements suggests a strong need for an extensive experimental and analytical program on the determination of the influence of embedding optical sensors on the behavior of composites and on providing a means for reducing undesired effects.

spec. 4B vaccuum w/press plate

spec. 4B vaccuum w/press plate

.l-field   .744 "n

l - field 1797 lb

(a)

(b)
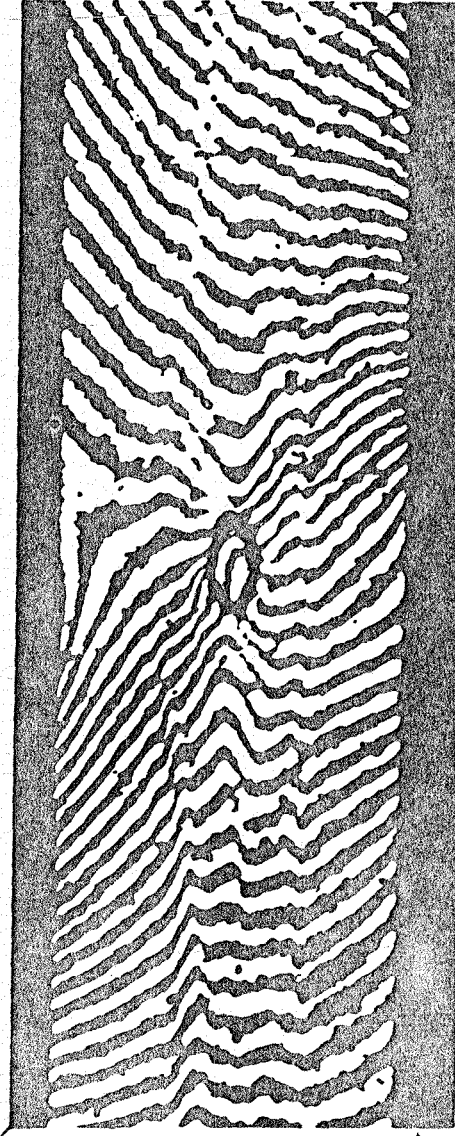
Figure 1.

Large Deployable Antennas in Space as Smart Structures

Dr Warren L Stutzman
Satellite Communications Group
Professor, Electrical Engineering

Many space-based projects are planned into the next century that require large antennas These antennas are most often reflectors and occasionally phased arrays. In either case, the antenna is up to many meters in extent and must be deployed in space Performance depends critically on the accuracy of the antenna shape. Antennas do not deploy accurately and also are subject to distortions while in space, primarily in the form of thermal gradients Therefore, sensing and control are necessary. With large scale antennal structures the sensing, control, and computing functions are best integrated into the design, creating a smart structure. This paper will focus on the large space antenna as an ideal candidate for smart structure realization.

Active Trusses for Structural Control

Dr Harry H Robertshaw
Associate Professor
Mechanical Engineering

and

Dr Charles F Reinholtz
Assistant Professor
Mechanical Engineering

Structures that can change their configuration, termed variable geometry trusses (VGTs) or active trusses, are being studied for their many applications· active control of structural vibration, pointing of structures or substructures, or performing robotic-like tasks. In fact, given a structure that can move actively, the distinction between a robot and a structure becomes blurred

We are presently using two forms of active structures to control the vibration of continua attached to them. We have performed planar and spatial vibration reduction experiments with two configurations for the active truss.

The planar experiments have been conducted with one plane of a tetrahedral-tetrahedral (T-T) truss controlling a beam that is constrained to almost planar motion. The spatial experiments were performed with an octahedral-octahedral (O-O) truss (nicknamed the geodesic truss) controlling a rod. In each case the trusses had three degrees of freedom embodied in three links of variable length actuated by machine screws driven by dc motors The motion of the links were sensed with resistive transducers and the motions of the beam and the rod were sensed using strain gages. The equations of motion for the systems were linearized about an operating point and an LQR optimal control law was applied with individual estimation of most of the

needed rate terms. Significant vibration reduction was observed with reasonable correlation with the analyses.

The spatial truss was also used to perform a rudimentary robotic task: writing letters with a pen placed at the end of a rigid rod attached to the structure. This robotic task involved solving the inverse kinematic equations for the needed link lengths in order to follow the required "path" to write the letters. For the geodesic truss, the solution of both the forward and the inverse kinematics is iterative. A reasonable amount of effort has gone into optimizing theses iterative procedures.

Additionally, we have studied kinematics of most of the different possible configurations of the basic unit of variable geometry trusses. The advantages and disadvantages of these different forms are determined based on: ease of solution of the kinematic equations, possible workspace of the trusses, loads involved during quasi-static and dynamic maneuvers. and possible kinds of motions available from the structure.

Development of a Novel 'Adaptive/Smart Composite Material' Utilizing Nitinol 'Fibers'

Craig A. Rogers
Associate Professor
Mechanical Engineering

A novel class of adaptive materials has been developed and demonstrated at Virginia Polytechnic Institute and State University. This class of adaptive materials utilize a shape-memory-alloy (Nitinol) in a laminated, fiber-reinforced composite. Adaptive materials are a relatively new class of materials that have the capability of changing their physical geometry, or of altering their physical properties. The basic concept behind the adaptive material developed at VPI&SU is that the shape memory alloys are integrated in a bulk material (i e., laminated fiber- reinforced composite, or an elastomer) as an actuator for force, motion, and/or variable stiffness. Possible applications for this class of adaptive materials are: in structures that are part of long-duration, unattended space missions (for which the material must be able to compensate for damage by redistributing the load around failed portions of the structure); in biomedical applications (such as artificial heart valves and pumps with no moving parts), in active vibration control of large flexible structures, in active acoustic control for aircraft to reduce interior sound levels, and in robotic manipulators.

The adaptive response of the material has been demonstrated experimentally by controlling the motion of a fiberglass cantilever beam. The cantilever beam is a unique composite material containing several shape memory alloy fibers (or films) in such a way that the material can be stiffened or controlled by the addition of heat (i.e., apply a current across the fibers) A demonstration of the capabilities of this unique class of materials will be presented. Shape memory alloys and the mechanism by which

they exhibit the characteristic shape memory effect (SME) will also be explained in some detail.

The basic physical design of the demonstration adaptive/smart composite cantilever beam is conceptually simple. The shape memory alloy fibers are embedded in a material off of the neutral axis of the beam which when activated introduce a large force and subsequent bending of the structure. Before imbedding the fibers, the shape memory alloy fibers are plastically elongated and constrained from contracting to their normal or 'memory' length upon curing the composite material with high- temperature. The fibers are therefore an integral part of the composite material and the structure. When the fibers are heated, generally by passing a current through the shape memory alloy, the fibers 'try' to contract to their 'normal' length and therefore generate a uniformly distributed shear load along the length of the fibers. The shear load offset from the neutral axis of the structure will then cause the structure to bend in a known and predictable manner. There are several other configurations that are currently being implemented and investigated

This presentation will describe the actual prototypes of the novel 'Adaptive/Smart Composite Material' and the capabilities of the devices. The basic concepts and mechanisms by which the adaptive response of the material is demonstrated will also be presented. several of the technical problems and solutions will be discussed. Lastly, the future direction and impact of this technology will be postulated.

Fiber Optic Methods for Structure Monitoring

Kimberly D. Bennett
Research Associate, Fiber & Electro-Optics Research Center
Electrical Engineering

and

Dr. Richard O. Claus
Director, Fiber & Electro-Optics Research Center
Professor, Electrical Engineering

Structures engineered for integrated active control impose demanding requirements on system components such as actuators, sensors, and intelligent control schemes. In particular, sensors are required to determine structural status, both in terms of normal operating parameters such as position, strain, or temperature, as well as actual material integrity. Perhaps the most mature approach for embedded sensing, and one readily applicable to attached sensors, involves the use of optical fibers.

Much of the pioneering work in smart structures, specifically embedded fiber optic sensing in structural materials, was per formed in the early 1980's at NASA Langley and Virginia Tech. Presently a number of researchers are investigating the use of fiber optics for monitoring ground, air, and space based structures. In addition, a number of different mechanisms are being exploited to perform various sensing tasks. Among these are optical time and frequency domain techniques, modal domain sensing, absolute and differential fiber interferometry, polarimetry, and various intensity modulation methods. Targeted observables include both point-to-point and distributed strain measurements, vibration and structural mode analysis, state of cure in composite materials, temperature monitoring, and damage assessment.

In this paper, several general sensing methods will be reviewed. Emphasis will be given to those which have had particular application in smart structures research at Virginia Tech.

Modal Interference Techniques for Strain Detection in Few-Mode Optical Fibers

Bradley D Duncan
Graduate Research Assistant, Fiber & Electro-Optics Research Center
Electrical Engineering

Interference between the modes of an optical fiber results in specific intensity patterns which can be modulated as a function of disturbances in the optical fiber system. These modulation effects are a direct result of the differential phase modulation which arises due to the difference in propagation constants of the constituent modes. Based on these concepts it has been shown how the modulated intensity patterns caused by various mode groups in few-mode optical fibers (V < 5.0) can be used to detect strain. A detailed discussion of the modal phenomena responsible for these strain induced pattern modulations is presented and it is shown that strain detection sensitivities on the order of 10-10 can be expected for simple systems based on these modal interference concepts. Actual strain detection systems based on the developed theory are also proposed and evaluated.

Applications of OTDR Methods to Structural Analysis

Russell G. May, Jr
Technical Director, Fiber & Electro-Optics Research Center
Electrical Engineering

Embedded optical fibers have been proposed as a technique for measuring strain and displacement in materials. particularly composite materials. By measuring parameters of the light exiting the embedded fiber, the integrated strain along the fiber can be derived. A promising technique to resolve the strain at discrete locations in a material is optical time domain reflectometry (OTDR).

OTDR is a measurement technique in which a short pulse of light is launched into an optical fiber and is reflected back to the input end by constituent atoms along the length of the fiber The intensity of the reflected light is plotted as a function of the time delay that the light pulse suffers in returning to the input end of the fiber. Since the time delay is linearly related by the speed of light in the fiber to the distance from the input to the reflection, OTDR may be used to accurately determine the location of a discrete reflector.

Experiments at Virginia Tech in 1984 demonstrated the feasibility of using OTDR to sense deformation of composite coupons with embedded optical fibers. In those experiments, OTDR was used to measure the loss induced by microbends in an embedded fiber at a point where pressure was applied. The spatial resolution of the measurement system is limited by the optical pulse width. Although the results demonstrated the validity of the concept, derivation of actual fiber or composite strain from microbend loss is difficult.

Further research at the Fiber and Electro-Optics Research Center in 1987 extended the work and enabled the direct measurement of fiber (and composite) strain by placing reflective markers within the embedded fiber. The markers were fabricated by separating the fiber at a point, and splicing the two ends together with an air gap between them. The Fresnel reflection from the refractive index mismatch of the splice yields a reflection center that produces a readily observable mark on the OTDR trace. The longitudinal strain of the fiber section between two air gap splices is found by measuring the resulting increase in time delay between the two reflective markers corresponding to the two air gaps

Limitations of this technique include a limit to the number of air gap splices that may be placed sequentially on a fiber due to the splice loss and fiber loss budget. A limit to the achievable spatial resolution exists, traceable to the low energy content of very narrow width laser pulses.

Acoustic Fiber Methods for Structural Monitoring

Dr. Ahmad Safaai-Jazi
Associate Professor
Electrical Engineering

Transmission properties of cladded fiber acoustic waveguides are briefly reviewed and compared with those of optical fibers. Applications of acoustic fibers in sensing and signal processing are addressed. Attention is focused on embedded acoustic fibers for structural monitoring Two schemes for the implementation of acoustic fiber sensing concept are discussed In one scheme the acoustic fiber sensor functions in much the same way as an optical fiber sensor; namely that an external disturbance perturbs a physical parameter of the fiber yielding a change in amplitude, phase, or polarization of the acoustic wave propagating in the fiber. The amount of the change is a measure of the external disturbance. In a second scheme, acoustic fiber is used in a listening mode picking up acoustic emissions and thus monitoring the health of the structure. Advantages of acoustic fiber sensors in certain special applications are pointed out. Research and development of acoustic fiber phase sensors at the Fiber and Electro-Optics Research Center of Virginia Tech are addressed.

Acoustic Emission Detection in Smart Materials

Kimberly D. Bennett
Research Associate, Fiber & Electro-Optics Research Center
Electrical Engineering

and

Kevin D. Zehner
Research Assistant, Fiber & Electro-Optics Research Center
Electrical Engineering

The monitoring of acoustic emission (AE) is an important technique for the nondestructive characterization of strained materials. Time and frequency domain analyses of AE events yield information about the type, geometry, and location of defects, as well as about material properties and how failure may occur. The quantitative interpretation of AE event signatures is critically dependent upon the faithfulness of the acoustic transduction and signal processing system in reproducing localized stress wave amplitude as a function of time. Although presently employed piezoelectric sensors are sensitive and reasonably broadband, they are not suited to embedded measurements, and are highly susceptible to electrical noise.

This paper reports the detection of acoustic emission signals generated in symmetric cross-ply composite laminates using internal optical fiber sensors. Few-mode optical fibers were embedded between different prepreg layers during lay-up, and the resulting specimens were cured under pressure between heated platens. During the original tests, samples containing optical fibers laid in the axial direction were loaded in tension in specially designed grips, allowing for continuous monitoring of light. Acoustic signals were obtained by detecting changes in an optimized modal domain feature inherent in the intermodal interference pattern. Independent measurements were also supplied by a piezoelectric transducer made by Acoustic Emission Technology

Corporation Agreement between transducing methods was excellent, indicating that acoustic emissions may be measured using fiber optic sensing techniques.

On-going experiments involve samples with optical fiber laid across the direction of applied load, allowing for the use of conventional grips, although requiring some care during cure. Collection of AE signals and computational analysis is simplified with the use of an inexpensive digital oscilloscope and associated computer. Also, the use of multiple fibers for the location of AE events is investigated. Results of these tests, as well as limitations of the method and implications for the composites industry are discussed.

Fiber Optic Assessment of Impact Damage in Smart Materials

Michael R. Dumais
Research Assistant, Fiber & Electro-Optics Research Center
Electrical Engineering

Kimberly D. Bennett,
Research Associate, Fiber & Electro-Optics Research Center
Electrical Engineering

This study investigates the possibility of incorporating optical fibers into a structure and using them to characterize impact damage. It is believed that the ability to correlate signal disturbances from optical fibers with physical disturbances would provide invaluable real-time information about the reliability of active engineering systems.

Previous work in this area, conducted at Virginia Tech with sup port from NASA Langley, General Motors, and the Virginia Center for Innovative Technology, involved the use of an embedded optical fiber mesh. Continuous wave light signals propagated through the fibers in the x and y directions, and were collected by an array of discrete photodetectors. Disturbances in the cw output due either to fiber breakage or intermodal interference were related to various impacts. Disadvantages arise in the need for injection of light into multiple fibers, and for multiple detectors.

In order to simplify the system and quantify impact signals, an exposed optical fiber having a V number of approximately 4.5 was attached to a thick aluminum plate with a rigid epoxy. The fiber was excited with monochromatic laser light and its output monitored with a photodetector. With the plate inverted and lying flat, several trials were run in which a steel mass was dropped on the plate from different heights and positions with respect to the fiber sensor. Using a digital waveform analyzer, fiber output signal changes were captured over the course of an impact. With the aid of a

computer. Fourier analysis of the signals was performed, and attempts were made to correlate spectral signatures with different types of impacts. Also, output signal power densities were calculated and analyzed with respect to impact amplitude and location. After attaching a second fiber to the plate, similar drop tests were run and blind impact location information was extracted by examining the time lag between the disturbance signals from the two fibers

In this paper the limitations of fiber optic impact and damage detection are discussed, and direction for future efforts proposed.

Control and Signal Processing Design Issues in Smart Structures

John C. McKeeman
Assistant Professor
Electrical Engineering

and

Doug K. Lindner
Assistant Professor
Electrical Engineering

The next generation of space structures will be significantly different from the current generation of spacecraft. The new space structures will be made of new composite materials which will allow them to be of significantly larger dimensions The increased size, in particular, along with tighter performance specifications will require that the structure be designed and built to function as a cohesive unit in which subassemblies strongly interact to achieve system performance specifications. The system wide integration will be achieved by control loops which (effectively) coordinate the subassemblies. Such a structure we call a smart structure.

In this paper we examine the system configuration of smart structures from a systems perspective. To focus the discussion we consider as an example structure a large space antenna, the Hoop Column Antenna We describe the control loops required to implement and maintain the antenna in space. Special attention is given to the components required to implement the control system. Several control design issues are highlighted.

To successfully produce this control system, several new computing technologies must be tailored to the applications required by each subassembly. At the highest level in this hierarchical control system, Artificial Intelligence coupled with Neural Networks will control the housekeeping activities and gross structure control. At the lowest level,

application specific integrated circuits will be customized to handle the high throughput, high bandwidth requirements for the sensors and actuators. This paper focuses on new computers architectures required to implement advanced control structure within a intelligent structure.

C - 4

APPENDIX F - Abstracts from Papers To Be Presented at The SPIE
Conference (Boston, MA) - September 1988

TABLE OF CONTENTS

INTERFEROMETRIC MEASUREMENTS OF STRAIN CONCENTRATIONS INDUCED BY AN OPTICAL FIBER EMBEDDED IN FIBER REINFORCED COMPOSITES

R. Czarnek[*], Y.F. Guo[*], K.D. Bennett[+] and R.O. Claus[T]

* Department of Engineering Science and Mechanics
+ Department of Electrical Engineering
Virginia Polytechnic and State University
Blacksburg, Virginia 24061

The concept of using of optical fibers for sensing the mechanical response of composite structures to applied loads has been implemented in the form of so-called "smart skins." An optical fiber imbedded between the layers of the structural fibers deforms together with the composite structure and modulates the light passing through the fiber. This allows for the detection of dangerous strain levels in the structure, as well as failure of the material.

The presence of the optical fiber embedded in the material is viable only if it does not diminish the performance of the material. Composite material on the micromechanics level is an extremely complex structure and its behavior is still not fully understood. The interaction between the composite fibers in a layer and the layers in the material causes strain levels much higher than those predicted analytically. Imperfections of the manufacturing process complicate the situation even further, introducing strong nonuniformity into the strain distribution of the material.

An optical fiber introduced as an element of such a complicated structure introduces more unknowns into the analytical

model of the material. Several important questions can and should be answered before the concept of embedding optical fibers can be commercialized. These include understanding how fibers influence the strain field in a composite element, and if the strain concentration factors introduced are significant when compared to the natural strain variations which arise from the manufacturing process. Strain concentration dependence on the layup and position of the optical fiber is also unknown. Finally, understanding of whether the inclusion of optical fiber can cause premature failure of a composite element, and how to reduce any such effects is necessary.

These issues require serious experimental investigation. Moire interferometry is a high sensitivity method yielding full field measurement of in-plane displacements. Its sensitivity is limited to 1/2 of a wavelength of the light used per fringe order, and in practical applications a sensitivity resolution of the order of 100 nm is standard in the VPI&SU Photomechanics Laboratory. The spatial resolution is limited only by the quality of the optical system used to capture the image and details as small as 1 micrometer can be successfully resolved.

In this paper, we report moire interferometry experiments performed on the face of a composite, as well as on its edge. Measurements on the face indicate the global influence of the fiber on the deformation of the specimen, and those on its edge give information about the very localized strain disturbance in the direct vicinity of the fiber. Representative layup sequences have been investigated, and the effect of embedding optical fiber has been analyzed.

2

DEMONSTRATION OF A SMART STRUCTURE WITH EMBEDDED ACTUATORS AND SENSORS FOR ACTIVE CONTROL

C.A. Rogers[*], K.D. Bennett[+], H.H. Robertshaw[*], and J.C. McKeeman[+]

* Department of Mechanical Engineering
+ Department of Electrical Engineering
Virginia Polytechnic Institute and State University
Blacksburg, Virginia 25061

A novel class of "smart" materials having embedded sensors and actuators and appropriate "intelligence" has been developed and demonstrated at Virginia Tech. This class of adaptive materials utilize a shape memory alloy (Nitinol) in a laminated, fiber-reinforced composite as the embedded distributed actuator. The basic concept behind the smart materials developed at Virginia Tech is that the shape memory alloy fibers are integrated into a bulk material such as a composite structural member, and used as actuators for force, motion, and/or variable stiffness. Sensing of material dynamics and strain is performed by embedded optical fiber sensors. Possible applications for this class of adaptive materials are in structures that are part of long-duration, unattended missions (for which the material must be able to compensate for damage by redistributing the load around failed portions of the structure), in biomedical applications (such as artificial heart valves and pumps with no moving parts), in active vibration control of large flexible structures, in active acoustic control for aircraft to reduce interior sound

levels, and in robotic manipulators.

The adaptive response of structural members has been demonstrated in hardware by controlling the motion of a fiberglass cantilever beam. The beam is a unique composite material containing several shape memory alloy fibers in such a way that the material can be stiffened or controlled by the addition of heat, created by applying a current across the fibers. Embedded optical fibers monitor the motion of the cantilever beam and application-specific intelligent hardware has been designed and built to control the motion and/or vibration of the structure.

Results from experimental studies showing active motion control with this novel smart structure will be presented. Shape memory alloys and the mechanism by which they exhibit the characteristic shape memory effect (SME) for use as an actuator will be explained, as well as the physical design and implementation of the embedded strain sensing fiber optics. The control strategy (i.e. "intelligence) will also be presented. Lastly, the future direction and impact of this technology will be postulated.

FULL FIELD ANALYSIS OF MODAL DOMAIN SENSOR
SIGNALS FOR STRUCTURAL CONTROL

K.D. Bennett, J.C. McKeeman, and R.G. May

Fiber and Electro-Optics Research Center
Virginia Polytechnic Institute and State University
Blacksburg, Virginia 24061

When coherent light is launched into multimode optical fiber, a complex interference of the modes occurs along the fiber length, and a speckle pattern results at the output. The exact arrangement of the speckles depends on the modal arrangement integrated along the fiber, and is modulated by local changes in geometry and refractive index profile. Interrogating the modal domain signal of an optical fiber embedded or attached to a structure is a well established means of determining pseudostatic strain and structural vibration frequency and mode shape, as well as monitoring acoustic events occurring in the material.

Prior research has depended upon spatially filtering the optical output to determine the speckle motion. In addition to requiring determination of an optical Q point, this method also necessarily results in a loss of optical power and useful information. Advancement in power collection has been made through the use of low mode optical fibers, which share power among few output speckles. Some novel in-line fiber techniques have also recently been reported for simplifying the process and gathering more information.

In this paper, we report the use of a detector array to process the modal domain output patterns. The array is linked to an IBM-PC, which reduces the data in real time. Full field determination of low mode speckle rotation due to axial strain is noted, as well as gross speckle rotation in multimode fibers due to bulk fiber motion. Statistics of speckle motion in both low an multimode fibers has also been investigated. Finally, the importance of this method for use in smart structure dynamics and control will be discussed.

INTENSITY PATTERN MODULATION IN OPTICAL FIBER
MODAL DOMAIN SENSOR SYSTEMS: EXPERIMENTAL RESULTS

Bradley D. Duncan

Fiber & Electro-Optics Research Center
Virginia Polytechnic Institute and State University
Blacksburg, Va 24061

Brian W. Brennan

Simmonds Precision I.S.D.
Panton Road, Vergennes, VT 05491

(ABSTRACT)

The past several years have given rise to many optical fiber
sensing techniques which may be employed in systems to detect
such observables as temperature, pressure, displacement and
strain. As sensing devices, optical fibers are attractive due to
their small size, flexibility, ruggedness and intrinsic
dielectric nature. In addition, their proclivity to be highly
sensitive to external perturbations is quickly making optical
fibers the sensing devices of choice for many passive
non-intrusive sensor applications.

Simply put, optical fiber sensors exploit the effects of
perturbations and external factors on the light in the fiber.
Unparalleled in sensitivity are the phase modulated sensors, a
classic example of which is the dual-fiber Mach-Zehnder
interferometer. By being based on an absolute phase modulation

...eme, however, such a sensor tends to be quite complex, with the reference phase and quadrature point often needing to be actively controled.

By comparison, systems utilizing single-fiber modal interference schemes, such as those to be discussed in this paper, essentially cause the two arms of the interferometer to be within the same environment. This provides for a high common mode rejection capacity while affording the system the further advantages of simplicity and increased ruggedness, with no need for couplers. Though remaining highly sensitive, as will be shown, some sensitivity will be sacrificed in a single-fiber interferometer, or modal domain sensor, due to the fact that the sensor mechanism will now be based on differential phase modulation.

In a companion paper a detailed theoretical analysis of the modal phenomena responsible for the far field intensity pattern modulation of various modal domain sensor systems is presented. This paper will present experimental results which verify the expected system behavior and which serve as proof of the significance of the modal domain sensing technique. The results of both static and dynamic strain measurements are presented, as are data which demonstrate the strain sensitivities achievable with modal domain sensor systems. System design, stability, and calibration techniques are also presented.

SMART STRUCTURES PROGRAM AT VIRGINIA TECH

R. O. Claus and K. D. Bennett, Fiber and Electro-Optics Research
Center, Virginia Tech, Blacksburg, VA 24061.

Abstract

This paper reviews the smart structures and avionics research
and teaching program at Virginia Tech. Started in 1979 with
support from the NASA Langley Research Center, this program has
grown to include interdisciplinary participation between more
than twenty faculty from seven departments in the Colleges of
Engineering and Arts and Sciences, graduate and undergraduate
engineering classes which specifically address smart structures
issues, and directed research programs conducted in cooperation
with more than a dozen aerospace companies and government
organizations.

Current smart structures research includes major efforts in
1) the development of embedded and attached optical fiber and
acoustic fiber sensors for a wide range of applications including
cure monitoring, in-service lifetime structural monitoring,
nondestructive evaluation, and impact and damage detection and
analysis, 2) sensor signal multiplexing, processing and data
handling to achieve near real time distributed structural
analysis, and 3) the combined use of embedded or attached sensors
and actuators to achieve controlled structural response. Special
campus facilities which have been used for this work include an

.ical fiber fabrication facility, an autoclave for composite structure fabrication and curing, and laboratories for optical fiber sensor development, materials response and nondestructive evaluation, structural control testing, and computer engineering. The work in all of these areas during the past few years by different Virginia Tech faculty, staff, graduate student and visiting scientist groups will be reviewed.

10

Fiber Optic Sensor Systems for Smart Aerospace Structures

W. J. Rowe, R. O. Claus*, D. A. Martin+, and D. Trites‡

Lockheed Aeronautical Systems Company
Dept. 72-51, Zone 303
Marietta, Georgia 30063

ABSTRACT

Current and projected advances in aerospace structures technology for such ongoing programs as the Advanced Tactical Fighter, National Aerospace Plane, and NASA/DoD space platforms are used as the starting point for a top-level structural monitoring systems analysis. Performance requirements are considered for such structures, and used to identify needs for integral sensors and systems. Results of recent work are discussed, which have demonstrated the potential for fiber optic sensor systems which can assess and report on structural condition in real time. The essential system elements are defined, and constraints imposed by vehicle configurations and mission performance are considered. The resulting development needs, for fiber optic sensors and systems to achieve Smart Structures in these applications, are stated in conclusion.

*Fiber & Electro-Optics Research Center, 648 Whittemore Hall, Virginia Tech, Blacksburg, VA 24061.

+Kelly Johnson Research & Development Center, Rye Canyon, Lockheed Aeronautical Systems Company, P. O. Box 551 (7471/211/2), Burbank, CA 91520.

‡Bldg. 104, Org. 62-13, Lockheed Missiles & Space Company, Space Systems Division, 1111 Lockheed Way, Sunnyvale, CA 94086.

APPENDIX G - Invited Lectures

INVITED LECTURES

1. "Optical Fiber Fundamentals," Proc. Optical Fiber System Design (Madison, WI) February 1988 (R.O. Claus).

2. "Smart Skins and Avionics," LTV Aerospace (Dallas, TX) Februaury 1988 (R.O. Claus).

3. "Optical Fiber Sensors" (Short Course), MFOC '88 (Crystal City, VA) March 1988 (R.O. Claus).

4. "Fiber Optic Sensors for Materials Evaluation," Hercules Research Center (Wilmington, DE) May 1988 (R.O. Claus).

APPENDIX H - Papers To Be Presented

PAPERS TO BE PRESENTED

1. "Embedded Sensors," Sensor Technology Symposium (Alcoa Center, PA) June 1988 (R.O. Claus).

2. "Intelligent Structures Research at Virginia Tech," QNDE (La Jolla, CA) August 1988 (R.O. Claus, K.D. Bennett, R.G. May and B.D. Duncan).

3. "Low-Profile Optical Time Domain Fiber Sensors for Materials Evaluation," QNDE (La Jolla, CA) August 1988 (R.O. Claus, S. Sudeora, K.A. Murphy and K.D. Bennett).

4. "Advanced Sensors for Smart Materials in Aerospace Applications," AIAA Conference (Atlanta, GA) September 1988 (J.S. Heyman, R.S. Rogowski and R.O. Claus).

5. "Demonstration of A Smart Structure with Embedded Actuators and Sensors for Active Control," SPIE (Boston, MA) September 1988 (C.A. Rogers, K.D. Bennett, H.H. Robertshaw and J.C. McKeenan).

6. "Fiber Optic Sensor Systems for Smart Aerospace Structures," SPIE (Boston, MA) September 1988 (W.J. Rowe, R.O. Claus, D.A. Martin and D. Trites).

7. "Full Field Analysis of Modal Domain Sensor Signals for Structural Control," SPIE (Boston, MA) September 1988 (K.D. Bennett, J.C. McKeeman and R.G. May).

8. "Intensity Pattern Modulation in Optical Fiber Modal Domain Sensor Systems: Experimental Results," SPIE (Boston, MA) September 1988 (B.D. Duncan and B.W. Brennan).

9. "Interferometric Measurements of Strain Concentrations Induced by An Optical Fiber Embedded in Fiber Reinforced Composites," SPIE (Boston, MA) September 1988 (R. Czarnek, V.F. Guo, K.D. Bennett and R.O. Claus).

10. "Smart Structures Program at Virginia Tech," SPIE (Boston, MA) September 1988 (R.O. Claus and K.D. Bennett).

11. "Optical Fiber Methods for the NDE of Smart Skins and Structures," SEM Fall Conference (Indianapolis, IN) November 1988 (R.O. Claus, K.D. Bennett and B.D. Duncan).

END

DATE

FILMED

AUG 22 °1988

End of Document